

THERMOMECHANICAL STABILITY OF LOW AND HIGH-TEMPERATURE PEM FUEL CELL SEALANTS

Thesis

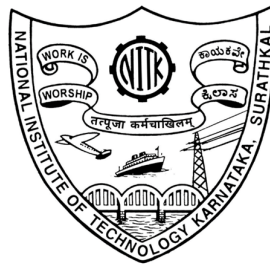
Submitted in partial fulfilment of the requirement for the degree of

DOCTOR OF PHILOSOPHY

by

VIKAS KUMAR

(Reg. No. 187130ME023)



DEPARTMENT OF MECHANICAL ENGINEERING
NATIONAL INSTITUTE OF TECHNOLOGY KARNATAKA
SURATHKAL, MANGALORE – 575025

October, 2024

THERMOMECHANICAL STABILITY OF LOW AND HIGH-TEMPERATURE PEM FUEL CELL SEALANTS

Thesis

Submitted in partial fulfilment of the requirement for the degree of

DOCTOR OF PHILOSOPHY

by

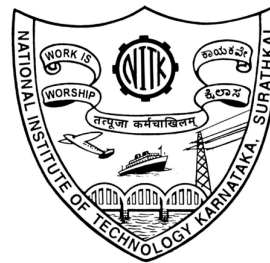
VIKAS KUMAR

(Reg. No. 187130ME023)

Under the guidance of

Dr. POORNESH KUMAR KOORATA

Associate Professor



DEPARTMENT OF MECHANICAL ENGINEERING
NATIONAL INSTITUTE OF TECHNOLOGY KARNATAKA
SURATHKAL, MANGALORE – 575025


October, 2024

DECLARATION

I hereby declare that the Research Thesis entitled "**THERMOMECHANICAL STABILITY OF LOW AND HIGH-TEMPERATURE PEM FUEL CELL SEALANTS**" which is being submitted to the **National Institute of Technology Karnataka, Surathkal** in partial fulfilment of the requirements for the award of the **Degree of Doctor of Philosophy in Mechanical Engineering** is a *bonafide report of the research work carried out by me*. The material contained in this Research Thesis has not been submitted to any University or Institution for the award of any degree

Register Number: **187130ME023**

Name of the Research Scholar: **VIKAS KUMAR**

Signature of the Research Scholar: 

Department of Mechanical Engineering

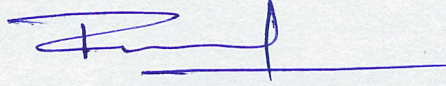
Place: NITK, Surathkal

Date: **25/10/2024**

CERTIFICATE

This is to certify that the Research Thesis entitled “**THERMOMECHANICAL STABILITY OF LOW AND HIGH-TEMPERATURE PEM FUEL CELL SEALANTS**” submitted by **Mr. VIKAS KUMAR** (Register Number: **187130ME023**) as the record of the research work carried out by him, *is accepted as the Research Thesis submission* in partial fulfilment of the requirements for the award of the degree of **Doctor of Philosophy**.

Research Guide



Dr. Poornesh Kumar Koorata

Associate Professor

Department of Mechanical Engineering



Chairman - DRPC

Department of Mechanical Engineering

National Institute of Technology Karnataka

Surathkal, Mangalore – 575025

ACKNOWLEDGMENT

A guide/mentor imparts meticulous care and support to his students, portraying genuine devotion and commitment. He shows his students the correct pathway so that he can see them becoming better every day and achieving a better position in their careers. I would like to bestow sincere gratitude to my guide **Dr. Poornesh Kumar Koorata**, Associate Professor, Department of Mechanical Engineering, National Institute of Technology Karnataka, Surathkal, Mangalore, for giving me the opportunity to learn every day. I was able to acquire knowledge and improve my skills because of his continuous support and guidance throughout my Ph.D. journey, which motivated and helped me to move forward in the right direction.

I am very thankful to the Director, **Prof. B. Ravi**, for providing a research-friendly environment to the research scholars. I am grateful to **Prof. S.M. Murigendrappa**, Professor and Head of the Department, Department of Mechanical Engineering, National Institute of Technology Karnataka, Surathkal, Mangalore for providing all the research-related facilities in the department. I would also like to thank RPAC members **Dr. Sharnappa Joladarashi**, Professor, Department of Mechanical Engineering, and **Dr. Prasanna Belur D**, Professor, Department of Chemical Engineering, as well as DRPC secretary, **Dr. Parthasarathy P**, Assistant Professor, Department of Mechanical Engineering, National Institute of Technology, Karnataka, Surathkal for their visionary comments and support in completing this work.

I express my gratitude to CRF Chairman **Prof. Keyur Raval** and staff **Mr. Nishant** and **Mr. Kiran** for providing access to various testing facilities. I want to thank staff of purchase department, **Mr. Arvind Karnad** for providing a smoother purchase of the equipments for my research work.

Throughout my Ph.D. journey, I am extremely obliged to **Dr. Vaishakh R**, **Dr. Umesh Shinde**, **Pranav Padavu**, **Sachin Kumar Varshney**, **Vibha Naik**, and **Dr. Vikash Kumar Singh Chauhan**, my research group members of the Electrochemical Energy System Design Laboratory, for their continuous support.

I want to express my deepest gratitude to my parents, **Sanyukta Sinha** and **Mrityunjay Prasad**, who always supported me in my endeavors. Their unwavering belief in my

capability encouraged me to move ahead. I would like to thank my brothers, **Birendra Kumar** and **Kumar Saurav**, and my sister, **Rupam Rashmi**, for their continuous support. I want to thank my wife, **Goldi Kumari**, for her unconditional love, unwavering support, and motivation that helped me a lot in this wonderful journey.

Life would have been less exciting and intriguing in the absence of friends. I want to thank my dearest friends **Nitin Kanth**, **Snehil Kumar**, **Vaibhav Tiwari**, **Mahesh Chand Gupta**, and **Pranesh Kumar**, who were always with me during my Ph.D. work. I thank God for showering me with blessings and gifting me with such lovely family and friends.

VIKAS KUMAR

ABSTRACT

Sealants are vital components in Polymer electrolyte membrane fuel cell or PEM fuel cell that prevent the leakage of reactant gases from the perimeter of the cell. The sealants also help to avoid the direct mixing of reactant gases in the cell and provide insulation between the anode and cathode electrode of the cell. The present thesis emphasizes the physical and chemical characteristics of commercial sealant materials silicone rubber, ethylene propylene diene monomer (EPDM) rubber, fluoroelastomer (FKM) rubber, and polytetrafluoroethylene (PTFE). In addition, the time-dependent viscoelastic property, particularly the creep characteristics of PTFE sealant is investigated. In PEM fuel cell, the components are subjected to an assembly pressure of 1–5 MPa, leading to compressive stress in the components. Therefore, the creep response of PTFE sealant is explored at various temperatures in the range of 25–65°C, at three stress levels of 2 MPa, 3 MPa, and 4 MPa. The time-temperature superposition (TTS) method is employed to construct the creep compliance master curve at a reference temperature of 25°C, and thereby, to predict the long-term creep behavior of PTFE sealant. The creep compliance master curve obtained offers the prediction for 4.5 hours. The present thesis further investigates in detail the influence of PTFE sealants' accelerated creep on the performance of a 1cm² active area PEM fuel cell. It is reported that at the cell voltage of 0.4V, the current density for case 1 (without creep) and case 2 (sealants' accelerated creep) are 1.309655 and 1.041806 Acm⁻², respectively. Furthermore, an experimental investigation is carried out to examine the collective impact of relative humidity (RH) and temperature on the dynamic viscoelastic characteristics of EPDM, FKM, and PTFE sealants in PEMFCs. These three sealants are subjected to four different RH conditions of 0, 50, 70, and 90% during the temperature sweep test from room temperature (RT) up to 90°C. Similarly, these sealants are exposed to four different temperatures of 30, 45, 60, and 80°C, during the RH sweep test conducted from 5 to 90% RH. The findings from the dynamic properties, which include the storage modulus (E'), and loss modulus (E'') of the sealants indicate that the degradation of PTFE sealant is the least, while that of FKM sealant is highest, under the combined temperature and RH environmental conditions of PEMFC.

Keywords: *Polymer electrolyte membrane fuel cell, Ethylene propylene diene monomer rubber, Polytetrafluoroethylene, Fluoroelastomer rubber, Viscoelasticity, Accelerated creep, Sealant, Gas diffusion Layer, Hygrothermal, Master curve, Creep compliance, Time-temperature superposition, Prony series.*

TABLE OF CONTENTS

ACKNOWLEDGMENT.....	vii
ABSTRACT.....	ix
LIST OF FIGURES	xvii
NOMENCLATURE	xxiii
ABBREVIATIONS	xxvii
CHAPTER 1.....	1
INTRODUCTION.....	1
1.1 Working principle of a PEMFC	2
1.2 The gaskets/sealants	3
1.3 Design of sealants in PEMFCs.....	4
1.4 Classification of PEMFC sealants based on sealing designs	4
1.4.1 PEM direct sealing design	4
1.4.2 PEM covered frame sealing design	4
1.4.3 MEA covered frame sealing design.....	5
1.5 Classification of PEMFC sealants based on profile	6
1.5.1 Flat gasket/sealant design	6
1.5.2 Profiled gasket/sealant design	6
1.5.3 Formed in place gasket/sealant.....	6
1.5.4 Loose gaskets/sealants.....	6
1.6 Alignment of gaskets/sealants in PEMFCs	7
1.7 Materials.....	7
1.7.1 Silicone rubber.....	8
1.7.2 Fluoroelastomer rubber (FKM1)	9
1.7.4 FKM2 (Viton Â).....	9

1.8 Motivation	10
1.9 Outline of the thesis.....	10
1.10 Closure	11
CHAPTER 2	13
LITERATURE REVIEW	13
2.1 Experimental investigations	13
2.2 Analytical and numerical investigations	18
2.3 Research gap and critical review.....	21
2.4 Objectives of the present work.....	22
2.5 Closure	23
CHAPTER 3.....	25
ASSESSMENT ON PHYSICAL AND CHEMICAL PROPERTIES OF COMMONLY USED LOW AND HIGH-TEMPERATURE POLYMER ELECTROLYTE MEMBRANE FUEL CELL (PEMFC) SEALANTS	25
3.1. Characterization methods.....	25
3.1.1. Acidic ageing environments for sealants.....	25
3.1.2. Alkaline environment for the ageing of sealant samples.....	25
3.2. Properties of sealants in acidic environment.....	26
3.2.1. Physical properties of sealants in acidic environment.....	26
3.2.2. Chemical properties of sealants in acidic environment.....	36
3.3. Properties of sealants in alkaline environment.....	42
3.3.1. Physical properties of sealants in alkaline environment.....	42
3.3.2. Chemical properties of sealants in alkaline environment.....	43
3.4 Physical properties of silicone sealant material in acid and base medium under temperature cycling.....	44
3.5 Testing Standards	46

3.5.1 Sealant material properties	46
3.6 Features of gaskets/sealants in PEMFCs.....	48
3.6.1 Tensile strength.....	49
3.6.2 Chemical and high-temperature stability.....	49
3.8 Closure	56
CHAPTER 4.....	57
THERMOMECHANICAL RESPONSE OF COMMERCIAL SEALANT MATERIALS USED IN PEM FUEL CELLS	57
4.1 Introduction	57
4.2 Material	57
4.3 Experimental Procedure	58
4.4 Results and Discussion.....	58
4.4.1 Creep Test Results	58
4.5 Closure	60
CHAPTER 5.....	61
ANALYTICAL STUDY TO CONDUCT THE TIME-TEMPERATURE SUPERPOSITION (TTS) ON THE EXPERIMENTAL DATA TO OBTAIN THE MASTER CURVE	Error! Bookmark not defined.
5.1 Time-temperature superposition (TTS).....	61
5.3 Non-linear viscoelastic formulations	68
5.3.1 Ascertainment of g_{σ_0} and g_{σ_2}	69
5.3.2 Determination of g_{T_0} and g_{T_2}	70
5.4 Model forecasts	71
5.5 Concluding Remarks	72
5.6 Closure	73
CHAPTER 6.....	75

EVALUATING THE PEM FUEL CELL PERFORMANCE UNDER ACCELERATED CREEP OF SEALANTS.....	75
6.1 Introduction.....	75
6.2 Model description.....	76
6.2.1 Structural model with creep analysis.....	76
6.2.2 Numerical model with flow, thermal and electrochemical analysis	79
6.3 Model assumptions.....	80
6.4 Mesh details.....	81
6.5 Methodology	81
6.5.1 Governing Equations	81
6.6 Boundary conditions	85
6.6.1 Mole fraction at inlet	85
6.6.2 Mass flow rate	86
6.6.3 Modelling variables	86
6.7 Results and Discussion.....	95
6.7.1 Performance curves	96
6.7.2 Transport properties.....	97
6.8 Conclusions	101
6.9 Closure	101
CHAPTER 7	103
INFLUENCE OF HYGROTHERMAL LOADING ON THE DYNAMIC MECHANICAL CHARACTERISTICS OF SEALANTS APPLICABLE TO POLYMER ELECTROLYTE FUEL CELLS.....	103
7.1 Introduction	103
7.2 Methodology	104
7.2.1. Experimental procedure.....	104

7.2.2 Dynamic test with RH accessory.....	104
7.3 Results and Discussion.....	107
7.3.1 Combined effect of RH and temperature on dynamic viscoelastic properties of sealants	107
7.4 Conclusion.....	108
7.5 Limitations of the Report	109
7.6 Closure	109
CHAPTER 8.....	111
CONCLUSIONS AND FUTURE WORK.....	111
8.1 Conclusion.....	111
8.2 Scope for future work.....	112
REFERENCES.....	115
LIST OF PUBLICATIONS	135
BIODATA.....	137

LIST OF FIGURES

Figure 1.1 Schematic showing (a) the components of PEMFC, and (b) working of PEMFC, adapted from (Pehlivan-Davis 2015).....	3
Figure 1.2 (a) Schematic of a PEMFC stack showing (i) Direct sealing design, (ii) PEM covered sealing design, (iii) MEA covered sealing design, and (b) Schematic of a PEMFC stack showing (i) aligned gaskets with gas flow path, and (ii) non-aligned gaskets with the gas flow path.	5
Figure 1.3 Schematic showing the chemical structure of (a) Silicone rubber, (b) FKM1 rubber, (c) EPDM rubber, and (d) PTFE, adapted from (Chen et al. 2018; Kashi et al. 2018; Performance 2009; Restrepo-Zapata et al. 2013).	8
Figure 3.1 Weight change for FKM1, Silicone, and EPDM rubber, adapted from (Lin et al. 2011c; Tan et al. 2011).....	25
Figure 3.2: Showing geometry of (a) Vickers, and (b) Berkovich indenter tips (Hardiman et al. 2017).	27
Figure 3.3 Load-indentation plots for FKM1, Silicone, and EPDM rubber samples, adapted from (Tan et al. 2008e, 2011).....	27
Figure 3.4 Force vs displacement plots for Fluoroelastomer (FKM1), Silicone, and EPDM rubber, adapted from (Tan et al. 2008f, 2009a).....	29
Figure 3.5 Bar charts showing (a) Indentation load (b) Mean contact pressure, and (c) Elastic moduli for FKM1, Silicone, and EPDM, respectively (i) before exposure, (ii) after 35-week exposure at 60°C, and (iii) after 35-week exposure at 80°C to a simulated fuel cell environment (ADT solution), adapted from (Tan et al. 2008e, 2011).....	31
Figure 3.6 (a) Storage Modulus, and (b) Tan δ for FKM1, Silicone, and EPDM rubber samples, adapted from (Lin et al. 2011a; Tan et al. 2011).....	32
Figure 3.7 Showing the spider chart for the physical properties of sealant materials in PEMFCs, adapted from (Tan et al. 2008e, 2009a, 2011).	34
Figure 3.8 Structural change of FKM1, Silicone, and EPDM rubber samples before and after subjecting to the regular solution at 80°C by ATR-FTIR, adapted from (Lin et al. 2011b; Tan et al. 2011).	36

Figure 3.9 Plots showing the concentrations of (a) Calcium and (b) Silicon with time for FKM1, Silicone, and EPDM rubber, subjected to regular and ADT solution at 60°C, and 80°C respectively, adapted from (Lin et al. 2011c; Tan et al. 2009c, 2011).	38
Figure 3.10 showing (a) Tensile strength, (b) % Elongation break, (c) Micro-hardness, and (d) ATR-FTIR plots for the sealant material FKM2 (Viton \hat{A}) subjected to NaOH (10%) at 80°C at different exposure times (1 to 12 weeks), adapted from (Mitra et al. 2004b; a).	41
Figure 3.11 Effect of the acidic, alkaline and air medium on (a) Weight change, and (b) Shore A Hardness of Silicone rubber under temperature cycling from -20°C~90°C, adapted from (Wu et al. 2018b).	44
Figure 4.1 Creep strain plots at temperatures 25–65°C, at stress magnitudes of (a) 2 MPa, (b) 3 MPa, and (c) 4 MPa.	58
Figure 5.1: Shows (a) the experimental setup of the creep test on Electroforce-3310 (TA Instruments) with environmental chamber, (b) enlarged view of the loaded PTFE sample on the tensile test fixture, and (c) PTFE test sample.	61
Figure 5.2 Creep compliance master curves obtained on log-time scale, at 2, 3, and 4 MPa at reference temperature, $T_0=25^\circ\text{C}$	65
Figure 5.3 Shows the master curve obtained at (a) 2 MPa, (b) 3 MPa, and (c) 4 MPa and their respective curve fits to six-term Prony series.	66
Figure 5.4 Shows the shift factors fitted with WLF equation, at a reference temperature, $T_0=25^\circ\text{C}$	67
Figure 5.5 (a) Variation of creep compliance with stress at temperatures of 25-65°C and (b) Variation of creep compliance with temperature at stresses of 2 to 4 MPa.	68
Figure 5.6 The relationship of the non-linear variables (a) g_{σ_0} and (b) g_{σ_2} with stress and their respective curve fits.	70
Figure 5.7 The non-linear variables (a) g_{T_0} and (b) g_{T_2} as an expression of temperature, and their respective curve fits.	71
Figure 5.8 A comparison of the observed and anticipated stresses following one hour of creep at (a) 2 MPa, (b) 3 MPa, and (c) 4 MPa, at various temperatures in the range 25-65°C.	72

Figure 6.1 Creep compliances at various temperatures 25, 35, 45, and 65°C, showing the impact of accelerated creep (MC-65).....	77
Figure 6.2 Structural model of PEMFC showing (a) load and boundary conditions, and (b) Meshed model considered for the creep analysis of PTFE sealant.	78
Figure 6.3 Shows GDL deformation along the length after the (a) static analysis (step-1), and (b) creep analysis (step-2) for the PTFE sealant.....	80
Figure 6.4 Single channel PEMFC model used for simulation	81
Figure 6.5 Single channel performance comparison of the PEM fuel cell for case-1 (no creep) with that of case-2 (sealants' accelerated creep).....	99
Figure 6.6 (i) H ₂ mole fraction variation and (ii) H ₂ O mole fraction variation in anode CL, respectively, at 0.4V for (a) case 1, and (b) case 2.	100
Figure 6.7 (i) O ₂ mole fraction variation and (ii) H ₂ O mole fraction variation in cathode CL, respectively, at 0.4V for (a) case 1, and (b) case 2.	101
Figure 6.8 (i) O ₂ mole fraction variation and (ii) H ₂ O mole fraction variation in cathode GDL, respectively, at 0.4V for (a) case 1, and (b) case 2.....	101
Figure 6.9 (i) Temperature distribution and (ii) Liquid saturation in cathode GDL, respectively, at 0.4V for (a) case 1, and (b) case 2.	102
Figure 6.10 Water content at (i) anode CL and (ii) cathode CL, respectively, at 0.4V for (a) case 1, and (b) case 2.....	102
Figure 6.11 (i) Temperature and (ii) water content variation in the membrane at 0.4V for (a) case 1, and (b) case 2.	103
Figure 6.12 (i) Water content and (ii) Current density (Acm ⁻²) variation at the cathode CL-membrane interface at 0.4V for (a) case 1, and (b) case 2.	104
Figure 7.1 (a) E' and (b) E'' for RH sweep test and (c) E' and (d) E'' for temperature sweep test for PTFE samples.	109
Figure 7.2 (a) E' and (b) E'' for RH sweep test and (c) E' and (d) E'' for temperature sweep test for EPDM samples.	110
Figure 7.3 (a) E' and (b) E'' for RH sweep test and (c) E' and (d) E'' for temperature sweep test for FKM (VITON) samples.....	111

LIST OF TABLES

Table 3.1 Permeability coefficient of the rubber materials according to ASTM D1418 (“Design guide” 2007).	34
Table 3.2 Atomic percentage of elements present on the surface of samples.	40
Table 3.3 XPS results show the atomic % ratios of C, F and O of the surface of FKM2 (Viton \hat{A}) rubber samples without being subjected and after being subjected to the NaOH (10%) solution at 80°C for different times (Mitra et al. 2004a).	44
Table 3.4 Percentage weight loss per cycle of the samples in acidic and basic environments subjected to temperature cycling (Wu et al. 2018b).	46
Table 3.5 Test Methods for the samples (Parsons 2009).	47
Table 3.6 Ex-situ durability test for PEFC sealants at 90°C in H ₂ (At 15psi) (Parsons 2009).	48
Table 3.7 Important physical and chemical properties of gasket/sealant materials in PEMFCs.	51
Table 3.8 Gasket/Sealant materials suitable for LT-PEMFC and HT-PEMFC, depending on the working temperature of the sealants.	56
Table 5.1 Prony series parameters for stress values of 2, 3, and 4 MPa.	68
Table 6.1 Dimensions and material characteristics of 2D PEM fuel cell components	77
Table 6.2 Anisotropic material properties for GDL (Poornesh et al. 2012)	78
Table 6.3 Geometrical dimensions and working environment.	87
Table 6.4 Kinetic, transport and physiochemical properties utilized in the PEM fuel cell model.	88
Table 6.5 The governing equations used for the study	91
Table 6.6 Source terms considered for the PEMFC model (Chippar and Ju 2013; Jiao and Li 2011; Yin et al. 2014)	92
Table 6.7 Mole fraction of reactants taken into account for maximum humidity	94
Table 6.8 Mathematical definitions of the variables used in Eqn (6.22) (Carcadea et al. 2018; Scholz 2015)	94
Table 6.9 Mathematical definitions of the variables used in Eqn (6.23) (Scholz 2015; Wang and Wang 2005; Weber and Newman 2004)	95

NOMENCLATURE

$\varepsilon(t)$	Creep strain	----
σ	Applied Stress	MPa
D_0	Instantaneous creep compliance	MPa ⁻¹
ΔD	Transient creep compliance	MPa ⁻¹
ϕ	Reduced time	----
ϕ'	Reduced time	----
μ_T	Time-temperature shift factor	----
T_0	Reference Temperature	°C
a, g_0, g_1, g_2	Non-linear parameters	----
$g_{\sigma_0}, g_{\sigma_2}, g_{T_0}, g_{T_2}$	Temperature-dependent non-linear parameters	----
$D_0, D_1, D_2, D_3,$ D_4, D_5, D_6	Prony series parameters	----
τ_i	Time Constant	s
c_1, c_2	Constants	----
S_q	Source/Sink term	kgm ⁻³ s ⁻¹
\vec{U}	Velocity vector	ms ⁻¹
M	Molecular weight	kgmol ⁻¹
T	Working temperature of PEM fuel cell	K
P	Working Pressure	Pa
D_0	Diffusivity at STP condition	m ² s ⁻¹
T_0	Standard temperature (298.15)	K
P_0	Standard pressure (101325)	Pa
$D_i^{eff.}$	Effective mass diffusion coefficient	----
$j_{ref.}$	Reference exchange current density	Am ⁻²
J	Volumetric current density	Am ⁻³
E	Activation energy	Jkmol ⁻¹ K ⁻¹

T^{ref}	Reference temperature	K
F	Faraday constant (96,485)	Cmol ⁻¹
R	Universal gas constant (8.314)	Jmol ⁻¹ K ⁻¹
P_x	Partial pressure	Pa
P_z	Water Pressure	Pa
p	Gas Pressure	Pa
p_c	Capillary pressure	Pa
X	Mass Fraction	----
y	Mole Fraction	----
E^r	Reversible potential	V
ΔS	Entropy of Reactions	Jmol ⁻¹ K ⁻¹
V^0	Half-cell potential	V
RH	Relative humidity	%
I_{ref}	Reference current density	Am ⁻²
c	Transfer exponent	----
\dot{m}	Mass flow rate	kgs ⁻¹
A_m	Membrane reaction area	m ²
k_{mem}	Membrane thermal conductivity	Wm ⁻¹ K ⁻¹
M_{eq}	Membrane equivalent weight	gmol ⁻¹
k_s	Thermal conductivity, where s indicates CC, GDL, and CL respectively	Wm ⁻¹ K ⁻¹
θ	Contact angle of GDL/CL	°
Θ	Water removal coefficient	Sm ⁻¹
κ_r	Relative permeability	m ²
b	Constant	----
t_0	Initial GDL thickness	mm
t	GDL thickness after compression	mm
n_d	Osmotic drag coefficient	----
D_w	Diffusion coefficient of water	m ² s ⁻¹

S_v	Mass change rate; v indicates gas to dissolved/liquid to dissolved/gas to liquid phases	$\text{kgm}^{-3}\text{s}^{-1}$
s	Liquid Saturation	----
c_p	Specific Heat	$\text{Jkg}^{-1}\text{K}^{-1}$
d_p^2	Average pore size (10 μm for the present study)	μm
<i>Greek symbols</i>		
ρ	Density	kgm^{-3}
τ	Shear Stress	Pa
μ	Dynamic Viscosity	Pa-s
σ	Electron/Proton conductivity	Sm^{-1}
	Surface Tension	Nm^{-1}
ϕ	Electronic/Ionic potential	V
ψ_0	Initial GDL porosity	----
ψ_f	GDL porosity after compression	m^2
κ_f	GDL permeability after compression	m^2
ω_a	Water Activity	----
η	Surface Overpotential	V
υ	Specific Active Area	m^{-1}
β	Transfer Coefficient	----
ξ	Stoichiometric Ratio	----
ψ	Porosity	----
κ	Permeability	m^2
ν	Kinematic viscosity	m^2s^{-1}
λ	Dissolved Water Content	----
δ	Gas and liquid mass change rate constants/Evaporation and condensation rate coefficients	s^{-1}
$\lambda_{a=1}, \lambda_{s=1}$	Water activity of unity and water content at saturation respectively.	---

Subscripts

q	Subscript for conservation mass, momentum, electronic/ionic charge, energy, species and dissolved water content (multiphase flow).	----
i	Subscript for species/Dry ionomer (membrane)	----
an	Anode	----
cat	Cathode	----
H_2	Hydrogen	----
O_2	Oxygen	----
x	H ₂ , O ₂ , and H ₂ O/saturated water vapour	----
z	Anode and cathode	----
c	Condensation	----
ϵ	Evaporation	----
l	Liquid	----
g	Gas	----
wv	Water Vapor	----
mom	Momentum	----

ABBREVIATIONS

ADT	Accelerated durability test
CL	Catalyst Layer
CC	Current collector
GC	Gas channel
GDL	Gas Diffusion Layer
PEM	Polymer electrolyte membrane
PEMFC	Polymer electrolyte membrane fuel cell
LT-PEMFC	Low-temperature polymer electrolyte membrane fuel cell
HT-PEMFC	High-temperature polymer electrolyte membrane fuel cell
MEA	Membrane Electrode Assembly
DI	Deionized
UV	Ultraviolet
XPS	X-Ray Photoelectron Spectroscopy
ATR-FTIR	Attenuated Total Reflection- Fourier Transformation Infrared Spectroscopy
HTV silicone rubber	High temperature vulcanized silicone rubber
IRHD	International rubber hardness degree
TTS	Time-temperature superposition
HOR	Hydrogen oxidation reaction
ORR	Oxygen reduction reaction
EPDM	Ethylene propylene diene monomer
FKM	Fluoroelastomer (VITON)
PTFE	Polytetrafluoroethylene
DMA	Dynamic mechanical analysis

CHAPTER 1

INTRODUCTION

In the present energy scenario, significant attention is directed towards polymer electrolyte membrane fuel cell (PEMFC). A PEMFC is a device that converts the chemical energy of the reactant gases into electrical energy efficiently. It runs continuously as long as fuel is supplied. Compared to other classes of fuel cells, PEMFCs have a higher power density at low operating temperatures (60–80°C) (Tawalbeh et al. 2022; Zhao et al. 2023). The PEMFCs are classified into two categories depending on the operating temperature. The first is LT-PEMFC, with a working temperature range of 60–80°C. The other is HT-PEMFC, with operating temperature above 120°C, and up to 200°C (Lochner et al. 2020; Rosli et al. 2017; Zhang et al. 2006). LT-PEMFC requires high purity reactant gas and the risk of electrode contamination is higher if impurities are not under control. Therefore, the operating cost is higher for LT-PEMFC as compared to that of HT-PEMFC. The benefits of HT-PEMFCs are improved electrochemical kinetics, better tolerance to reactant gas impurities and improved cooling arrangement due to high operating temperature (Araya et al. 2016; Haider et al. 2021; Zhang et al. 2006).

The efficient utilization of the reactants is key to the prolonged performance of the PEMFC. The sealants are the crucial components that help in the prolonged performance of LT-PEMFC and HT-PEMFC, preventing leakage of these reactant gases. The stability of PEMFC is improved if the sealants are durable enough and withstand the cyclic operating conditions. It is to be noted that the chemical and physical properties of sealants are not clearly understood, especially for cyclic conditions as that of the other components of PEMFCs as in refs (Koorata and Bhat 2021; Poornesh et al. 2010, 2014; Poornesh and Cho 2015). Therefore, the available resources are recollected on the fuel cell sealants to match functionality requirements. This study aims to emphasize on physical and chemical properties of various sealant materials along with their design in PEMFCs. The schematic and the operating of the PEMFC is illustrated in Figure 1.1. The study of various sealant designs as well as materials suitable for PEMFC contributes as a tool for the researchers to assess their

performance in PEMFC working conditions. The chemical degradation of various sealant materials subjected to simulated PEMFC environments helps to better understand the chemical properties of sealant materials in PEMFC conditions. The physical and chemical properties of vital elastomeric sealant materials such as FKM, Silicone, and EPDM rubbers are thoroughly reviewed in the present work. The thesis attempts to provide a comprehensive understanding of the effect of sealant material designs and their properties on the performance of PEMFCs.

1.1 Working principle of a PEMFC

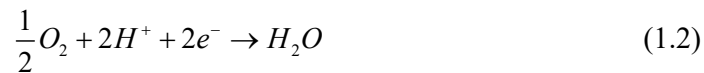
In PEMFC, hydrogen gas advances from the anode towards the active region of the cell. Before reaching the active region, it diffuses through the porous gas diffusion layer (GDL). The catalyst (Pt/Pt Alloy) splits hydrogen molecules into electrons and protons as the hydrogen gas approaches the active region of the cell. The protons are allowed to pass from the active region of the PEMFC, hence the electrons travel through an external electric circuit, which results in the generation of electric current (Pehlivan-Davis 2015).

The reaction at the anode is:



Oxygen gas advances from the cathode side towards the active region of the PEMFC and diffuses through the porous GDL. As soon as it reaches the active region, the catalyst breaks the oxygen molecules into electrons and protons. These oxygen molecules react with the protons transferred from the anode side to form water.

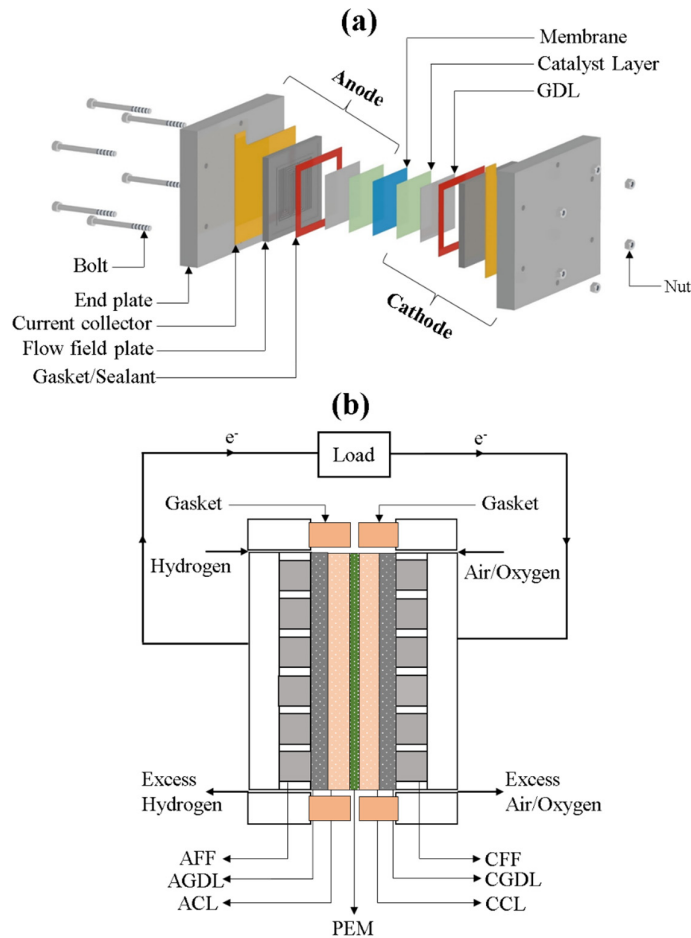
The reaction at the cathode is:



The overall reaction is:



The overall chemical reaction produces electrical energy, water, and waste heat.



AFF: Anode Flow Field, AGDL: Anode Gas Diffusion Layer, ACL: Anode Catalyst Layer, CFF: Cathode Flow Field, CGDL: Cathode Gas Diffusion Layer, CCL: Cathode Catalyst Layer, PEM: Polymer Electrolyte Membrane

Figure 1.1 Schematic showing (a) the components of PEMFC, and (b) working of PEMFC, adapted from (Pehlivan-Davis 2015).

1.2 The gaskets/sealants

Sealants are crucial components assembled on both sides of the membrane in between BPP and the GDL in PEMFCs. The sealants in PEMFCs must possess sufficient strength and hardness to ensure no leakage of reactant gases and coolants from the cell. The sealants in PEMFCs are subjected to an acidic solution, moist air, and compressive

stress between the BPPs (Lin et al. 2011c; Tan et al. 2007a; Wu et al. 2018a; Zhao et al. 2023). Thus, it must sustain these extreme conditions at operating temperatures of (60–80°C) in the case of LT-PEMFC and in the range (120– 200°C) in the case of HT-PEMFC for several thousands of hours. The failure of any single sealant in LT-PEMFC and HT-PEMFC assembly during its operation may lead to the leakage of reactant gases, ultimately compromising the overall performance of the PEMFC (Nah et al. 2015; Yuan et al. 2011). The optimum design of the sealants helps to improve the overall performance of the PEMFC. The sealants' design can be classified based on the sealing structure and sealant profile. PEMFC profile-based sealants include flat gaskets, profiled gaskets, formed-in-place gaskets (FIPG), and loose gasket designs. The schematic of the PEMFC stack showing the various sealant designs is depicted in Figure 1.2(a).

1.3 Design of sealants in PEMFCs

1.3.1 Classification of PEMFC sealants based on sealing designs

Ye et al. (Ye and Zhan 2013) introduced various sealing design in PEMFCs and classified them into the following categories

1.3.1.1 PEM direct sealing design

In this type of sealing design, the size of the PEM is greater than that of GDL, and hence the PEM extends from the active area of the cell. As a result, a sealing border is formed around the cell (Liang et al. 2017; Ye and Zhan 2013). The sealant materials such as PTFE films (Michael M. Walsh 2000), and thermoplastic materials (Stanley P. Bonk, Myron Krasij 2002) are positioned separately on both sides of the PEM sealing edge. During the fuel cell assembly, they are forced together by the clamping force to form a sealing design.

1.3.1.2 PEM covered frame sealing design

Similar to the direct sealing design, in the PEM covered design also, the size of the PEM is greater than that of GDL. Therefore, the PEM extends the active area, and a sealing border is formed around the cell. The main sealing structure of the elements is formed by covering the sealing border of the PEM with adhesive materials. The sealing

border of the PEM is kept in a die, into which the molding sealant materials are injected. After the completion of molding, the sealant materials are shaped, which forms the main structure of the sealing design (Liang et al. 2017; Ye and Zhan 2013).

1.3.1.3 MEA covered frame sealing design

MEA includes membrane, catalyst layer, and the GDL. The sealing border of the MEA is formed by the non-active region surrounding the active area. Similar to the PEM covered sealing design, in this design, the sealing border can be partially or entirely covered by sealant materials. Injection moulded sealant materials are used to cover the sealing border, completing the structure of the integrated MEA (Liang et al. 2017; Ye and Zhan 2013).

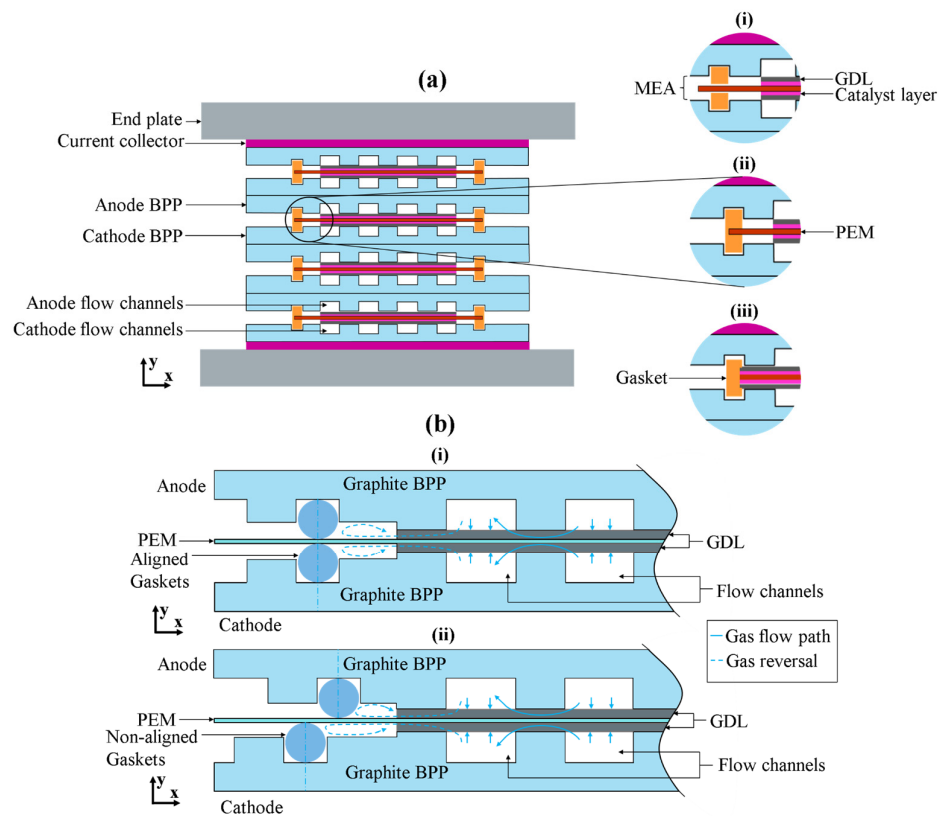


Figure 1.2 (a) Schematic of a PEMFC stack showing (i) Direct sealing design, (ii) PEM covered sealing design, (iii) MEA covered sealing design, and (b) Schematic of a PEMFC stack showing (i) aligned gaskets with gas flow path, and (ii) non-aligned gaskets with the gas flow path.

1.3.2 Classification of PEMFC sealants based on profile

1.3.2.1 Flat gasket/sealant design

Flat gaskets are fabricated with elastomeric sheets of the desired thickness with the help of die-cutters (Charlene Jones, Mike Shorts 2007; Liang et al. 2017; Pehlivan-Davis 2015; Ye and Zhan 2013). This fabrication method is simple, efficient, and economical, but it has some drawbacks. Loss of material in the fabrication process is a major drawback. Furthermore, this method is ineffective in determining the thickness of manufactured sealants.

1.3.2.2 Profiled gasket/sealant design

This fabrication process is used to fabricate sealants of a particular profile. The sealants are fabricated by various moulding processes such as compression, injection, and transfer moulding. These sealants of different profiles can either be attached to the flat surfaces or assembled onto the grooves and channels on flow field plates. Profiled sealants require less assembly force, reducing the risk of damage to other fuel cell components caused by excessive assembly forces (Liang et al. 2017; Pehlivan-Davis 2015; Ye and Zhan 2013).

1.3.2.3 Formed in place gasket/sealant

In this fabrication process, a liquid polymer is applied onto the fuel cell components such as GDL, MEA, and BPP using an automatic applicator (Charlene Jones, Mike Shorts 2007; Liang et al. 2017; Pehlivan-Davis 2015; Ye and Zhan 2013). Temperature and time cause the liquid elastomer to cure and bond to these components. Hence, these gaskets are also called cured-in-place gaskets (CIPG). These gaskets/sealants are fabricated for better compressive force resistance and reduced processing time.

1.3.2.4 Loose gaskets/sealants

Loose gaskets/sealants are chosen in the single-cell assembly, where it has to be manufactured in small quantities. Loose gaskets/sealants allow the form to change based on the sealing conditions and optimize the geometry (Liang et al. 2017; Pehlivan-Davis 2015; Ye and Zhan 2013). Furthermore, mass production of the cost-effective fuel cell necessitates the use of these sealant types in PEMFC.

1.4 Alignment of gaskets/sealants in PEMFCs

The aligned and non-aligned gaskets in PEMFC are explained in Figure 1.2(b). In both aligned and non-aligned gasket configurations, the reactant gases coming from the channels of the BPP and crossing the GDL, flow towards the perimeter of the cell. But, these reactant gases are blocked by the sealants and are prevented from leaking outside (Bhosale et al. 2019; Liang et al. 2017; Ye and Zhan 2013). Hence, both aligned and non-aligned configurations effectively avoid the leakage of the reactant gases in PEMFCs.

1.5 Materials

Most common polymers used as gasket/sealant materials are as mentioned below:

The selection of gasket/sealant material is crucial for designing PEMFC stacks to achieve optimum performance. The elastomeric sealant materials which can withstand the LT-PEMFC and HT-PEMFC working conditions are Silicone, FKM1, and EPDM rubber (Lin et al. 2011a; c; Tan et al. 2007c, 2008e; Wu et al. 2018a). Hardness, thermal stability, stress relaxation, processability, chemical resistance, and mechanical strength are the attributes necessary for sealant materials to be sufficiently durable. The sealant materials in PEMFC must be free of catalyst contamination, which might affect the fuel cell's performance. Also, the sealant material should not contain any component that erodes quickly and blocks the pores in the GDL (Nah et al. 2015). Fluoroelastomers have strong chemical resistance to acids and water, long-term hardness, and low compression set and are anticipated to perform well as a sealant material for PEMFC applications. However, it is not a manufacturer's first choice as it has poor processability in molten state for injection molding and poor low-temperature flexibility (Tan et al. 2008e). Silicone rubber possess a high compression set value, and low chemical resistance in acidic environment, hence it is used as sealant material in PEMFC.

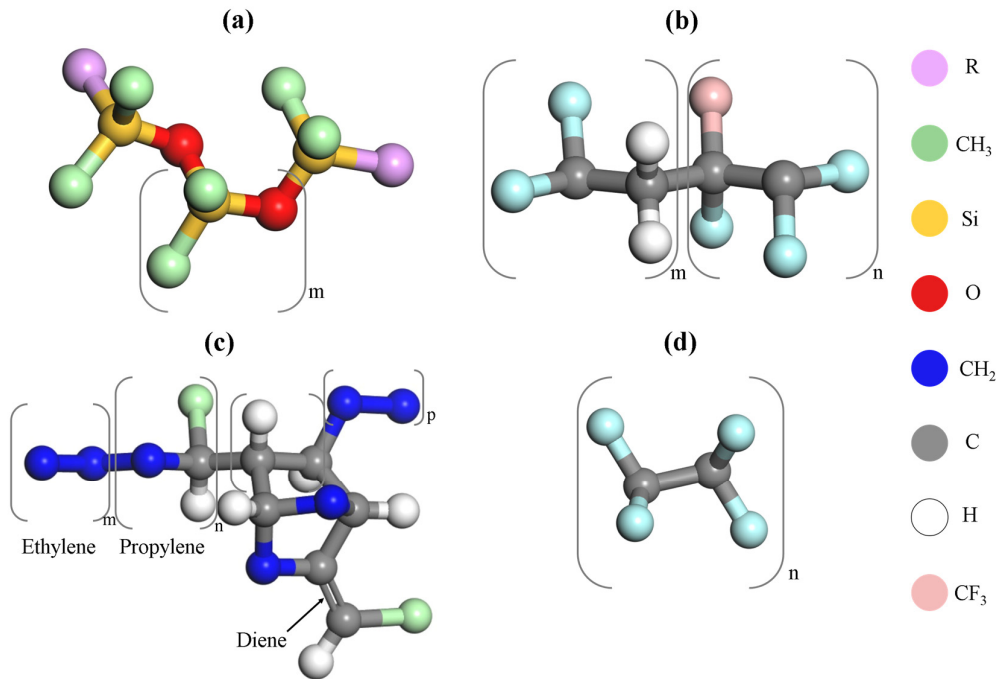


Figure 1.3 Schematic showing the chemical structure of (a) Silicone rubber, (b) FKM1 rubber, (c) EPDM rubber, and (d) PTFE, adapted from (Chen et al. 2018; Kashi et al. 2018; Performance 2009; Restrepo-Zapata et al. 2013).

1.5.1 Silicone rubber

Silicone rubber is an elastomeric material, suitable as gasket/sealant in PEMFCs. Because of its extensive operating temperature range, low cost, and ease of manufacturing, it is used as a sealant material in PEMFCs (Wu et al. 2018a). Silicone rubber's distinctive properties are due to its unique molecular structure, as shown in Figure 1.3(a). Silicone rubber has a unique combination of properties due to the siloxane (Si-O) bond, making it a very good choice for many applications, including the sealant for PEMFCs. These properties include excellent weather and thermal stability, ozone and oxidation resistance, and extreme low-temperature flexibility ($T_g = -120^\circ\text{C}$) (Pehlivan-Davis 2015).

1.5.2 Fluoroelastomer rubber (FKM1)

Fluoroelastomer (FKM1) rubber is prepared from fluorinated rubbers. The molecular structure of FKM1 is shown in Figure 1.3(b). Because of its chemical structure and its natural resilience to acid and heat, FKM1 is chosen as a sealant material in PEMFCs (Lin et al. 2011c; Pehlivan-Davis 2015; Tan et al. 2007b). It offers excellent chemical resistance, particularly in high-temperature applications in various media.

1.5.3 Ethylene propylene diene monomer (EPDM) rubber

EPDM rubber is commonly utilized in insulating components because it has a saturated hydrocarbon backbone and a double bond in the side chains (Mitra et al. 2006d), as shown in Figure 1.3(c). It has inherent resistance to heat, ozone and ultraviolet (UV) light (Lin et al. 2011c; Tan et al. 2007b, 2008f). EPDM rubber has high compression set values and can withstand large compressive loads. It has a working temperature range of -45°C to 120°C , allowing it to withstand the operating temperatures of PEMFCs. EPDM is a versatile polymer, which is resistant to heat, light, ozone, and ultraviolet light. It is commonly utilized in outdoor applications (Nah et al. 2015). EPDM rubber is found to have the highest tensile strength and chemical resistance properties, making it an ideal sealant material for LT-PEMFC and HT-PEMFC.

1.5.4 FKM2 (Viton $\hat{\text{A}}$)

FKM2 sealant material is a commercial grade rubber (Viton $\hat{\text{A}}$), whose constituents are hexafluoro propylene ($\sim 30\%$) and vinylidene fluoride ($\sim 70\%$) co-monomers having Mooney viscosity of 60 (ML-1 +10 at 100°C) (Mitra et al. 2004a). FKM2 (Viton $\hat{\text{A}}$) sealant material is mechanically stable as well as resistant to fuel and heat, which is due to its strong molecular structure (C-F bond, 485 kJ mol^{-1}). Therefore, FKM2 (Viton $\hat{\text{A}}$) is observed as a suitable sealant material for PEMFC operating conditions. The high vinylidene fluoride content in the FKM2 (Viton $\hat{\text{A}}$) material contributes a source of α -hydrogen. The α -hydrogen plays an active role in dehydrofluorination reactions, which happen at high temperature in alkaline environment. The time-dependent study of chemical degradation of FKM2 (Viton $\hat{\text{A}}$) material revealed that de-crosslinking takes place through the hydrolysis process and backbone cleavage takes place due to the dehydrofluorination reactions (Mitra et al. 2004a).

1.6 Motivation

Extensive work is required for enhanced thermomechanical stability and enhanced sealant properties. Comprehending the physical and chemical characteristics of the sealant is critical in improving the performance and longevity of the PEMFC. The sealants' creep under the assembly loading conditions remarkably influences the PEMFC performance. The sealant's dynamic viscoelastic characteristics are key in determining the overall performance and longevity of PEMFC under the hygrothermal conditions. To obtain the improved performance and longevity of the PEMFC, it is required to comprehend the physical and chemical properties of sealants under the PEMFC operational conditions.

1.7 Outline of the thesis

The present thesis is structured as below,

Chapter 1 explains the background and working of the PEMFC. This study explores a vital component of PEMFC, the sealants, which is concisely addressed in this chapter.

Chapter 2 presents a compressive literature review on the physical and chemical characteristics of sealants in PEMFCs. The research gaps identified from the literature aided in framing the present work's objectives.

Chapter 3 reports the physical and chemical properties of various sealants used in PEM fuel cells, that affect the performance of the PEMFC. The physical properties of the sealants include weight loss, hardness, elastic modulus, and hysteresis loss, whereas the chemical characteristics include the chemical composition and chemical structure of the sealants in PEM fuel cell working conditions.

Chapter 4 emphasizes the sealants' creep characteristics in PEM fuel cell conditions. The experimental investigation on PTFE sealants is carried out at various temperatures in the range of 25–65°C, at three stresses of 2, 3, and 4MPa.

Chapter 5 presents the analytical investigation on the PTFE sealant by developing a master curve at a reference temperature of 25°C, utilizing the time-temperature

superposition (TTS) principle. The master curve developed provides the creep compliance prediction for 4.5 hours.

Chapter 6 presents a numerical model to study the impact of sealants' accelerated creep under the PEMFC assembly loading conditions. The Prony series parameters obtained from the compliance master curve are utilized to perform the sealants' accelerated creep analysis in a 2D PEMFC model. Furthermore, this chapter reports the investigation on the influence of the PTFE sealants' accelerated creep analysis on PEMFC performance. The present study is carried out by utilizing a 3D, steady-state, incompressible, and non-isothermal PEMFC model.

Chapter 7 focuses on the dynamic viscoelastic characteristics of various sealant materials (EPDM, FKM, and PTFE) subjected to different hygrothermal conditions. The temperature and relative humidity (RH) sweep tests are conducted at four different relative humidity of 0, 50, 70, and 90% RH and four different temperatures of 30, 45, 60, and 80°C, to study the combined influence of RH and temperature on the dynamic characteristics of sealants.

Chapter 8 presents concluding interpretations of the current study's findings, and confers the scope for future work.

1.8 Closure

The present chapter provided the background and the working principle of the PEMFCs. The chapter also incorporates an introduction to the sealants and their designs, which is the main focus of the study. The framework of the thesis is also presented in this chapter. The following chapter is focused on an extensive literature review of the current research work.

CHAPTER 2

LITERATURE REVIEW

This literature provides a thorough examination of sealants and other components of PEM fuel cells, incorporating experimental, analytical, and computational analyses. It specifically investigates how the characteristics of these components impact the performance of PEM fuel cells, as mentioned below.

2.1 Experimental investigations

Sealants are the essential components in PEMFCs that prevent the leakage of reactants from the edge of the cell. In addition, they prevent the direct confluence of the reactants while providing insulation between the anode and cathode electrodes. An early study by (Mikkola et al. 2007) provided the foundation for sealant materials acceptable for working in PEMFC conditions. They explored several materials, such as EPDM rubber, and EPDM rubber with PTFE, suitable as sealants in PEMFCs. (Pozio et al. 2002) suggested a sealant assembly, which incorporates the membrane in the sealant and eliminates the requirement of protruding the membrane material, resulting in excellent sealing of the stack. (Albert P. Grasso, Vernon; Myron Krasij, Avon; Michael J. Rajpolt 2000) found thermoplastic films such as polyolefin films to be a suitable sealant material, which prevents the water transport from bipolar plates at the periphery of the stack. (Schulze et al. 2004) revealed that there were silicone traces observed on the anode and cathode electrode surfaces, which were caused by the deterioration of the silicone sealants during the PEM fuel cell working. The silicone sealants, which they tested, deteriorated at both the anode and cathode electrodes of the cell. It is revealed from their study that the products of sealants' decomposition are responsible for the deterioration of the catalyst layer.

The investigation by (Majsztrik et al. 2008) incorporated the tensile creep for dry and hydrated Nafion membranes at different temperatures from 23 to 108°C and at a stress of 1.55 MPa. They investigated the viscoelastic response of Nafion membranes at various temperature and relative humidity (RH) conditions. In a similar manner, (Han et al. 2020) explored the creep behavior of fluoroelastomer in acidic environments. The

key findings from their study are that the creep strain raised with an increase in temperature and concentration of the acidic environment to which the material was subjected before the test. In PEMFCs, the sealants undergo compressive mechanical loads in addition to high temperatures between 60 and 80°C during operations. As a result, the characterization of sealants under thermomechanical loading is essential to ensure sealants' design and longevity in PEMFC operating conditions. (Habibnia et al. 2016) investigated the influence of clamping force, endplate thickness, and the depth of sealant groove on the uniform pressure distribution over the gas diffusion layer (GDL) in PEMFC. Their findings disclosed that a minimum compression pressure of 2 MPa is adequate for ensuring the effective sealing of components.

Elastomeric sealant materials undergo thermal and irradiative deterioration under the operating conditions of PEMFC. For example, (Youn and Huh 2005) observed that the surface of the high-temperature vulcanized (HTV) Silicone and EPDM rubbers depreciated in the presence of accelerated ultraviolet (UV) conditions. (Mitra et al. 2004a) evaluated the chemical degradation of FKM rubber with time, in an alkaline (10% NaOH, 80°C) environment. Similarly, (Basuli et al. 2012) analysed the performance and degradation mechanisms of silicone, FKM, and EPDM sealants in PEMFCs. (Van J.W. 2006) observed that the chemical and mechanical deprivation of silicone, EPDM and Fluoroelastomer sealants occurs in a simulated PEMFC environment. They explained the material degradation process with morphological and weight changes, leachates, and Fourier transform infrared spectroscopy (FTIR) results. The physical and chemical degradation characteristics of the elastomeric sealant materials are investigated in simulated PEMFC environments in refs (Lin et al. 2011b; Tan et al. 2007a, 2008a, 2009c, 2011). Furthermore, Cui et al. (Cui et al. 2011) studied the stress relaxation behavior of liquid silicone rubber (LSR) at fixed strain. They predicted the estimated service life of LSR using the time-temperature superposition (TTS).

The functional characteristics of polymeric sealants in PEMFCs are influenced by two key environmental factors; relative humidity (RH) and temperature. Various studies in the literature have emphasized the impact of humidity and temperature on the viscoelastic characteristics of polymers. For example, Hu et al. (Hu et al. 2013)

conducted the dynamic mechanical tests subsequent to subjecting the materials to specified humidity (0–60% RH) and temperature (10–60°C) settings during the temperature and RH scans, respectively. They investigated the plasticizing effect on materials' characteristics caused by the presence of humid environments. Furthermore, a thorough investigation is done on how the viscoelastic characteristics of PVA are influenced by the combined effect of temperature and RH.

In literature, several studies have focused on the dynamic mechanical characteristics of elastomers subjected to hygrothermal conditions, with the help of DMA. (Konidari et al. 2011) carried out differential scanning calorimetry (DSC) to investigate the impact of humidity on the mechanical characteristics of Poly (vinyl alcohol) (PVA) films. Their research revealed that raising the water content in PVA caused a reduction in the elastic modulus, tensile strength, and glass transition while simultaneously increasing the loss tangent ($\tan \delta$) of the polymer material. Similarly, (Park et al. 2001) explored the DMA characteristics of PVA under dry and humidified conditions within a temperature range of -20 to 260°C. (Porte et al. 2023) examined the mechanical properties of four elastomeric materials frequently used in soft robotics. Especially, they analyzed the stress-relaxation characteristics of these materials at temperatures of -40 to 80°C, as well as under different humidity conditions ranging from 5 to 95% RH. (Tan et al. 2011) explored the dynamic mechanical properties of commercial silicone S sealant under simulated PEMFC conditions, with a temperature spanning from -70 to 90°C. Similarly, (Lin et al. 2011d) examined the dynamic characteristics of five polymers that can be used as sealants in PEMFC by utilizing DMA in a simulated PEMFC environment at 80°C. A study by (Swaminathan and Shivakumar 2009) explored the dynamic characteristics of glass/epoxy and carbon/epoxy composites under various temperature conditions. (Jansen et al. 2020) conducted the DMA on the epoxy compound set at five different temperatures of 20, 40, 60, 80, and 85°C, and kept the duration of humidity steps for 4 hours. Similarly, (Alawsi et al. 2009) explored the impact on the mechanical characteristics of polymer composites when they are subjected to high relative humidity (98% RH) conditions. A study by (Henriques et al. 2018) conducted a comparison of complex modulus in various working modes provided by various DMA apparatuses. However, there is a lack of research work on the

collective impact of RH and temperature on the dynamic characteristics and, thereby, on the longevity of gaskets/sealants in PEMFC working conditions.

The polymeric sealant's material selection is crucial for determining its endurance, which ultimately affects the longevity and performance of the PEMFCs. Therefore, the current investigation emphasizes the cumulative influence of RH and temperature on the dynamic characteristics of FKM and EPDM rubber and Polytetrafluoroethylene (PTFE) in PEMFC working conditions. Moreover, these three sealant materials are compared for their dynamic properties in the PEMFC operating conditions. FKM rubber, commercially known as VITON, has a broad range of applications, for example, in the automobile sector, apart from sealing applications in the aerospace industry. EPDM rubber possesses an inbuilt resistance to heat, ozone, and ultraviolet (UV) radiation (Améduri et al. 2001; Mitra et al. 2006a). PTFE is an evolving material suitable for harsh working conditions with temperatures ranging from -150 to 300°C (Wang et al. 2016). An investigation by (Li et al. 2018a) explored the PTFE-based fabric composites for their dynamic mechanical properties in the range of 30–225°C. To the best of the authors' information, no record of prior investigation has quantitatively assessed the collective impact of RH and temperature on the dynamic viscoelastic characteristics of EPDM, PTFE, and FKM sealants in PEMFC working conditions.

When subjected to axial strain along with various hygrothermal conditions, the sealants tend to degrade at a faster rate, due to the de-crosslinking and weakening of polymer chains (Kumar et al. 2022b; Tan et al. 2008b). In this prospect, the physical and chemical degradation of silicone and EPDM rubber gaskets/sealants under the operating conditions of a PEMFC is examined in the refs (Tan et al. 2007a, 2008c, 2009b). The findings from these investigations indicate that the aforementioned compound undergoes rapid degradation in a simulated PEMFC working condition. Similarly, the physical characteristics of silicone, ethylene propylene diene monomer (EPDM) and fluoroelastomer (FKM) rubber are examined utilizing the DMA in refs (Cui et al. 2011; Tan et al. 2008f, 2011). In PEMFC working conditions, the mechanical and chemical deterioration of Silicone and EPDM rubber-based gasket/sealant compounds are investigated in refs (Tan et al. 2007a, 2008c, 2009b). It was inferred

that the silicone-based compound degraded rapidly in various aqueous solutions, similar to PEMFC working conditions. The fillers in these compounds, such as silicon dioxide, calcium carbonate, and magnesium oxide were attacked by the solution. As a result, elements such as silicon, calcium, and magnesium leach out of sealant material, lowering the electrochemical performance of the PEMFCs (Tan et al. 2007a, 2008c, 2009b). Micro indentation test and dynamic mechanical analysis (DMA) were carried out to investigate the mechanical properties of Silicone, EPDM and FKM rubber in refs (Lin et al. 2011b; a; Tan et al. 2008f, 2011). The chemical and mechanical steadiness of sealant materials ensures the improvement in durability and performance of the PEMFCs. The chemical and mechanical properties of sealants are studied in order to investigate the performance of PEMFCs in refs (Husar et al. 2007; Yuan et al. 2011). The chemical degradation of the sulphur and peroxide-cured EPDM rubber in a 20% Cr/H₂SO₄ acidic environment was investigated in refs (Mitra et al. 2006b; c). It is revealed from their study that both the sulphur and the peroxide-cured EPDM undergo chemical degradation due to the de-crosslinking process. Importantly, the chemical and mechanical stability of polymeric sealants promotes the longevity and performance of the PEMFCs. Therefore, the authors have concentrated on the dynamic characteristics of sealants under the operating PEM fuel cell conditions.

The gaskets/sealants in PEMFCs usually possess viscoelastic characteristics. These sealants are required to possess flexibility to accommodate the compression of the fuel cell, ensuring appropriate contact among all components (Lin et al. 2011d). Therefore, the dynamic mechanical characteristics i.e. storage modulus (E'), loss modulus (E''), and loss tangent ($\tan \delta$) of the polymeric sealants play a vital role in determining their functionality. E' represents the elastic energy storage capacity, E'' represents the material's energy dissipation capacity, and $\tan \delta$, the ratio of E'' to E' , measures the material's damping capability. It is noteworthy that when the sealant experiences changes in its dynamic characteristics (due to the environmental conditions of RH and temperature) with time, it may be deprived of its sealing capability and consequently influence the longevity of the PEMFC.

Examining different sealant designs and materials appropriate for PEMFC serves as a means for researchers to evaluate their performance in the PEMFC operating

environment. Studying the chemical degradation of different sealant materials in simulated PEMFC environments provides valuable insights into the chemical characteristics of sealant materials under PEMFC conditions. The present thesis provides a comprehensive study of the physical and chemical characteristics of important elastomeric sealant materials, including Silicone rubber, FKM rubber, EPDM rubber, and PTFE.

2.2 Analytical and numerical investigations

The proper design and development of models for the sealants can also be approached similar to other components (Padavu et al. 2021b; Shinde and Koorata 2022), and this can be very crucial for the improvement of the overall performance of PEMFCs. Also, the selection of sealant material is a crucial process and depends upon the design and application of PEMFCs (Chang et al. 2016; Shinde and Koorata 2021b; Wu et al. 2008). (Lee et al. 2005) proposed a stack assembly to find out the bipolar plate (BPP) thickness, sealant dimensions, and the clamping pressure required in a PEMFC. Similarly, the physical and transport properties of various components of PEMFCs are studied in refs (Poornesh et al. 2014; Poornesh and Cho 2011b, 2015).

In the literature, much of the researches on the impact of compression/assembly pressure have focused on the gas diffusion layer (GDL) and its influence on cell performance (Bouziane et al. 2020; Ceballos et al. 2022; Koorata and Bhat 2022; Padavu et al. 2023; Poornesh et al. 2010; Poornesh and Cho 2011a; Shinde et al. 2023; Yang et al. 2021). A study by (Zhou and Wu 2007) examined the effect of GDL compression on PEMFC performance. An investigation by (Ceballos et al. 2022) examined the impact of tortuosity on the polarization curve in the case of a single-channel PEMFC model. A numerical study conducted by (Shinde et al. 2023) investigated how the PEMFC performance is impacted by the relative humidity (RH) and the inhomogeneous gas diffusion layer properties. (Padavu et al. 2021a) performed a numerical investigation to assess the influence of flow channel design in the case of uniform and inhomogeneous GDL compression on PEMFC performance. Similarly, (Li and Sundén 2018) explored the impact of GDL compression on fuel cell performance utilizing a 3D model. They revealed that PEMFC performance is enhanced due to the increased assembly pressure. (Um and Wang 2004) investigated the effect of operating

pressure, operating temperature, and relative humidity (RH) on PEMFC performance experimentally. (Huang et al. 2010) incorporated a 3D, non-isothermal, two-phase model, to analyze how the porosity difference in the GDL affects the PEMFC performance. Similarly, (Zhou et al. 2013) explored the effect of assembly pressure on the GDL and membrane properties and, therefore on the PEMFC performance. As far as the authors are aware, there is no reported work on the impact of sealant response to external factors on cell performance.

Polytetrafluoroethylene (PTFE), one of the sought-after sealant materials, is used in various industrial fields as gaskets, valves, wire insulation, and surface coatings due to its excellent mechanical characteristics as well as chemical inertness (Dasappa et al. 2009b; Jeya and . 2021). PTFE has the inbuilt viscoelasticity characteristic, indicating that its mechanical characteristics vary with time and temperature. Creep and stress relaxation are two important time-varying deformation characteristics of viscoelastic materials that are caused by constant loading at high-temperature conditions (Allen et al. 2001; Betten, and Tsang, 2003; Hiel et al. 1984; Shaw and MacKnight 2005; Stan and Fetecau 2013). In recent decades, there have been many research works dedicated to studying the mechanical properties of PTFE. (Bharadwaj et al. 2017) utilized the finite element method (FEM) approach to investigate the behaviour of PTFE gaskets in flange joints. By implementing Burger's model, they focused on the stress relaxation properties of PTFE sealants. Many researchers have developed the master curves utilizing the time-temperature superposition (TTS) method with the Williams-Landel-Ferry (WLF) equation for predicting creep compliance characteristics of various polymers and polymer composites (Mahdavi et al. 2018; Nomula et al. 2019; Ollier et al. 2021; Tábi et al. 2019). Few research works have been conducted on the creep characteristics of polymeric materials utilizing the Burger model and Modified Burger model (Kurt and Kasgoz 2021; Ye et al. 2021). Researchers have been particularly interested in developing a viscoelastic model that uses the TTS principle to predict the creep characteristics of polymer and polymer-based composites. An early investigation by (Xiao et al. 1994) emphasized modelling the viscoelastic creep properties of PEEK composite material. They explored the viscoelastic properties with the help of TTS and the time-stress superposition (TSS) principle. Similarly, (Allen et al. 2001) constructed

a linear viscoelastic model to analyze and forecast the creep properties of polypropylene GMT components. The findings from their investigation showed that the viscoelastic model results fitted the experimental results in most of the cases. Similarly, (Dasappa et al. 2009a) established a constitutive model for the creep characteristics of a glass mat thermoplastic (GMT) material. They developed a long-term creep model utilizing the TTS principle.

Sealant creep may occur due to cyclic (hygrothermal) or direct loads (mechanical compression); the former is expected to have originated from membrane or GDL and it may have negligible influence on the magnitude of overall creep. It is noteworthy, however, that many researchers have reported on the significance of such cyclic loads in the membrane and GDL on the stability and hence cell performance. A study by (Koorata and Bhat 2020) explored the cyclic mechanical response of GDL under low altering stresses. The creep response of Nafion membrane is well reported in refs. (Arthurs and Kusoglu 2021; Shi et al. 2013; Xia et al. 2018; Zhang et al. 2019). The aforementioned investigations on membrane creep provided insights into the stability and durability of the membrane, and, thereby, impact on PEMFC performance. It provided a motivation for the current study as the sealants are exposed to similar loading and thermal conditions in PEMFC. Similarly, the effect of mechanical loading on various PEMFC components' physical and transport properties is investigated in the refs (Bhosale et al. 2019; Kumar et al. 2022a; Padavu et al. 2021b; Poornesh et al. 2013, 2014; Poornesh and Cho 2011b, 2015; Shinde and Koorata 2021a). It is essential to congregate all the resources currently accessible on the sealants' creep (due to compressive loading) in the PEMFC working environment. Therefore, the authors are interested in the sealants' creep response resulting from compressive loading conditions, on the longevity and performance of the PEMFC. The prediction of creep behavior at elevated temperatures (accelerated creep) in a shorter time interval is achieved by developing a master curve, at a specified temperature, utilizing the time-temperature superposition (TTS) technique. The master curve thus obtained mimics the creep compliance results for a prolonged period. A recent study by (Kumar and Koorata 2024) explored the creep behavior of PTFE sealants in the temperature range of 25-65°C, wherein the authors addressed the effect of sealants' creep that occurred due to

the assembly loading conditions. They utilized the TTS technique to develop a master curve, that provides creep compliance prediction for 4.5 hours.

The thesis work investigates in detail the influence of PTFE sealants' accelerated creep on transport properties, thereby, on PEMFC performance, by incorporating an incompressible, three-dimensional, non-isothermal, steady-state and multiphase flow model. The motive of the present work is to acquire a comprehensive knowledge of the performance of PEM fuel cells, as a result of accelerated creep in sealants. The findings from this study will serve as a useful tool in establishing a link between sealants' creep and the PEMFC performance.

2.3 Research gap and critical review

In the literature, no research is related to the sealants' creep characteristics in PEMFC conditions. PTFE sealants are not investigated for their creep characteristics as the previous studies have focused mostly on other PEMFC components such as Nafion Membrane (Majsztrik et al. 2008), apart from polymer-based composites (Mahdavi et al. 2018). The mechanical characteristics, including the creep of sealants, are not as well understood in the published research as those of the other PEMFC components investigated in refs. (Baik et al. 2013; Koorata and Bhat 2021; Poornesh et al. 2010, 2013, 2014; Poornesh and Cho 2011b, 2015; Shinde and Koorata 2021b, 2022). In the same manner, the various PEMFC components' physical and transport properties are investigated in the refs.(Irmscher et al. 2019; Koorata and Bhat 2021; Padavu et al. 2021b; Poornesh and Cho 2011b, 2015; Shinde and Koorata 2021a, 2022). Therefore, it is essential to gather all the currently available resources regarding the mechanical characteristics of PEMFC sealants.

It is clear from the extensive literature that the sealants' creep and dynamic viscoelastic characteristics are of prime research potential from the application point of view in PEMFCs. Therefore, a thorough study in this field is essential. There is a requirement to develop the creep compliance master curve for sealants using the TTS approach, which can give the creep compliance prediction for a longer duration, as shown by ref. (Dasappa et al. 2009a). Also, there is a need to develop the creep compliance master

curve, that can be utilized to model the sealants' accelerated creep at higher temperatures applicable to PEM fuel cell conditions.

The detailed creep response of PTFE sealants is investigated by incorporating TTS principle and WLF equation and, thereby, developing master curve for creep compliance. The creep compliance master curve thus obtained forecasts the long-term behaviour of PTFE sealants, which is not easily accessible under the test conditions. It is evident from the literature that such detailed creep analysis is not available for PTFE sealants in PEMFCs. The viscoelastic creep compliance model developed in the study would be helpful for its potential high-temperature applications, such as in HT-PEMFCs. Although the clamping pressure results in a compressive load, the creep test on the sealant material has been carried out under tensile loading conditions at stresses of 2, 3, and 4MPa. The temperature dependency of the viscoelastic behavior is studied by performing creep experiments on PTFE sealant at higher temperatures. The methodology for studying the temperature dependency of viscoelastic behavior through creep experiments is to develop a master curve (utilizing the TTS approach) to forecast the long-term creep compliance results for PTFE sealant at higher temperatures. The impact of stress and temperature on the creep characteristics of PTFE sealants are investigated in the present study. Moreover, some important factors, such as relative humidity (RH) conditions and exposure time to creep loading, could impact the sealants' creep characteristics. Therefore, the investigation is extended by conducting dynamic tests that incorporate RH and temperature sweep tests, for studying the viscoelastic characteristics of PTFE, EPDM and FKM sealants in PEMFC working conditions.

2.4 Objectives of the present work

The primary objectives of the present work are:

1. To experimentally investigate the thermomechanical response of commercial sealant materials used in PEM fuel cell.
2. To implement an analytical study to conduct the time-temperature superposition (TTS) on the experimental results to obtain the master curve.

3. To numerically investigate the creep response of sealants under PEM fuel cell assembly loading.
4. To investigate the influence of sealants' accelerated creep on the PEM fuel cell performance.
5. To experimentally investigate the combined impact of temperature and relative humidity (RH) on the characteristics of PEM fuel cell sealant.

2.5 Closure

This chapter outlines the objectives of the present study, which have been identified by an extensive review of existing literature and the identification of research gaps. The next chapter includes an assessment of the physical and chemical characteristics of commercial sealants under the operating conditions of PEMFC.

CHAPTER 3

ASSESSMENT ON PHYSICAL AND CHEMICAL PROPERTIES OF COMMONLY USED LOW AND HIGH- TEMPERATURE POLYMER ELECTROLYTE MEMBRANE FUEL CELL (PEMFC) SEALANTS

The physical and chemical characteristics of the commercial sealants are critical in deciding the overall performance and longevity of the PEMFCs. The following characterization methods are thoroughly explored for improving the thermomechanical stability of commercial sealants under the PEMFC working conditions.

3.1. Characterization methods

3.1.1. Acidic ageing environments for sealants

In literature, it is found that two solutions are used to show the ageing of sealant materials. The first is an accelerated durability test (ADT) solution, which is used to accelerate the ageing of material over a short period of time. It is comprised of 48% HF and 98% H₂SO₄ dissolved in reagent grade water. The constituents of this ADT solution are 1M H₂SO₄, 10ppm HF, and reagent grade water having 18MΩ resistances (Lin et al. 2011b). The pH value of this solution is less than one. The second solution is termed as regular solution. The chemical composition of this solution is 12ppm H₂SO₄ and 1.8ppm HF, with reagent grade water having 18MΩ resistances. The final solution has a pH value of 3.35, which is close to the PEMFC working conditions (Lin et al. 2011b).

3.1.2. Alkaline environment for the ageing of sealant samples

A simulated environment is created by dissolving the highly pure NaOH in DI water to prepare 10% solution having pH value of 14.5 (Mitra et al. 2004a). The FKM2 (Viton \hat{A}) samples are subjected to this alkaline environment at 80°C for different time duration (i.e. from 1 to 12 weeks), and their physical and chemical properties are studied.

3.2. Properties of sealants in acidic environment

3.2.1. Physical properties of sealants in acidic environment

3.2.1.1. Weight change

The sealant material specimens are taken from the test enclosure at specific periods to evaluate weight loss. The percentage weight loss, WL, is calculated as

$$WL = \frac{W_i - W_f}{W_i} \times 100 \quad (3.1)$$

Where W_i is the initial weight of the sample in air, and W_f is the weight of the aged sample in air.

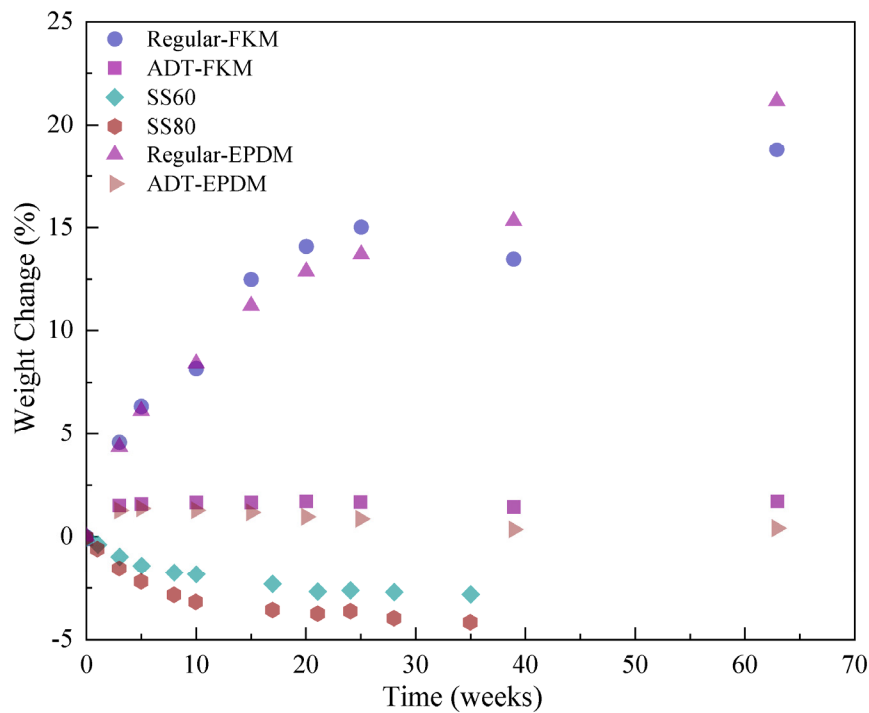


Figure 3.1 Weight change for FKM1, Silicone, and EPDM rubber, adapted from (Lin et al. 2011c; Tan et al. 2011).

It is found that EPDM and FKM1 rubber samples gained weight consistently over time in regular solution whereas their weight remained almost the same in ADT solution, as shown in Figure 3.1. The reason for their weight gain is the formation of crystals of $MgSO_4$ on the surface of EPDM and FKM1 samples when they are subjected to the regular and ADT solutions. The formation of these crystals is found to be more in regular solution (Lin et al. 2011b). A higher acid concentration in the ADT solution apparently corrodes the material more than the regular solution. For the silicone rubber subjected to the regular solution, weight loss increases with exposure time at temperatures $60^\circ C$ and $80^\circ C$. The weight loss for the Silicone samples is more at $80^\circ C$ than at a temperature of $60^\circ C$, showing the effect of high temperature. The weight change results indicate that FKM1 and EPDM rubber samples are better than the Silicone rubber as the material degradation is more in the case of Silicone rubber in PEMFC operating conditions.

3.2.1.2. Indentation load

The indentation test gives an indentation load-displacement curve. The stainless steel ball used as the indenter tip for the indentation test typically has a radius of 1.98 mm. The apparatus has a 0.5 mN force resolution and a 0.1 μm displacement resolution. On each rubber material, 3–4 indentations are made, as mentioned in the literature. A peak indentation depth of 0.22 mm is employed for the samples for displacement control in refs. (Tan et al. 2008e, 2011).

Vickers and Berkovich indenters are the commonly used indenters for microhardness measurements, which have the geometry of four side or three side pyramid respectively. These indenters are mainly calibrated by optical microscopes which measure the angles between the pyramid planes. The angles between the pyramid planes i.e. the rated angle between opposite planes is $\alpha=136^\circ$ for Vickers indenter and the angle between the pyramid plane and the symmetry axis of the indenter i.e. the rated angle is $\alpha=65.35^\circ$ for Berkovich indenter, respectively (Herrmann et al. 2001). Figure 3.2 shows the geometry of Vickers and Berkovich indenter tips.

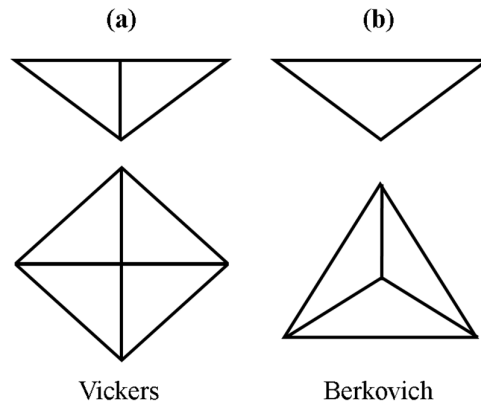


Figure 3.2: Showing geometry of (a) Vickers, and (b) Berkovich indenter tips (Hardiman et al. 2017).

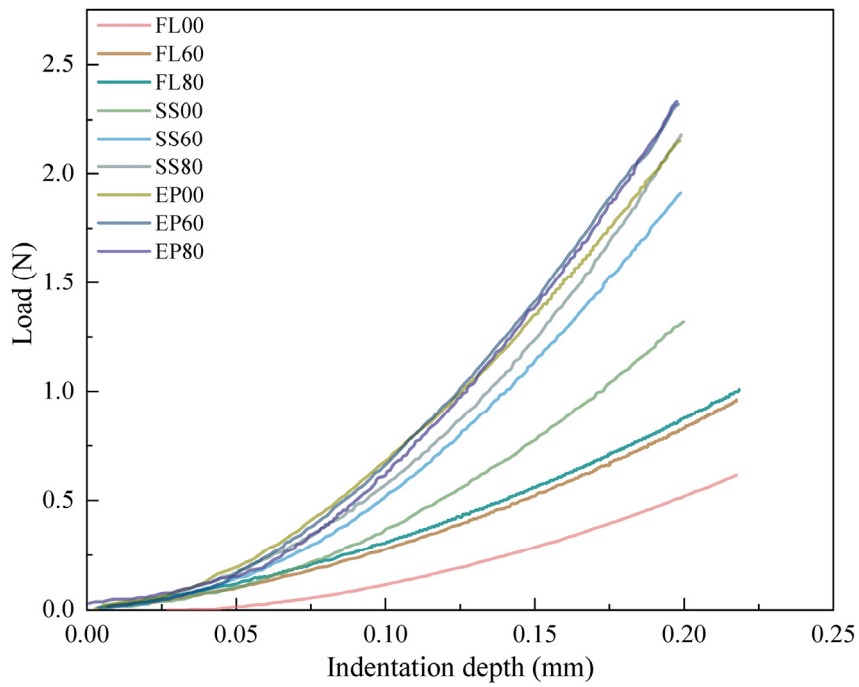


Figure 3.3 Load-indentation plots for FKM1, Silicone, and EPDM rubber samples, adapted from (Tan et al. 2008e, 2011).

In Figure 3.3, FL00, FL60, and FL80 indicate Fluoroelastomer (FKM1) samples without exposure and after exposure for 47-weeks at 60°C and at 80°C to the ADT solution, respectively. Similarly, SS00, SS60, and SS80 signify the Silicone S rubber samples without exposure, after 35-week exposure at 60°C, and after 35-week exposure at 80°C, to the ADT solution, respectively. EP00, EP60, and EP80 represent EPDM samples without exposure, after exposure for 47-weeks at 60°C, and at 80°C, to the ADT solution, respectively. The load versus indentation depth results disclose that the indentation of samples increases with temperature at a constant indentation depth. Therefore, the samples subjected to the ADT solution at 80°C are found to have the maximum load, followed by the samples at 60°C, and finally samples which are not subjected to the ADT solution. These results indicate the effect of temperature and environment both. The rise in indentation load at a constant indentation depth indicates that FKM1 and Silicone rubber samples get hardened with temperature when they are subjected to the simulated PEMFC conditions (Tan et al. 2008e). According to the results shown in Figure 3.3 and 3.5(a), the indentation load for EPDM samples did not change considerably with temperature, indicating that the EPDM rubber samples did not degrade with increasing temperature and with exposure to the ADT solution. Therefore, EPDM rubber shows better results than the FKM1 and Silicone rubber samples in PEMFC operating conditions.

3.2.1.3. Cyclic loading of sealants

In Figure 3.4, the load-displacement plots show the cyclic loading conditions for FKM1, Silicone, and EPDM rubber samples at 60°C and 80°C without applying the load. It shows load-displacement results for these sealant materials before and after exposure to the ADT solution for 45–47 weeks. FL00, FL60, and FL80 indicate Fluoroelastomer (FKM1) samples without exposure, after exposure for 47-weeks at 60°C, and at 80°C, to the ADT solution. The results for FKM1 rubber show that unloading curve does not coincide with the corresponding loading curve, indicating the hysteresis property of material. SS00, SS60, and SS80 represent the Silicone S rubber samples without exposure, after exposure for 45-weeks at 60°C, and at 80°C, to the ADT solution. The elastomeric materials possess a particular characteristic known as Hysteresis (Mark et al. 1984). This characteristic represents loss of energy and

overheating in polymers, and it is caused due to the viscoelastic property of polymers (Ferry 1980; Menard 1999). The area covered by the loading curve represents the energy applied, and the area covered by the unloading curve represents energy recovered. The area between the two curves (between loading and unloading curves in Figure 3.4) represents the energy loss due to hysteresis. In Figure 3.3, EP00, EP60, and EP80 represent EPDM samples without being subjected, after being subjected for 47-weeks at 60°C, and at 80°C, to the ADT solution, respectively. It is evident that the hysteresis energy loss changes significantly with exposure time and increasing temperature for FKM1, Silicone, and EPDM rubber samples. The results indicate that the viscoelastic characteristics of FKM and Silicone rubber samples changes significantly, but for EPDM rubber samples, it remains almost the same with the exposure medium and with increasing temperature. Therefore, EPDM rubber is found to be more stable sealant material as compared to the FKM1 and Silicone rubber in PEMFC working conditions.

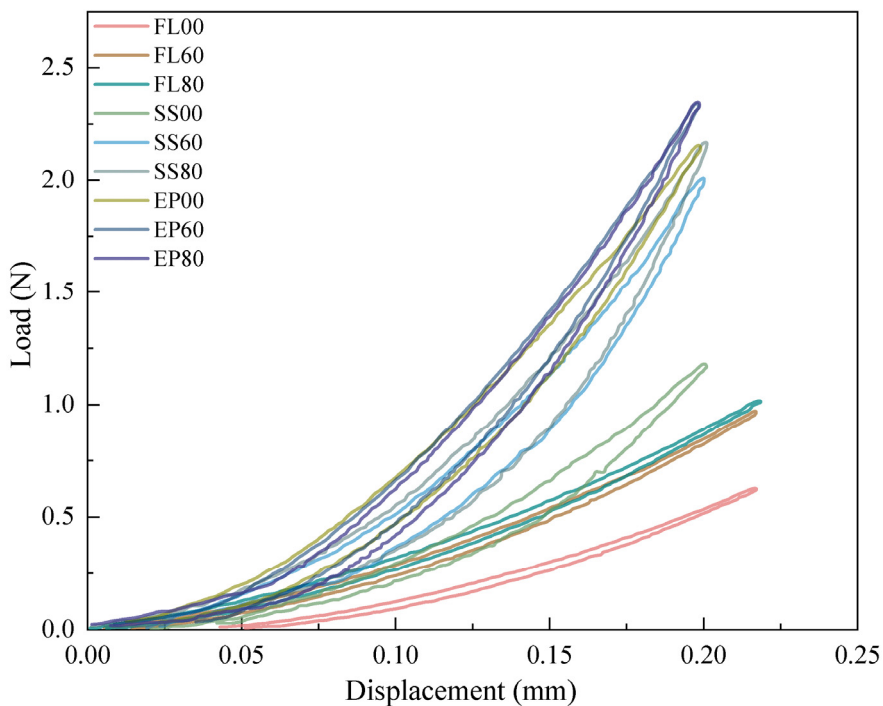


Figure 3.4 Force vs displacement plots for Fluoroelastomer (FKM1), Silicone, and EPDM rubber, adapted from (Tan et al. 2008f, 2009a).

3.2.1.4. Hardness (Mean contact pressure)

Hardness or Mean contact pressure is given by the load upon the projected area of contact (Li and Bhushan 2002), i.e., the magnitude of load, which a material is able to withstand at a given displacement. As shown in Figure 3.5(b), the hardness for the FKM1 and Silicone rubber samples increased significantly with temperature, without any load application. These results agree with indentation load and elastic modulus results shown in Figure 3.5(a) and 3.5(c), respectively. In the case of EPDM rubber samples, the hardness did not change considerably with exposure time and with increasing temperature. The hardness results for EPDM rubber samples agree with the maximum indentation load and elastic modulus results, as shown in Figure 3.5(a) and 3.5(c), respectively. Therefore, it is very clear that EPDM rubber does not degrade with increasing temperature and is found to be more stable than FKM1 and Silicone rubber in PEMFC working conditions.

3.2.1.5. Elastic Modulus

The elastic modulus is a mechanical property that is used to define the elastic deformation behavior of sealants in PEMFC. It is clear from Figure 3.5(c) that the FKM1 and Silicone rubber samples exposed to the ADT solution at 80°C have the highest elastic modulus, followed by the samples at 60°C, and then the samples without exposure to the solution. These results specify that the elastic modulus for the FKM1 and Silicone rubber increases due to increasing temperature in the exposure medium (Tan et al. 2008e). In all three conditions, i.e., without exposure, after exposure for 47-weeks at 60°C, and at 80°C to the ADT solution, the elastic modulus for EPDM samples is almost similar. Therefore, the results suggest that the EPDM rubber samples have much better stability as compared to FKM1 and Silicone rubber samples in PEMFC working conditions. Also, these results are found to be consistent with the load-indentation and hardness results as shown in Figure 3.3 and 3.5(b), respectively.

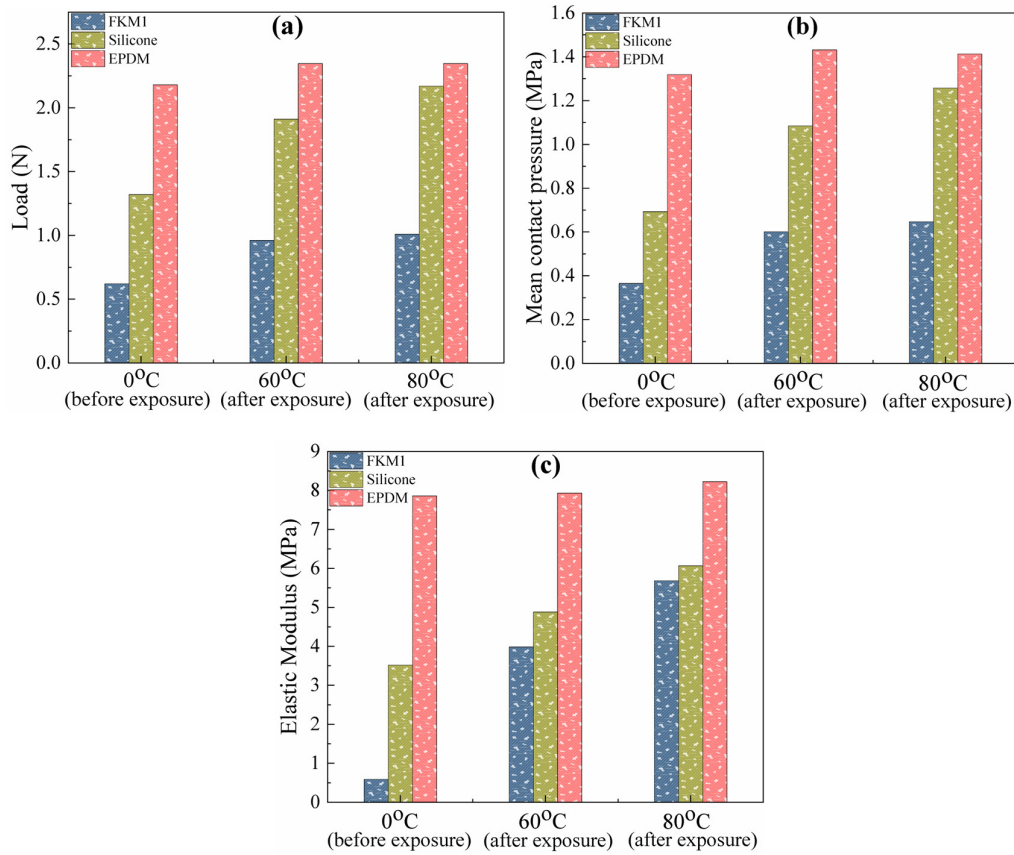


Figure 3.5 Bar charts showing (a) Indentation load (b) Mean contact pressure, and (c) Elastic moduli for FKM1, Silicone, and EPDM, respectively (i) before exposure, (ii) after 35-week exposure at 60°C, and (iii) after 35-week exposure at 80°C to a simulated fuel cell environment (ADT solution), adapted from (Tan et al. 2008e, 2011).

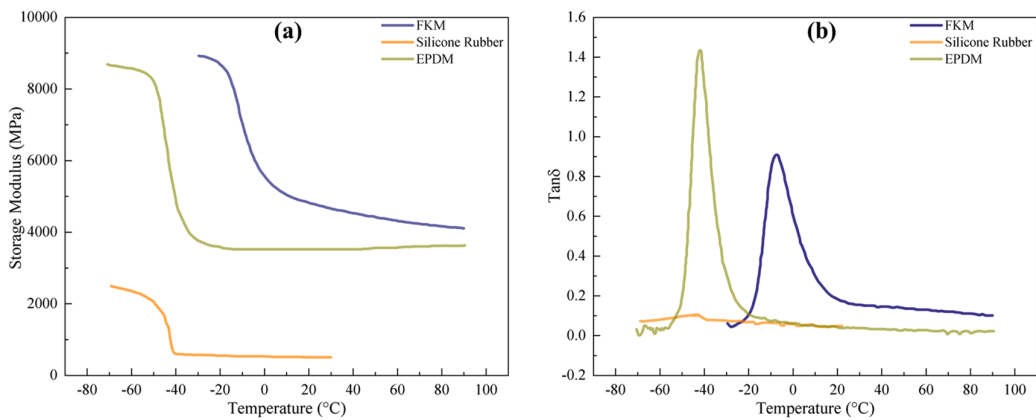


Figure 3.6 (a) Storage Modulus, and (b) Tan δ for FKM1, Silicone, and EPDM rubber samples, adapted from (Lin et al. 2011a; Tan et al. 2011).

3.2.1.6. Dynamic mechanical analysis (DMA)

The dynamic mechanical properties obtained for FKM1, Silicone, and EPDM rubber are shown in Figure 3.6. The results show (a) Storage modulus (E'), and (b) $\tan \delta$ with temperature for FKM1, Silicone, and EPDM rubber samples (Lin et al. 2011a). It is known that storage modulus (E') represents the ability of a material to store energy in the elastic region, whereas loss modulus (E'') represents the ability of a material to dissipate energy. In Figure 3.6(a), the higher E' indicates the higher stiffness and hence higher hardness. The E' value at room temperature (25°C) for FKM1 rubber (23.9×10^6 Pa) is the highest, followed by EPDM rubber (5.82×10^6 Pa). The stiffness or hardness of the Silicone rubber samples does not change significantly with temperature. These results indicate that FKM1 rubber is better choice as a sealant material than Silicone and EPDM rubbers in terms of hardness at high temperatures. Thus, FKM1 rubber is the appropriate sealant material in PEMFC working conditions, as it shows better hardness properties than Silicone and EPDM rubber.

3.2.1.7. Permeability

It is found that Silicone rubber is the most permeable elastomer than most other rubbers, as shown in Table 3.1. Silicone rubber is a suitable sealant material for extremely low-temperature applications, i.e., up to -100°C (Zhang and Cloud 2006). It is to be noted that Silicone rubber has adequate intermolecular forces and single bonds that are comparatively unbounded, joining the silicon and oxygen backbone chain atoms simultaneously. As a result, there is more free volume and greater chain mobility (Gillen et al. 2006a). The polarity of the suspended groups beside the siloxane chains affects the permeability of Silicone rubber. The solubility of gas influences it more than its diffusivity (Gillen et al. 2006b). The crosslink density in silicone rubber shows little effect on permeability. Filler levels reduce permeability in proportion to volume fraction (Burak Erman 2011; Nah et al. 2015). However, fillers also increase the specific density. The presence of fillers in silicone rubber increases the enthalpy of gas, implying that the polymer matrix's character is altered. It is also found that the gas diffusivity decreases with silica filler loading. From Table 3.1, it is evident that EPDM and FKM rubbers have significantly less gas permeability as compared to the Silicone

rubber. Therefore, FKM and EPDM rubbers are appropriate sealant materials in PEMFC working conditions.

Table 3.1 Permeability coefficient of the rubber materials according to ASTM D1418 (“Design guide” 2007).

Permeability coefficient								
Gases: (cm ³ -cm×10 ⁻⁸ /cm ² -s-atm), Fluids: (gm/m ² -day)								
Gas/Fluid	Ethylene acrylic (AEM) rubber	Isobutylene-Isoprene (IIR) rubber	Chloroprene rubber (CR)	EPDM	Epichlorohydrin rubber (ECO)	FKM	Silicone rubber	Nitrile butadiene rubber (NBR)
Air	0.3	0.6	1.1	7.9	0.105	0.099	-	2.5-7.5
CO₂	7	3.92-5.18	13.9-25.8	85	13.9-25.8	5	1028-1530	5.76-14.1
H₂	2.9	5.5	180	29-111	180	160	188-500	5.42-8.97
He₂	2.7	6.4	6-6.5	19.7	0.6-6.5	9-22	238-263	6.2
Nitrogen	0.3	0.24	0.01-2.0	6.4	0.66	0.5-0.7	75-210	0.18-0.50
Oxygen	1	0.99	1.1-4.0	16-18	0.255	1-2	195-605	0.73-6.5
Water	2.4	-	1.2	-	15.5	-	-	4.5

The above numbers are taken at standard temperature and pressure (STP) conditions

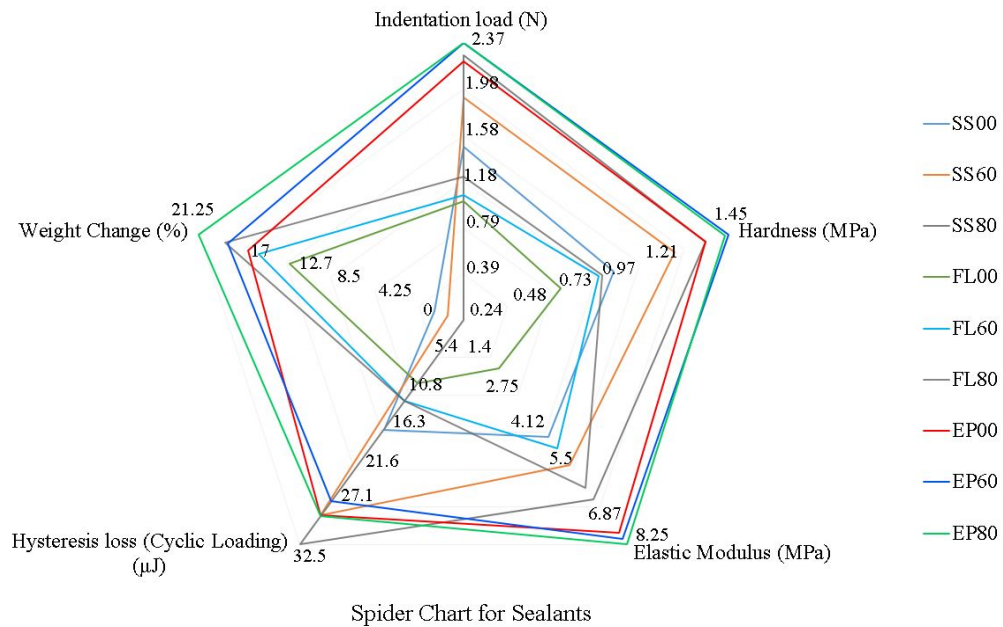


Figure 3.7 Showing the spider chart for the physical properties of sealant materials in PEMFCs, adapted from (Tan et al. 2008e, 2009a, 2011).

The physical characteristics of sealant materials such as FKM1, Silicone, and EPDM rubber are indicated using a spider chart shown in Figure 3.7. The weight change results suggest that the Silicone S rubber has a highest weight loss of 4.25% when subjected at 80°C to the regular solution. This indicates that the Silicone S rubber degrades more as compared to FKM1 and EPDM sealant materials. The FKM1 and EPDM sealant materials show highest weight gain of 18.75% and 21.25% respectively when subjected at 80°C to the regular solution. These results indicate that the FKM1 and EPDM sealant materials are better than Silicone S sealant material in PEMFC conditions. The indentation results show that the Silicone S and EPDM sealant material have high indentation load as compared to the FKM1 sealant material, as shown in Figure 3.7. These results also specify that the indentation load is in the range 2.2–2.4 N, i.e. it does not change considerably for the EPDM samples, as compared to FKM1 and Silicone rubber materials. Therefore, EPDM rubber show better results as compared to FKM1 and Silicone S sealant materials. The hardness results show that the EPDM rubber samples have hardness values in the range 1.3–1.45 MPa, which suggests that hardness did not change significantly with exposure time and temperature. Therefore, EPDM rubber is the better sealant material in terms of hardness in PEMFC conditions. From

Figure 3.7, Elastic modulus results for the EPDM rubber is found to be in the range 7.75–8.25 MPa. For FKM1 and Silicone rubber samples the Elastic modulus values change significantly, thus it is clear that EPDM rubber is a better choice for sealants, in terms of Elastic modulus. Similarly, the hysteresis loss results indicates that EPDM rubber has hysteresis loss in the range 25–27.6 μ J. These results suggest that EPDM rubber is the most stable sealant material as compared to FKM1 and Silicone sealant materials in PEMFC working environment.

3.2.2. Chemical properties of sealants in acidic environment

Due to the chemical reactions, elastomeric sealant materials often result in degradation. One of the reasons for elastomeric degradation is hydrolysis, which consists of the separation of vulnerable molecular groups (i.e., esters, amides, and carbonate groups) due to reaction with water, acids, and alkalis (Pehlivan-Davis 2015). Chain scission occurs whenever these groups are present in the backbone chain rather than the side chain. As a result, chain scission reduces the molecular weight of the polymer, causing the softening of polymer.

3.2.2.1. ATR-FTIR

The ATR-FTIR analysis governs the chemistry changes occurred to the FKM1, Silicone, and EPDM rubber sealants in a simulated PEFC environment. Figure 3.8 shows the FTIR results for the FKM, Silicone, and EPDM rubber samples in regular solution (Lin et al. 2011b; Tan et al. 2011). Here, FKM00 and FKM03 shows the plots for FKM1 rubber before subjecting it to the regular solution at 80°C, and after subjecting it for 3 weeks respectively. SS00, and SS08 shows the plots for Silicone rubber before subjecting it to the regular solution at 80°C, and after subjecting it for 8 weeks respectively. Similarly, EP00 and EP03 shows the plots for EPDM rubber before subjecting it to the regular solution at 80°C, and after subjecting it for 3 weeks respectively. The FKM1 material, which is unexposed to the regular solution, shows the intensity peaks at wavenumbers 2860 cm^{-1} and 2920 cm^{-1} . The peaks in the range 2850–3000 cm^{-1} are due to the CH₃, CH₂, and CH groups in FKM1 and EPDM rubbers. It also suggests that the intensities at the wavenumbers 2860 cm^{-1} and 2920 cm^{-1} for FKM1 samples decreased consistently in regular solution with exposure time. The

FTIR plots for the virgin EPDM rubber samples has the highest peaks at wavenumbers 2850cm^{-1} and 2920cm^{-1} . EPDM rubber is resistant to high temperatures (up to 120°C) and acidic environments by nature (Streitwieser and Heathcock 1976) due to its saturated hydrocarbon backbone. Despite the fact that EPDM rubber's primary chains are relatively stable, it can be degraded in an acidic environment (Mitra et al. 2006e; f; Tomer et al. 2007). In regular solution, the FTIR results for EPDM rubber show that the peak intensities almost disappeared after an exposure for 3-weeks to the regular solution. The strongest and broadest peak for the Silicone rubber samples is at 2962cm^{-1} , which is due to the stretching vibrations of $-\text{CH}_3$ present in the Silicone rubber backbone (Tan et al. 2011). These results suggest the chemical changes in the rubber backbone for the Silicone rubber samples exposed to the solution at 80°C and 60°C with exposure time. The FTIR results indicate that Silicone and EPDM rubbers are better choices for sealant materials as their degradation is less than the FKM1 rubber, in PEMFC working conditions.

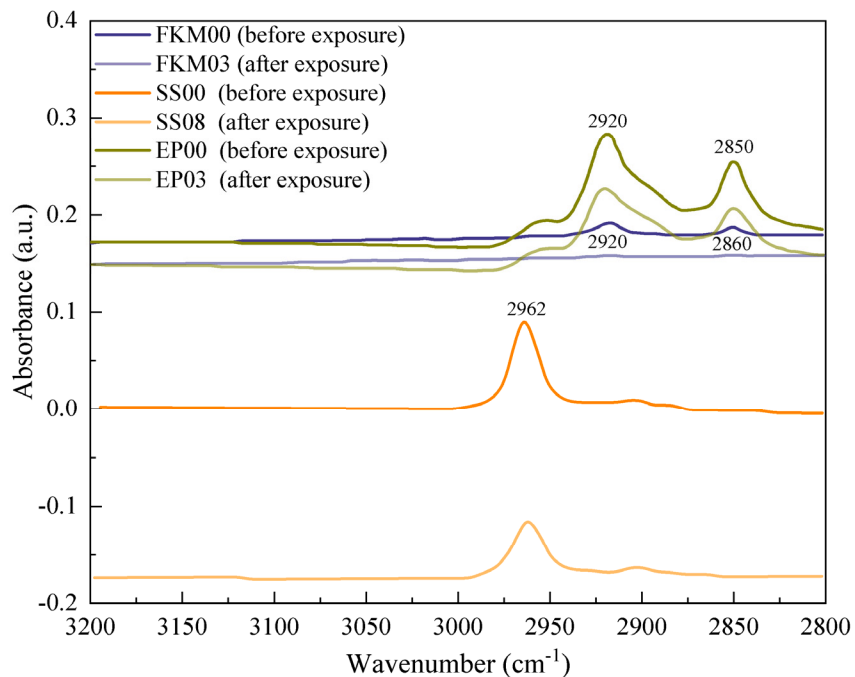


Figure 3.8 Structural change of FKM1, Silicone, and EPDM rubber samples before and after subjecting to the regular solution at 80°C by ATR-FTIR, adapted from (Lin et al. 2011b; Tan et al. 2011).

3.2.2.2. Atomic absorption spectroscopy

Figure 3.9(a) and 3.9(b) indicate the calcium and silicon concentrations for the FKM1 rubber samples exposed to the regular and ADT solution at 60°C and 80°C, and calcium and silicon concentrations for the Silicone and EPDM rubber samples exposed to the ADT solution at 60°C and 80°C (Lin et al. 2011c; Tan et al. 2009c, 2011). Figure 3.9(a) and 3.9(b), SS60 and SS80 indicate the silicone samples subjected to the solution at 60°C and 80°C, respectively. The calcium ions concentration for FKM1 samples in regular solution is much higher than that in ADT solution with exposure time. The calcium ions concentration for Silicone samples in ADT solution increases with exposure time and temperature, which is verified by the weight loss of Silicone samples as shown in Figure 3.2. The calcium ions concentration for EPDM samples in ADT solution does not change significantly, which can be verified with the weight change results as shown in Figure 3.2. The results show that, for Silicone rubber samples, the silicon ions have a substantially higher concentration than the calcium ions in ADT solution. The influence of temperature (60°C to 80°C) is also insignificant. The silicon ions concentration for Silicone rubber samples at temperatures 60°C and 80°C is higher than the FKM1 and EPDM rubber samples in ADT solution. For the FKM1 samples, the calcium ions concentration is higher in the regular solution, whereas the silicon ions concentration is the same in both regular and ADT solutions. Thus, the results indicate that the EPDM rubber samples are stable in both the regular and ADT solutions and do not degrade in terms of the calcium and silicon leachates. Therefore, EPDM rubber is a better choice as a sealant material as compared to the FKM1 and Silicone rubber in PEMFC operating conditions.

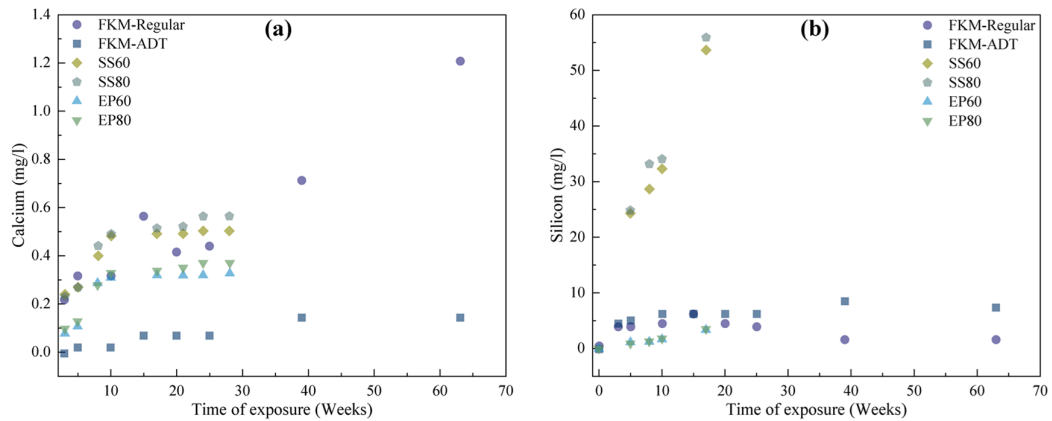


Figure 3.9 Plots showing the concentrations of (a) Calcium and (b) Silicon with time for FKM1, Silicone, and EPDM rubber, subjected to regular and ADT solution at 60°C, and 80°C respectively, adapted from (Lin et al. 2011c; Tan et al. 2009c, 2011).

3.2.2.3. X-ray photoelectron spectroscopy (XPS)

XPS is a surface investigation method to determine the elements present on the sealant material's surface. Before and after exposure to ADT solution at 80°C, XPS is utilized to gather qualitative and quantitative details of the surface of Silicone S and Silicone G materials. The XPS spectra indicate the existence of carbon (C), oxygen (O), silicon (Si) and small amount of fluorine (F) on the surface of samples. Table 3.2 shows the ratios of concentration (C/Si and O/Si) for Silicone S and Silicone G samples before and after different exposure times to the ADT solution (Tan et al. 2008d). As shown in Table 3.2, the C/Si ratio declined significantly with increasing exposure time. The surface chemistry changed as a result of chemical degradation, according to XPS analysis, and this is followed by de-crosslinking and chain scission in the backbone. The degradation of PEMFC sealant materials may eventually impact their mechanical and chemical durability.

Table 3.2 Atomic percentage of elements present on the surface of samples.

Sample	Exposure time	Atomic concentration, at. %				Ratio of elements to silicone		References
		C	O	Si	F	C/Si	O/Si	
Silicone S	Prior to exposure	51.36	27.56	20.41	0.67	2.52	1.35	(Tan et al. 2007b)
	1 week exposure	32.82	38.10	23.03	6.05	1.43	1.65	(Tan et al. 2007b)
	4 week exposure	23.13	51.81	25.06	0.00	0.92	2.07	(Tan et al. 2007b)
Silicone G	Prior to exposure	53.29	26.0	20.71	0.00	2.57	1.26	(Tan et al. 2008c)
	1 week exposure	48.69	29.22	21.51	0.58	2.26	1.36	(Tan et al. 2008c)
	4 week exposure	48.38	28.87	22.03	0.72	2.19	1.31	(Tan et al. 2008c)

As illustrated in Table 3.2, in the case of Silicone S, the O/Si ratio is found to increase with the exposure times. It suggests that the chain in silicone rubber backbone (Si-O-Si) is broken. Also, the C/Si ratio is lowered significantly with exposure time to the ADT solution. This behaviour could be related to the attack on the methyl group of silicon atoms and the formation of Si-O bonds. The results suggest that Silicone G rubber has more stability as it deteriorates less compared to Silicone S rubber samples in the same working conditions.

3.2.2.4. Irradiation (UV)

An Ultraviolet (UV) test is used to predict the expected service life of gaskets or sealants. In this test, the sealant materials are exposed to natural or artificial UV radiation. UV components in sunlight do not cause scission of the main chain and

siloxane (Si-O) rather C-H and Si-C bonds, in the case of Silicone rubber. Although the chances of main chain scission in Silicone rubber are low, crosslinking reactions can occur at the locations where Si-C and C-H bonds are broken. Many researchers have studied elastomeric materials exposed to environmental stresses such as heat, ultraviolet light (UV), moisture, and acid rain in order to replicate PEMFC operating conditions and anticipate the sealant materials' estimated service life (Hirano et al. 2001; Kumagai and Yoshimura 1999; Yoshimura et al. 1999; Zhao and Allen Bernstorff 1998). Their research has looked into the processes that cause the base polymer to degrade as well as the influence of the environment on the elastomeric material. In addition, to find out the relation between surface chemical state and electrical properties, additional investigations using material samples and controlled stresses utilising methods are carried out (Lee and Lee 1999; Moreno and Gorur 1999; Ollier-Duréault and Gosse 1998).

3.2.2.4.1. Weathering tester

Weathering includes the variables of temperature, precipitation, and variation in sunlight intensity. But, there should be more focus on solar radiation and, in particular, the UV region. A study by (Youn and Huh 2005) involved subjecting the samples to UV, using a weathering tester (Q-panel, QUV/spray) with eight UVB 313 nm fluorescent lamps. The wavelength range of the UV lamps is 280 nm to 415 nm. The distance between the lamps and the sample surface is found to be 50 mm. The UV radiation is subjected to only one of the samples. They performed the test cycle continuously with 4 hours of UV irradiation and 4 hours of condensation. The lamp's radiance at 313 nm wavelength and the temperature are kept within the chamber at $0.65 \text{ W/m}^2/\text{nm}$ and 50°C , respectively, during irradiation (Youn and Huh 2005). Also, they kept the temperature at 40°C during condensation with the UV turned off. They performed the test for a duration of 5000h.

3.3. Properties of sealants in alkaline environment

3.3.1. Physical properties of sealants in alkaline environment

3.3.1.1. Tensile strength and % Elongation

Tensile strength and % Elongation at break results for the FKM2 (Viton \hat{A}) material are plotted against time, subjected to NaOH (10%) solution as shown in Figure 3.10(a) and 3.10(b) respectively. The tensile strength and % Elongation both results show a decreasing trend with increasing exposure time to the medium. Also, the surface degradation due to the chemical attack affects the bulk properties of the material in due course.

3.3.1.2. Hardness

The surface hardness results for the FKM2 (Viton \hat{A}) rubber are found to be increasing with prolonged exposure time in NaOH (10%) solution at 80°C. The micro-hardness result is plotted in Figure 3.10(c), which suggests that the conversion of a less flexible rubber backbone into a slightly rigid backbone due to the presence of various functional groups of oxygen (due to the degradation) helps to increase the surface hardness of the sealant material. The micro-hardness of the samples has the units of International Rubber Hardness Degree (IRHD).

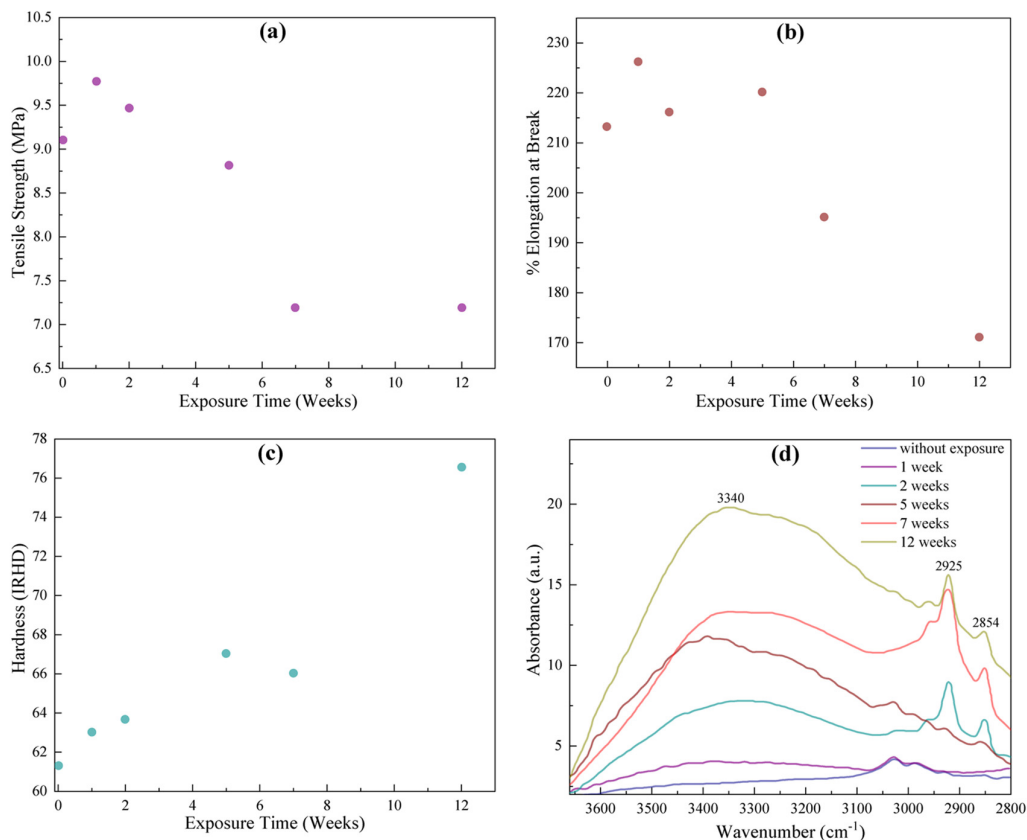


Figure 3.10 showing (a) Tensile strength, (b) % Elongation break, (c) Micro-hardness, and (d) ATR-FTIR plots for the sealant material FKM2 (Viton \hat{A}) subjected to NaOH (10%) at 80°C at different exposure times (1 to 12 weeks), adapted from (Mitra et al. 2004b; a).

3.3.2. Chemical properties of sealants in alkaline environment

3.3.2.1. ATR-FTIR

The ATR-FTIR curves for pure FKM2 (Viton \hat{A}) rubber before being subjected and after being subjected to the NaOH (10%) solution is shown in Figure 3.10(d) between 2700–3700 cm^{-1} . These plots indicate that remarkable changes occur in the FKM2 (Viton \hat{A}) rubber backbone when subjected for 1 week to the alkaline medium and subsequently minor changes occur when subjected for longer duration of time (i.e. up to 12 weeks) (Mitra et al. 2004b; a). These results are also in agreement with the XPS results as shown in Table 3.3.

3.3.2.2. XPS

The XPS results show significant changes in atomic ratios (C/F, O/F, and O/C). There is a conspicuous increase in C/F and O/F ratios with exposure time as shown in Table 3.3. This is more plausible because an alkaline environment-induced dehydrofluorination process removes hydrogen fluoride (HF) from the pure rubber backbone (Mitra et al. 2004b). The XPS result indicates that the chemical degradation of pure FKM2 (Viton \hat{A}) is not limited to the surface, but also approaches the bulk when subjected to the medium for an extended time period (Mitra et al. 2004a) (i.e. 12 weeks).

Table 3.3 XPS results show the atomic % ratios of C, F and O of the surface of FKM2 (Viton \hat{A}) rubber samples without being subjected and after being subjected to the NaOH (10%) solution at 80°C for different times (Mitra et al. 2004a).

	C/F	O/F	O/C
FKM2 (Viton \hat{A}) theoretical	0.63		
Pure FKM2 (Viton \hat{A})	0.74	0.02	0.03
0 week	1.24	0.18	0.15
1 week	4.70	2.11	0.45
2 weeks	4.40	3.10	0.70
5 weeks	3.28	2.61	0.79
7 weeks	4.38	4.38	1.00
12 weeks	3.39	3.55	1.05

3.4 Physical properties of silicone sealant material in acid and base medium under temperature cycling

The weight change results for the Methylvinyl Silicone rubber in four different environments including air are shown in Figure 3.11(a). The first solution is the regular solution as mentioned in the previous section. The second solution is the acetic acid solution having pH value of 5. The third solution is the de-ionized water having pH value of 7. The weight change for the Silicone sealant material is seen under

temperature cycling of -20°C to 90°C , which is the accumulated weight loss from the beginning (Wu et al. 2018b). The plots indicate that the degradation of Silicone material is more severe in these three solutions as compared to that in air. The weight loss for the samples is found to be more with an increase in the acidity of the medium. The presence of F- in the these acidic medium is the prominent cause for the degradation of the silicone material (Feng et al. 2014). Figure 3.11(b) shows the plots for Shore A hardness for Methylvinyl Silicone rubber, in these four environments as mentioned above. The results indicate that the Shore A hardness increased very slowly for the samples subjected to these environments as compared to air. The results also specify the increment in weight loss and reduction in Shore A hardness with the increase in the acidity of the medium, which signifies the effect of the working conditions of PEMFC on sealant materials.

Table 3.4 shows that the weight loss for the samples i.e degradation is more when they are subjected to these three solutions as compared to that in air. Also, the weight loss is found to increase with an increase in acidity of the solution.

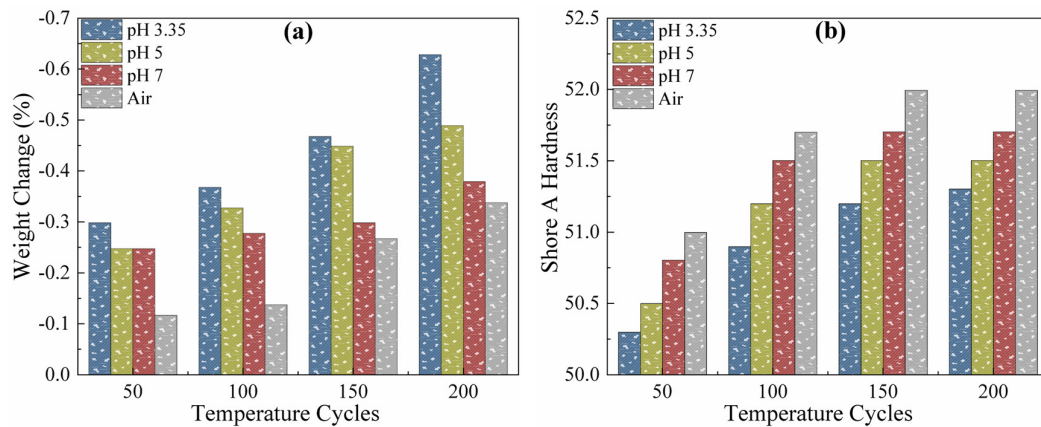


Figure 3.11 Effect of the acidic, alkaline and air medium on (a) Weight change, and (b) Shore A Hardness of Silicone rubber under temperature cycling from -20°C ~ 90°C , adapted from (Wu et al. 2018b).

Table 3.4 Percentage weight loss per cycle of the samples in acidic and basic environments subjected to temperature cycling (Wu et al. 2018b).

Temperature cycle	Testing Environments			
	pH 3.35	pH 5	pH 7	Air
50 th	0.0060	0.0050	0.0050	0.0024
100 th	0.0037	0.0033	0.0028	0.0014
150 th	0.0031	0.0030	0.0020	0.0018
200 th	0.0032	0.0025	0.0019	0.0017

3.5 Testing Standards

3.5.1 Sealant material properties

The sealant material's properties are studied before and after subjecting it to the exposure conditions. The exposure environments should have the pH values of 2 to 4 at temperatures of 60-80°C. The ASTM standards include tensile tests (ASTM D412, ASTM D638), hardness test (ASTM D2240), and compression set (ASTM D395) as shown in Table 3.5. Table 3.6 shows various ex-situ testing standards for the sealant samples in PEMFC working conditions. The results show that the samples have almost same tensile strength but 100% modulus results increase with exposure time. The results show that the % Elongation for the samples decreases with the exposure time. Also, the hardness and the % weight change for the samples increases with exposure time. These results indicate that the sealant samples are hardened when subjected to the hydrogen for longer duration.

Table 3.5 Test Methods for the samples (Parsons 2009).

Material Properties	ASTM Standards	No. of test specimens
Tensile strength	ASTM D412 (ASTM D638 Type IV Die)	Average of 5 test specimens/ test point
100% Modulus	ASTM D412 (ASTM D638 Type IV Die)	Average of 5 test specimens/ test point
% Elongation at break	ASTM D412 (ASTM D638 Type IV Die)	Average of 5 test specimens/ test point
Hardness Shore A	ASTM D2240	Average of 3 replicates per specimen/ 5 specimens
% Weight change	ASTM D471	Average of 5 specimens
% Volume change	ASTM D471	Average of 5 specimens
Density	ASTM D471	Average of 5 specimens

Table 3.6 Ex-situ durability test for PEFC sealants at 90°C in H₂ (At 15psi) (Parsons 2009).

Property	Method	0 hours	500 hours	2000 hours	6652 hours
		Average	Average	Average	Average
Tensile strength (MPa)	ASTM D412				
	(ASTM D638 Type IV Die)	1.4	1.3	1.4	1.3
100% Modulus (MPa)	ASTM D412				
	(ASTM D638 Type IV Die)	0.7	0.9	0.9	0.9
100% Elongation at break	ASTM D412				
	(ASTM D638 Type IV Die)	177	143	143	142
Hardness (Shore A)	ASTM D2240	36	38	38	38
% Weight change	ASTM D471	0%	0.38%	0.26%	0.62%
% Volume change	ASTM D471	0%	-1.09%	-0.11%	-0.43%
Density (gm/cc)	ASTM D471	0.963	0.978	0.967	0.974

3.6 Features of gaskets/sealants in PEMFCs

The sealants in PEMFC must possess the properties of electrical insulation as well as reactant gases mixing prevention. It must also have a high glass transition temperature (T_g), which is mainly important for HT-PEMFC. It should be chemically resistant to oxidant gases and mechanically resistant owing to stack compression. The sealant materials, such as FKM, Silicone, EPDM, LSR, and FSR rubber are found to be suitable for PEMFC working conditions (Lin et al. 2011b). Their chemical and mechanical deterioration have been given special attention. Silicone, EPDM, and PTFE rubber are

some of the most often utilized sealant materials for PEMFCs and have been shown to be adequate for gas tightness.

3.6.1 Tensile strength

The compression force is the property that ensures the proper contact of all components as well as leak proof working of PEMFCs. The compression tests include compression set and compression relaxation test, according to the ASTM standards (Shen et al. 2016a). The compression rate affects the contact pressure of sealant materials, including silicone rubber, butadiene acrylonitrile rubber (NBR), EPDM rubber, and PTFE (Qiu et al. 2020).

3.6.2 Chemical and high-temperature stability

It is crucial to investigate the thermal behavior of sealants. Thermo-gravimetric analysis (TGA) is the most common approach for assessing the thermal behavior of sealants. Also, T_g is an important physical property of elastomeric materials for determining the temperature associated with molecular motion. Rubber chain mobility decreases below T_g , and as the mobility of the rubber chains decreases, T_g increases (Xu et al. 2010). Also, chemical stability is an essential characteristic for the durability of the sealants in PEMFCs. The sealants are found to deteriorate with time, under compression, and in humid environments. Furthermore, it releases decomposition products into the MEA, poisoning the catalysts. The chemical deterioration of sealants can be evaluated directly in PEMFC or by placing the sealant samples in simulated PEMFC conditions and analysing them before and after being subjected to these conditions (Tan et al. 2009b). The dynamic mechanical analyzer (DMA) is accustomed to determining how the properties of sealant materials change with temperature (Tan et al. 2009b). Hardness is also an important factor, which affects the chemical decomposition of sealants. However, there is no evident relationship between the shore hardness number and the material's fundamental mechanical properties (Tan et al. 2008e). The effect of hardness on chemical deterioration can be examined in several ways, including soaking sealant materials in an acidic aqueous solution. The chemical stability of the sealant material is determined by measuring weight loss before and after subjecting it to certain

conditions of temperature, pressure, and relative humidity (RH) conditions in ref. (Lin et al. 2011b).

Table 3.7 illustrates the significant physical and chemical properties of sealants in PEMFCs. These results include mechanical strength, chemical stability, permeability and thermal stability of sealants. Table 3.8 shows the sealant materials, which are suitable for the LT-PEMFC and HT-PEMFC conditions. EPDM and FKM1 rubber materials can sustain high operating temperatures as well, thus they are suitable for both LT-PEMFC and HT-PEMFC operating conditions.

Table 3.7 Important physical and chemical properties of gasket/sealant materials in PEMFCs.

Working	Characteristics	Property	Measurement			
			Procedure	Apparatus	Existing or under development	Destructive or non-destructive
Mechanical strength	Hardness	Shore hardness (Shore A)	Shore hardness test (Cylindrical samples)	Shore hardness durometer (Wu et al. 2018a; Xu et al. 2010) (ASTM D2270)	E	D
		Indentation hardness (kgf mm ⁻²)	Micro-indentation hardness test	Load-depth sensing micro-indenter(Tan et al. 2008e, 2009b)	E	D
	Tensile strength	Elongation at break (%)	Mechanical tests	Universal mechanical tester(Xu et al. 2010)	E	D
		Tearing strength (Nm ⁻¹)				
	Young's Modulus (Pa)					

	Compression properties	Compressibility	Compression stress relaxation test (Cylindrical samples)		CMT-4104 testing machine (ASTM D6147) (Shen et al. 2016a)	E	D
		Compression set (Xia et al. 2016)	Compression set test (Cylindrical samples) (Grelle et al. 2015)		ASTM D395 (Method B)(Shen et al. 2016a)	E	D
			Measuring the compression set over a long period (e.g., 10000 h) (Grelle et al. 2015; Xia et al. 2016)		ASTM D395	E	D
	Tribological Properties	Friction coefficient	Mechanical tests		Tribometer	E	D
Chemical stability	Chemical stability	Chemical aging stability (short term and long term)	Chemical ageing test	Fenton's test	Fenton's reagent (3% H ₂ O ₂ containing 2 ppm FeSO ₄)	E	D
				Various simulated solutions containing H ₂ SO ₄ and HF		A regular solution contains 12.5ppm H ₂ SO ₄ , 1.8ppm HF with a pH of about 3.4 (Li et al. 2012)	

Chemical aging test under compression	Aging test under compression	In an accelerated durability solution, a gasket sample is sandwiched between two graphite plates and subjected to various temperatures and compressive loads(Lin et al. 2011b; Shen et al. 2016a)	E	D
Characterization	Weight loss monitoring	Microbalance(Lin et al. 2011b)	E	D
	DMA(Grelle et al. 2015)	Rheometrics Solid Analyser RSA-III (TA Instruments)(Tan et al. 2009b); DMA analyser (Xu et al. 2010)	E	D

Electrical insulation and Prevention of gas mixing	Gas permeation			Morphology inspection	Optical microscope(Xia et al. 2016), SEM	UD	D
		Visual inspection	Visual inspection for completeness or potential defects, e.g., bubbles	Analytical methods	AFM, XPS, FTIR-ATR, atomic absorption spectrometry (Li et al. 2012; Lin et al. 2011b; Tan et al. 2007a, 2009b)		
					No tools needed (Microscope or camera)	E	N
		Thickness (µm)	Thickness measurement		Micrometer	E	N or D
		Gas permeability (s/100 cc gas)	Flow under pressure difference (through plane)		Pressure differential gas permeation cell (Shen et al. 2016b)	E	D

Thermal tolerance	Thermal stability	Glass transition temperature (T _g)	Dynamic thermo-mechanical analysis	TGA; TGA-FTIR, XPS(Liu et al. 2013); DSC(Grelle et al. 2015)	E	D
		Tolerance of temperature	Weight loss monitoring	Microbalance (Wu et al. 2018b); TGA	E	D
			Alternating temperature cycling test	Simulated fuel cell testing environment (Wu et al. 2018b)	E	D

Table 3.8 Gasket/Sealant materials suitable for LT-PEMFC and HT-PEMFC, depending on the working temperature of the sealants.

S.No.	Sealant Materials	PEMFCs	References
1.	Silicone	LT-PEMFC	(Chang et al. 2016; Haider et al. 2021; Pehlivan-Davis 2015)
2.	EPDM	LT-PEMFC and HT-PEMFC	(Haider et al. 2021; Pehlivan-Davis 2015)
3.	FKM1	LT-PEMFC and HT-PEMFC	(Haider et al. 2021; Lin et al. 2011b; Pehlivan-Davis 2015)
4.	FKM2 (Viton Â)	HT-PEMFC	(Mitra et al. 2004a)
5.	PTFE	HT-PEMFC	(Haider et al. 2021; Pehlivan-Davis 2015)

3.8 Closure

The physical and chemical characteristics of sealants are vital in ascertaining the overall performance and longevity of the PEMFC, as reported in this chapter. In the following chapter, the thermomechanical response of the commercial sealant PTFE is experimentally investigated in the temperature range of 25–65°C, at stresses of 2, 3, and 4 MPa.

CHAPTER 4

THERMOMECHANICAL RESPONSE OF COMMERCIAL SEALANT MATERIALS USED IN PEM FUEL CELLS

4.1 Introduction

PTFE has the inbuilt viscoelasticity characteristic, indicating that its mechanical characteristics vary with time and temperature. Creep and stress relaxation are two important time-varying deformation characteristics of viscoelastic materials that are caused by constant loading at high-temperature conditions. The methodology for studying the temperature dependency of viscoelastic behavior through creep experiments is to develop a master curve at a reference temperature (utilizing the TTS approach), to predict the long-term creep compliance results for PTFE sealant at higher temperatures. The impact of stress and temperature on the creep characteristics of PTFE sealants are explored in this study.

The detailed creep response of PTFE sealants is reported by incorporating TTS principle and WLF equation and, thereby, developing master curve for creep compliance. The creep compliance master curve thus obtained forecasts the long-term behaviour of PTFE sealants, which is not easily accessible under the test conditions. It is evident from the literature that such detailed creep analysis is not available for PTFE sealants in PEMFCs. The viscoelastic creep compliance model developed in the study would be helpful for its potential high-temperature applications, such as in HT-PEMFCs.

4.2 Material

The polymer material explored for the creep characteristics in this study is PTFE. Rectangular samples, having dimensions of 70.5×22.4×0.53 mm are tested on Electroforce-3310, TA Instruments. The sample dimensions considered in the present study are within the machine's permissible dimensional limit (Electroforce-3310, TA-Instruments). Also, the gauge length (span length) of the samples in the current study

is in the range of 20–22 mm. Moreover, the sample dimensions considered in the present study are quite close to that in the ref. (Mahdavi et al. 2018) During the complete test, creep strain is observed with loading time. The PTFE samples are heated to the test temperature and soaked at every temperature for a duration of 5 minutes so that the temperature is stabilized and then the test is started. The tensile test fixture is enclosed by a heating chamber attached to the machine Electroforce-3310 (TA Instruments).

4.3 Experimental Procedure

Creep tests are conducted on Electroforce-3310 (TA Instruments), which has a servomotor fixed at the top to provide the linear displacement to the upper movable fixture. The maximum permissible load which can be applied to the samples in this machine, is 1000N. The creep specimens are subjected to three different stress levels of 2, 3, and 4MPa. The specimens are subjected to temperatures of 25, 35, 45, 55, and 65°C for each of these stress levels. Before conducting each high-temperature test, the fixture containing the sample is kept at the desired temperature for five minutes. This is done to ensure that the equilibrium condition is maintained. Creep test on PTFE samples is conducted in four consecutive steps. In the first step, the desired stress (2, 3, and 4MPa) is achieved in 60 seconds by gradually increasing the load from zero, followed by the second step in which a constant stress is applied for 3600 seconds. In the third step, load is reduced to 5N in 60 seconds, and then in the fourth step, the load is kept constant at 5N for 120 seconds. The creep strain plots are shown in Figure 4.1, where time is taken in minutes.

4.4 Results and Discussion

4.4.1 Creep Test Results

It is essential to determine the range (linear and non-linear) of viscoelastic characteristics while conducting a tensile creep test. These ranges are generally determined by conducting a tensile test for the samples. Detailed investigation is conducted on the creep characteristics of PTFE utilizing the TTS principle. Figure 4.1(a-c) illustrates the isothermal creep curves for temperatures 25–65°C and at three different stress magnitudes of 2, 3, and 4 MPa, respectively. These plots show the creep plots as a function of time for PTFE. Generally, creep behavior includes three phases

i.e. elastic deformation, primary and secondary creep as shown in Figure 4.1(a-c). It is anticipated that the creep response of the samples rises with increasing temperature, indicating the high-temperature softening of the polymer matrix due to the reduction of stiffness of the polymer chains. When the temperature is raised from 25 to 65°C, the creep strain of the PTFE sample increases by ~482% (from ~0.006497 to ~0.0378 at 2 MPa, ~330% (from ~0.011197 to ~0.048174 at 3 MPa), and ~608% (from ~0.015307 to ~0.108302 at 4 MPa) at 1800 sec. Therefore, the creep deformation is very sensitive to the temperature to which the sample is subjected. The creep compliance is further developed within the linear viscoelastic domain of 2 MPa for temperatures in the 25–65°C range by considering a reference temperature of 25°C, which is addressed in the next chapter. The creep behavior over the range of 2–4 MPa is adequately identical at almost all temperatures. It is evident from the creep strain plots at stresses of 2, 3, and 4 MPa that the slopes of these curves (strain rate) increase with temperature. Moreover, their slopes are again increasing with an increase in stress levels. This is particularly evident when the temperatures are higher than 45°C. These results are fairly consistent with the results reported in the ref. (Shojaei et al. 2018).

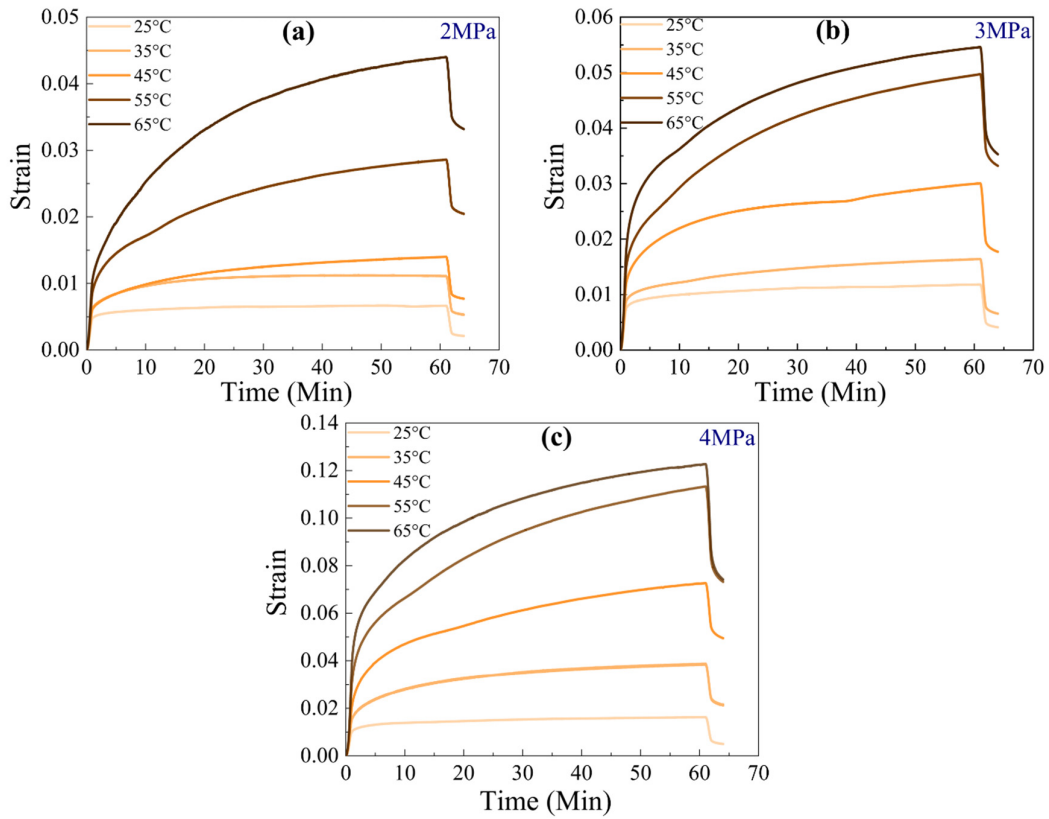


Figure 4.1 Creep strain plots at temperatures 25–65°C, at stress magnitudes of (a) 2 MPa, (b) 3 MPa, and (c) 4 MPa.

4.5 Closure

The present chapter includes the study of the creep strain vs time plots for PTFE sealants in PEMFC operating conditions. The following chapter incorporates the analytical study to develop the master curves for PTFE sealant at three stress levels of 2, 3, and 4MPa by utilizing the TTS approach with the WLF equation.

CHAPTER 5

NUMERICAL INVESTIGATION ON THE CREEP RESPONSE OF SEALANTS UNDER PEM FUEL CELL ASSEMBLY LOADING

5.1 Experimental creep characteristics of PTFE sealant

Figure 5.1 depicts the experimental setup for conducting the creep test on Electroforce-3310 (TA Instruments) with an environmental chamber along with the loaded PTFE sample on the tensile test fixture, and the PTFE test sample.

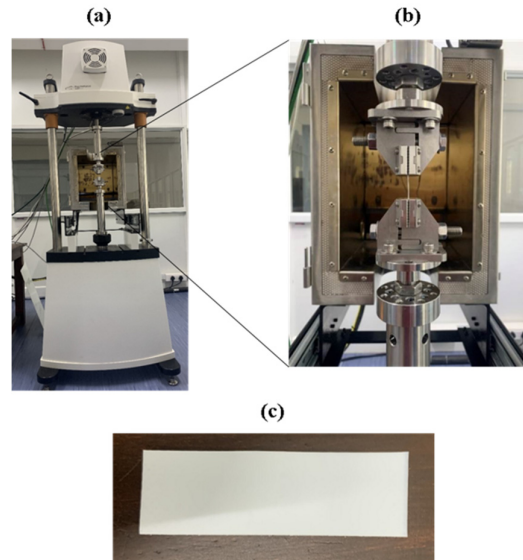


Figure 5.1: Shows (a) the experimental setup of the creep test on Electroforce-3310 (TA Instruments) with environmental chamber, (b) enlarged view of the loaded PTFE sample on the tensile test fixture, and (c) PTFE test sample.

5.2 Time-temperature superposition (TTS)

To evaluate the creep compliance for extended time-period, TTS principle is applied to short-term creep test data and the master curve for creep compliance-time is obtained. Figure 5.2 depicts the compliance-time plots for PTFE samples at 2, 3, and 4 MPa, by considering the reference temperature at 25°C. The master curves provide creep-

compliance for a longer period, which is not being done experimentally. PTFE samples are found to exhibit a linear viscoelastic nature up to 2 MPa. Therefore, TTS can be conducted on the creep plots produced at different temperatures at stress of 2 MPa. The TTS approach involves moving the plots shown in Figure 4.1(a-c) in the previous chapter horizontally towards the reference temperature $T_0=25^\circ\text{C}$, in order to produce master curves as shown in Figure 5.2. The master curve at 2 MPa, as shown in Figure 5.2, is able to provide creep compliance predictions for 4.5 hours at room temperature. Figure 5.2(a-c) shows that the six-term Prony series fits the experimental creep data well. The Prony series parameters are evaluated by the curve fitting process at the stress levels of 2, 3, and 4 MPa, and are mentioned in Table 5.1. The time-constants τ_i are set to 10^i seconds at the beginning of the curve-fitting process so that the approach would be simpler to understand.

5.3 Mathematical model for studying the creep behavior of PTFE sealants

The mathematical model for the creep predictions utilizing the stress and temperature-dependent non-linear parameters is given by Eqn (5.9). It is well known that the TTS approach to construct the master curves applies only in the viscoelastic region. Therefore, accurate creep predictions can be obtained by utilizing the TTS approach in the linear viscoelastic domain. The occurrence of viscoplastic strains in PTFE samples at higher temperatures and higher stress magnitudes is the prospective reason for the deviations of the experimental curves from the predicted curves as shown in Figure 5.8(a-c). In addition, previous studies have verified that choosing reference temperatures close to the T_g results in more accurate model predictions. (Dasappa 2008)

The time-varying response of polymer materials is described as linear viscoelastic:

- (a) If the compliance-time plots that are produced at different stresses are identical to one another.
- (b) In the event that the Boltzmann superposition principle holds true. According to the Boltzmann principle, every loading operation contributes to the overall deformation. As a result, the overall deformation can be understood as the aggregate of the contributions made by each loading operation.

If any of the two above conditions is not fulfilled, then the material in consideration is defined as non-linear viscoelastic. In a certain range, a material may have linear viscoelastic characteristics; but, if the temperature, stress, or time crosses a particular limit, the material behaves as non-linear. The Schapery viscoelastic model (Gamby and Blugeon 1987) is utilized while attempting to model the properties of polymers. It can be written as,

$$\varepsilon(t) = g_0 D_0 \sigma + \int_0^t g_1 \Delta D (\phi - \phi') \frac{\partial (g_2 \sigma)}{\partial \tau} d\tau \quad (5.1)$$

Where, $\varepsilon(t)$ is the creep strain, σ is the stress, D_0 and ΔD are the instantaneous and transient compliance in the linear viscoelastic domain. ϕ and ϕ' are the reduced time, g_0 , g_1 , g_2 , and a are the stress dependent non-linear variables. Considering the values of g_0 , g_1 , g_2 and a to be 1, Eqn (5.1) is reduced to linear viscoelastic. The transient compliance ΔD is presented as Prony series, which is specified as,

$$\Delta D(t) = D_0 + \sum_{i=1}^N D_i (1 - e^{-t/\tau_i}) \quad (5.2)$$

The Schapery viscoelastic model can increase its applicability range by applying numerous modifications. One approach to illustrate the impact of temperature on creep is to interpret each non-linear characteristic as a function of temperature and stress. Furthermore, it can be stated as a product of the functions of temperature and stress, despite being two distinct functions (Peretz and Weitsman 1983) i.e.

$$\mu(\sigma, T) = \mu_\sigma \cdot \mu_T \quad (5.3)$$

$$g_i(\sigma, T) = g_{\sigma_i} \cdot g_{T_i}, \text{ with } i=0, 1, 2 \quad (5.4)$$

The temperature-dependent parameters μ_T and g_{T_i} are calculated at a reference stress level. In contrast, the stress-dependent parameters μ_σ and g_{σ_i} are calculated from the data at a reference temperature. In Eqn (5.3), μ_T is the shifting factor derived using TTS. (Dasappa et al. 2009b; c; Gamby and Blugeon 1987; Peretz and Weitsman 1983; Shaw and MacKnight 2005; Xiao et al. 1994)

According to the TTS principle, viscoelastic material exhibits a relation in the linear range where its characteristics at higher temperatures are comparable to those at lower temperatures for a longer period. Therefore, the results from the short-term creep test conducted at high temperatures can be utilized along with an accelerated test method to forecast the long-term creep behavior of polymers. The creep compliance can be related at the temperatures, T_1 and T_2 , utilizing the following equation,

$$D(t, T_1) = D\left(\frac{t}{\mu_T}, T_2\right) \quad (5.5)$$

Where, μ_T is the shifting factor, which follows the WLF (Williams-Landel-Ferry) equation given as,

$$\log(\mu_T) = -\frac{c_1(T-T_0)}{c_2 + (T-T_0)} \quad (5.6)$$

Where, c_1 and c_2 are constants. The isothermal creep curves are shifted horizontally in order to determine the shift factor. This process continues until all creep plots meet with the creep plot at reference temperature (T_0).

Based on the application of PTFE as sealants in PEMFC, they are usually exposed to a wide range of temperatures starting at room temperature (RT) up to 80°C. Therefore, the characteristics investigations of the sealants in this particular temperature range is very crucial. It is clearly seen from the creep compliance curves that with an increase in temperature, the creep compliance increases. The prediction of creep behavior at elevated temperatures (accelerated creep) in a shorter time interval is achieved by developing a creep compliance master curve, considering a reference temperature, and utilizing the time-temperature superposition (TTS) technique. The master curve thus obtained mimics the creep compliance results at the reference temperature for an extended period. The master curve thus developed provides creep compliance prediction for 4.5 hours, at stress magnitudes of 2, 3, and 4 MPa as shown in Figure 5.2. It is noticed that creep compliance increases at higher temperatures especially at higher stresses. Significant rise in the slope of creep strain curves and the creep compliance at higher temperatures at all stresses (2, 3, and 4 MPa) as shown in Figure 4.1 and Figure 5.3, respectively, can be attributed to the movement of polymer chains,

as reported in refs. (Mahdavi et al. 2018; Shojaei et al. 2018). Moreover, the creep characteristic of PTFE is reflected in the current study, as the creep compliance master curves at temperatures above 45°C have steeper slopes than those at lower temperatures. These results are also fairly consistent with that in the ref. (Shojaei et al. 2018). Figure 5.3 shows the creep compliance master curves and their respective curve fits at stress magnitudes of 2, 3, and 4 MPa. These compliance master curves fit well with the six-term Prony series, as the R^2 value is 0.987, 0.991, and 0.994 for 2, 3, and 4 MPa, respectively.

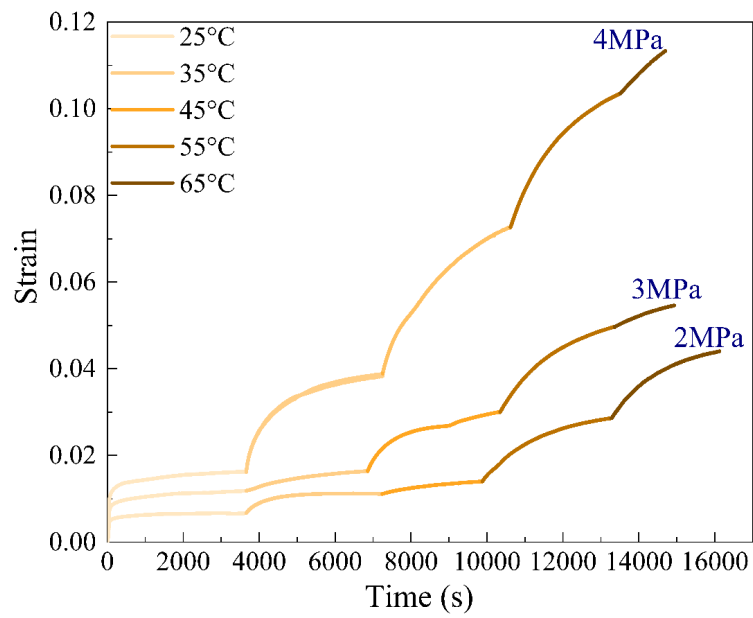


Figure 5.2 Creep compliance master curves obtained on log-time scale, at 2, 3, and 4 MPa at reference temperature, $T_0=25^\circ\text{C}$.

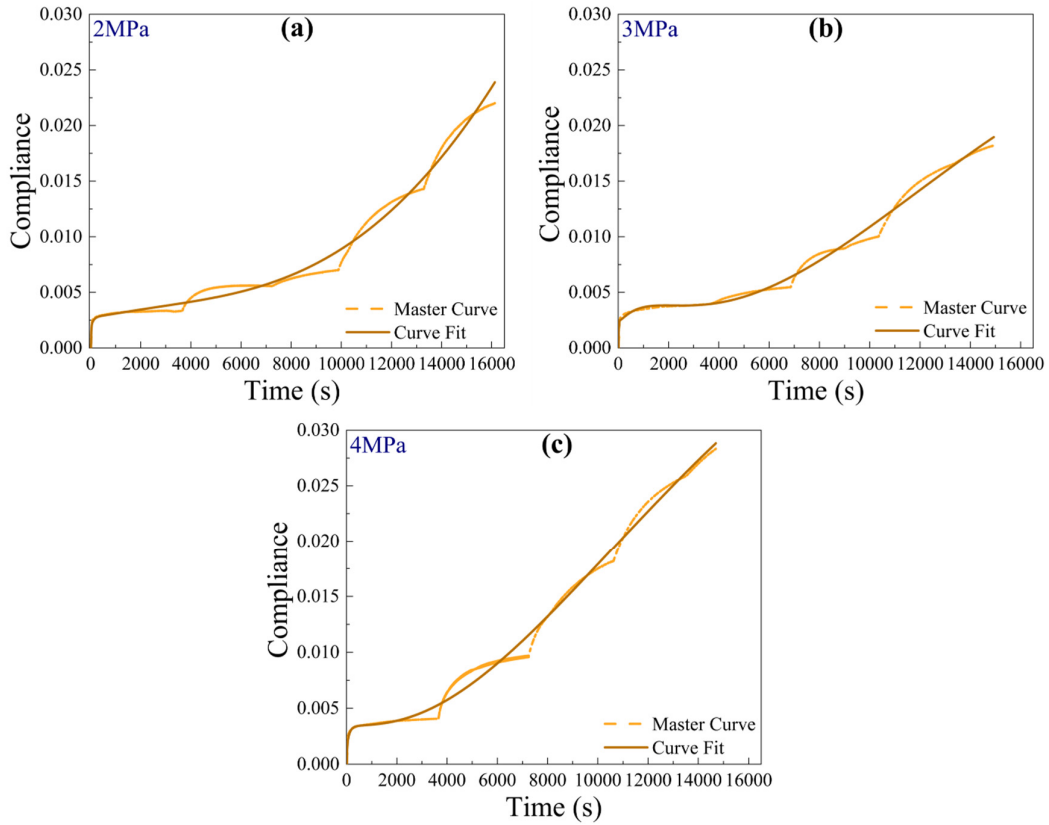


Figure 5.3 Shows the master curve obtained at (a) 2 MPa, (b) 3 MPa, and (c) 4 MPa and their respective curve fits to six-term Prony series.

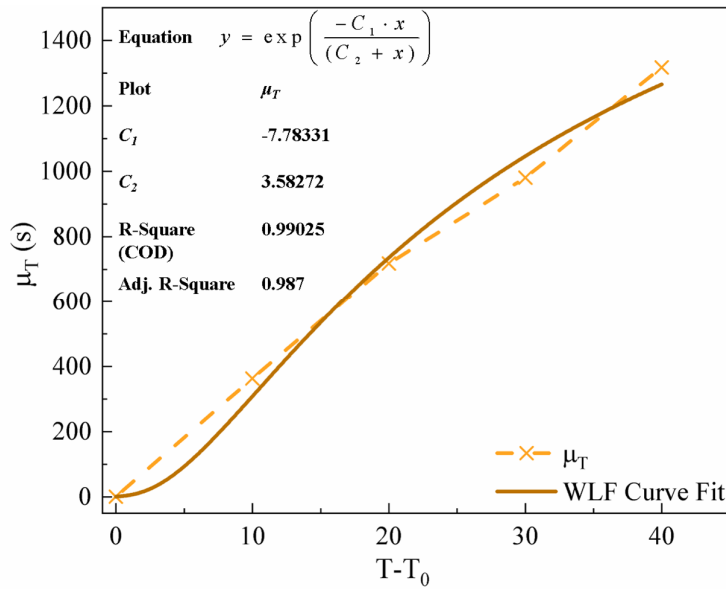


Figure 5.4 Shows the shift factors fitted with WLF equation, at a reference temperature, $T_0=25^\circ\text{C}$

A curve-fitting procedure is conducted on the shift factors which are obtained by shifting the isothermal creep curves horizontally towards the reference temperature, $T_0=25^\circ\text{C}$, using the WLF Eqn (5.6). The shift factor μ_T is plotted and with $T-T_0$, the results may be seen in Figure 5.4. The R^2 value of 0.987 is achieved, demonstrating that the curve fits well. However, when contrasted with the experimental result, the WLF equation appears quite linear. The WLF equation after the curve fit can be written as:

$$\log(\mu_T) = \frac{-7.78331(T-T_0)}{3.58272+(T-T_0)} \quad (5.7)$$

Figure 5.5(a) shows the creep compliance with stress at temperatures from 25 to 65°C . The compliance responds to increasing stress at lower temperatures linearly; however, at higher temperatures, it exhibits a non-linear behavior. Figure 5.5(b) depicts the plots of compliance with temperature at the stresses 2, 3, and 4 MPa. It is evident that the slope of the compliance curve with temperature at 4 MPa is steeper than that of other stress levels. This indisputably suggests a sudden rise in the PTFE material's temperature sensitivity. Therefore, PTFE material can be considered as non-linear viscoelastic above the stress of 2 MPa. In addition, PTFE material can be considered to be non-linear at temperatures above 45°C (including 45°C), as the slope of the compliance-stress curves becomes steeper at these temperatures.

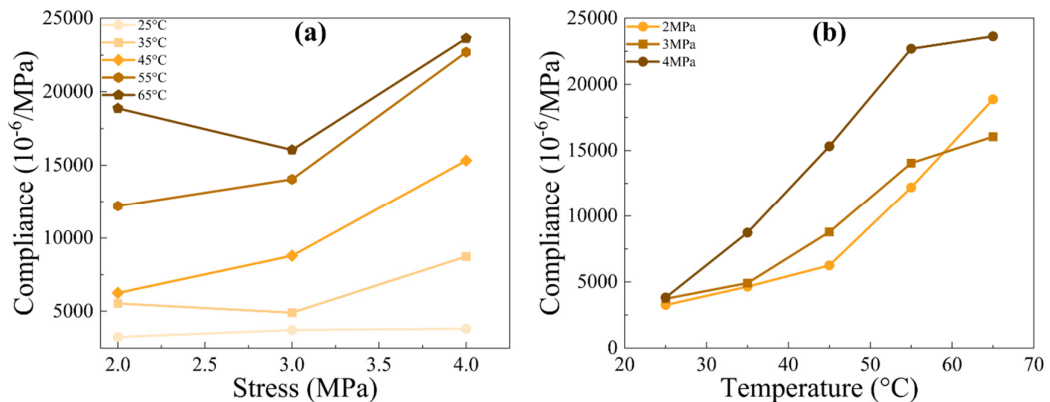


Figure 5.5 (a) Variation of creep compliance with stress at temperatures of 25- 65°C and (b) Variation of creep compliance with temperature at stresses of 2 to 4 MPa.

Table 5.1 Prony series parameters for stress values of 2, 3, and 4 MPa

Equation	$\Delta D(t) = D_0 + \sum_{i=1}^6 D_i(1 - e^{-t/\tau_i})$		
Time constants, τ_i (s)	10^i		
Stress	2 MPa	3 MPa	4 MPa
Coefficients (MPa ⁻¹)			
D_0	-0.00594	-0.00797	-0.00529
D_1	0.00771	0.01038	0.00666
D_2	0.000986727	-2.49445E-04	0.00198
D_3	-0.000452707	0.00503	0.00123
D_4	0.09303	-0.12145	-0.12685
D_5	-7.64626	4.57683	5.32183
D_6	67.88006	-35.68597	-41.50032

5.4 Non-linear viscoelastic formulations

Under a stress σ_0 , Eqn. (4.1) is rewritten as,

$$\varepsilon(t) = \left(g_0 D_0 + g_1 g_2 \Delta D \left(\frac{t}{a} \right) \right) \sigma_0 \quad (5.8)$$

It was discovered that the instantaneous loading and the unloading reactions are the same, hence $g_i=1$. In addition, because of the uneven distribution of the data, it is

presumed that, $a_\sigma=1$. When the Prony series are substituted into Eqn. 4.1 and the values $g_l=1$ and $a=\mu T$ are used, the creep strains can be stated as

$$\varepsilon(t) = \left(g_{\sigma_0} g_{T_0} D_0 + g_{\sigma_2} g_{T_2} \sum_{i=1}^N D_i \left(1 - e^{-t/(\mu T \tau_i)} \right) \right) \sigma_0 \quad (5.9)$$

5.4.1 Ascertainment of g_{σ_0} and g_{σ_2}

The plots of the nonlinear parameters g_{σ_0} and g_{σ_2} are demonstrated in Figure 5.6(a) and 5.6(b), respectively. It is discovered that g_{σ_0} varies in a quadratic manner with stress, and hence a quadratic function is fitted to the data given in Eqn (5.4). The non-linear variable g_{σ_2} can be presented in the form of quadratic expression of stress at 2 MPa as illustrated in Figure 5.6(b) and Eqn (5.11). It is to be noticed from Figure 5.6(b) that the non-linear variable g_{σ_2} may be considered as a quadratic function of stress at the stress of 2 MPa, and above 2 MPa, also it increases quadratically up to the stress of 4 MPa, as shown in Eqn (5.11).

$$g_{\sigma_0} = 0.8266 + 0.3614\sigma - 0.0472\sigma^2 \quad (5.10)$$

$$g_{\sigma_2} = 1.03234 - 0.1644\sigma + 0.04808\sigma^2 \quad (5.11)$$

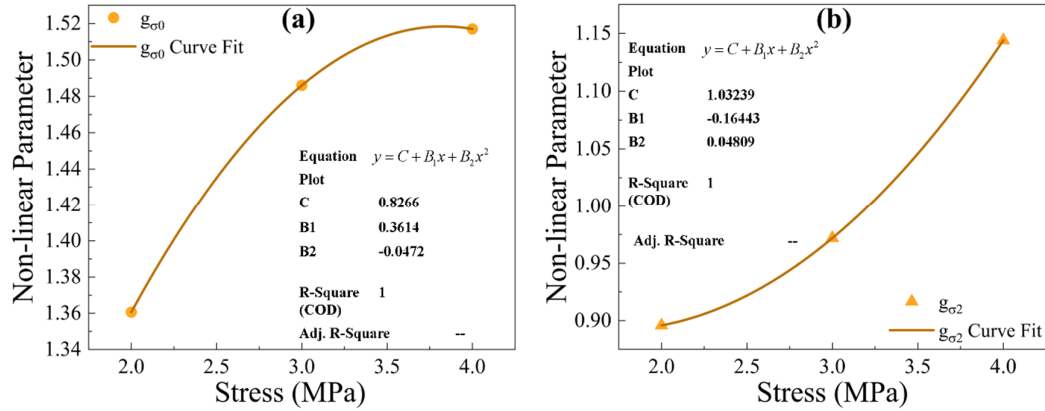


Figure 5.6 The relationship of the non-linear variables (a) g_{σ_0} and (b) g_{σ_2} with stress and their respective curve fits.

5.4.2 Determination of g_{T_0} and g_{T_2}

The non-linear parameters g_{T_0} and g_{T_2} are discovered to be very close to equal to one at the stress level of 2 MPa. This indicates that the impact of temperature is insignificant. It is considered that $g_{T_0} = 1$ and $g_{T_2} = 1$ at 2 MPa, to simplify the model. It means that the influence of temperature at 2 MPa can be successfully modelled with the assistance of shift factors acquired from TTS at 2 MPa. Eqn. (5.12) and Eqn. (5.13) show that the parameters g_{T_0} and g_{T_2} are quadratic up to 4 MPa as shown in Figure 5.7(a) and 5.7(b). This provides the insight that at stress of 2 MPa and above, the temperature-dependent parameters g_{T_0} and g_{T_2} both show non-linearity in instantaneous response with temperature and their slope increases up to 65°C, indicating that there is sharp increase in viscoelastic properties of PTFE samples at higher temperatures and stresses.

$$g_{T_0} = 0.9338 - 0.08425T + 0.00305T^2 \quad (5.12)$$

$$g_{T_2} = 1.13928 - 0.08365T + 0.00294T^2 \quad (5.13)$$

The parameters g_{T_0} and g_{T_2} , and their respective curve fits at 2 MPa are shown in Figure 5.7(a) and 5.7(b), respectively.

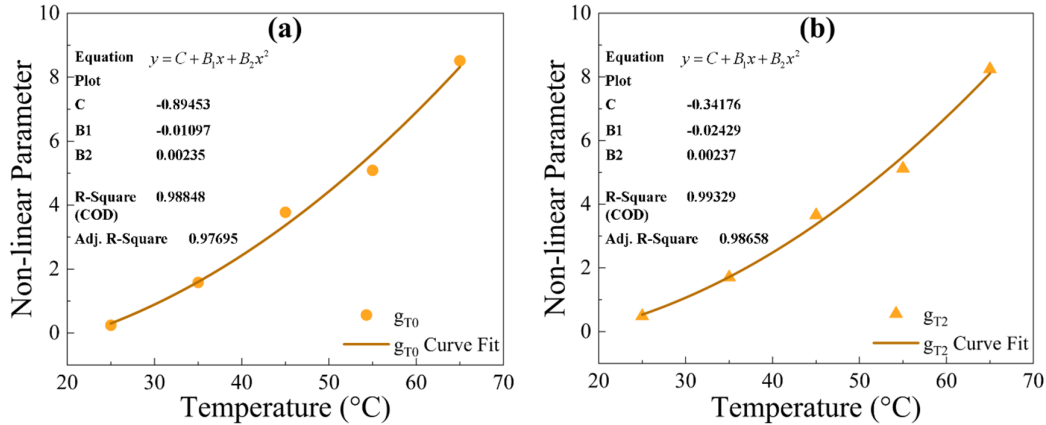


Figure 5.7 The non-linear variables (a) g_{T_0} and (b) g_{T_2} as an expression of temperature, and their respective curve fits.

5.5 Model forecasts

The model provides forecasts using non-linear variables, shown in Eqns (5.10-5.13). The shifting factors obtained from the WLF Eqn (5.6) are equated with the experimental plots presented in Figure 5.8(a-c). The predicted and experimental curves are represented as Pr. and Exp. correspondingly, as demonstrated in Figure 5.8(a-c). It is observed from Figure 5.8(a) that the predictions at 2 MPa fits the experimental data quite well at all temperatures. Figure 5.8(b) indicates that, at the stress of 3 MPa, the predictions are quite comparable to the experimental curve up to the temperature of 55°C, but at the temperature of 65°C, the predicted curve deviates from the experimental curve. Figure 5.8(c) shows that the predicted creep curves at 4 MPa are quite off the experimental curves at temperatures over 35°C. Although the predicted plots deviate from the experimental plots at higher temperatures, particularly at higher stresses, the forms of anticipated curves are quite similar to the experimental plots. The deviations of the predicted curves at higher temperatures and higher stress magnitudes indicate that the present model is applicable to the experimental creep data up to 3 MPa, even at higher temperatures. Moreover, the present model's applicability is limited at the stress of 4 MPa, as it fits the experimental data only at lower temperatures (up to 35°C). Therefore, the present model has some limitations at higher temperatures, particularly at higher stress levels. The potential reason for the deviations of the curves might be the occurrence of viscoplastic strains in PTFE samples at higher temperatures and higher stresses. Also, it is well known that the TTS method to produce the master curves only applies to the viscoelastic region. Furthermore, to improve the predictive accuracy of the model, the creep compliance master curves should be developed considering higher reference temperatures, which are in close proximity to the glass transition temperature (T_g) of PTFE. Previous research has demonstrated that selecting reference temperatures close to the T_g results in more accurate model predictions. (Dasappa 2008)

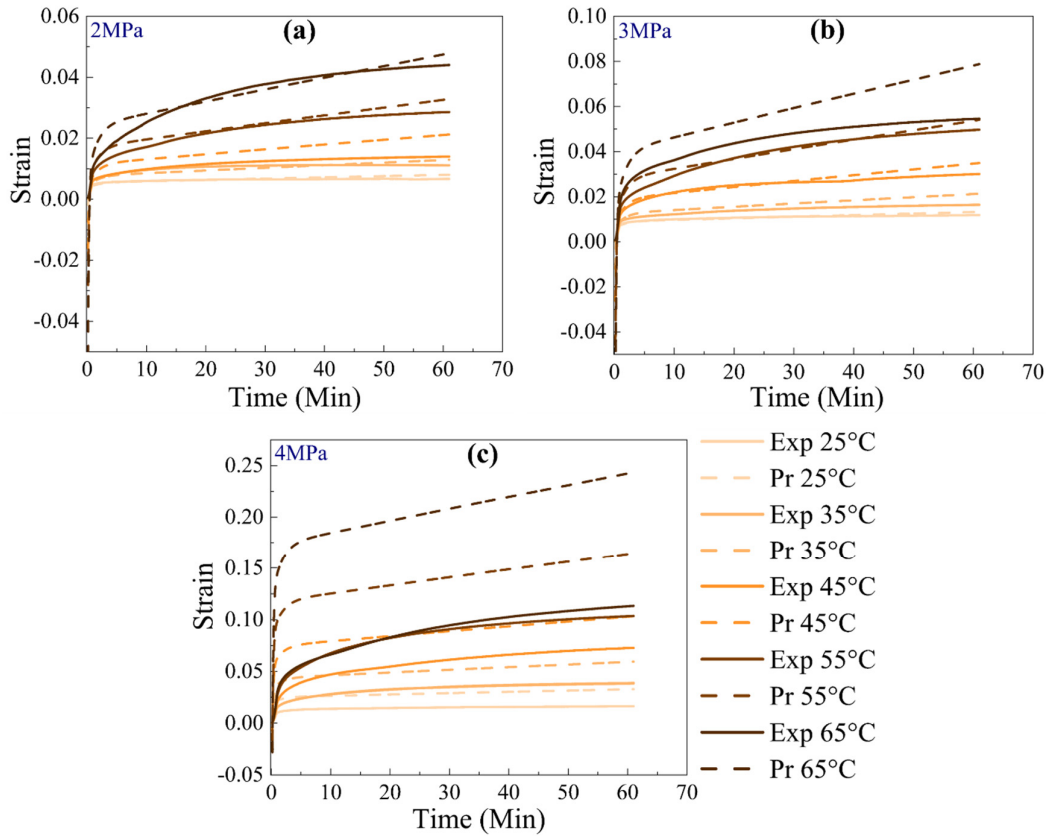


Figure 5.8 A comparison of the observed and anticipated stresses following one hour of creep at (a) 2 MPa, (b) 3 MPa, and (c) 4 MPa, at various temperatures in the range 25-65°C.

5.6 Concluding Remarks

Analysis of creep compliance on PTFE samples is performed by developing the master curves at the reference temperature 25°C, at stress levels of 2, 3, and 4 MPa utilizing the TTS method. The creep compliance master curve of PTFE samples is predicted for 4.5 hours. With the exception of the predicted creep curves at 4 MPa, the model's forecasts for stress levels of 2 and 3 MPa at higher temperatures are fairly consistent with the Exp. results. Furthermore, the predictions made at 4 MPa are inconsistent with the Exp. creep results at higher temperatures (above 35°C). The deviations in the curves are potentially caused due to the development of viscoplastic strains in PTFE samples at higher temperatures, particularly at higher stresses. It is widely acknowledged that

the TTS method is appropriate only in the viscoelastic domain for developing the master curves. Therefore, in order to enhance the model's ability to predict accurately, it is recommended to construct the creep compliance master curves by considering a higher reference temperature (T_0) that is in close proximity to the glass transition temperature (T_g) of PTFE. Moreover, the creep compliance master curves should be constructed by selecting the lower stresses and minimizing the viscoplastic strain values in PTFE samples.

This thesis highlights the significance of PTFE sealant for its use in LT-PEMFCs under low stress and temperatures. It indicates that PTFE is an appropriate sealant material in LT-PEMFC working conditions for an extended period. Moreover, it can potentially be utilized as a sealant material for HT-PEMFCs, operating at temperatures ranging from 120°C to 200°C.

5.7 Closure

The present chapter addresses the sealant's creep response by developing a model utilizing the TTS approach, along with the WLF equation, to forecast the creep compliance of PTFE sealant for an extended period. In the following chapter, the performance of a three-dimensional PEMFC model is evaluated in the presence of accelerated creep in PTFE sealant.

CHAPTER 6

EVALUATING THE PEM FUEL CELL PERFORMANCE UNDER ACCELERATED CREEP OF SEALANTS

6.1 Introduction

6.1.1 Sealants' accelerated creep

The present study focuses on the sealants' creep response resulting from compressive loading conditions, and on the longevity and performance of the PEMFC. The prediction of creep behavior at elevated temperatures (accelerated creep) in a shorter time interval is achieved by developing a master curve at a reference temperature, utilizing the TTS technique. The master curve thus obtained mimics the creep compliance results at the reference temperature for an extended period. The present study thus investigates in detail the influence of PTFE sealants' accelerated creep on transport properties, thereby, on PEMFC performance. The objective of this work is to acquire a comprehensive knowledge of the performance of PEM fuel cells, as a result of accelerated creep in sealants. In order to estimate the accelerated creep in PTFE sealant, Figure 6.1 is constructed using Figure 3(a) from the ref. (Kumar and Koorata 2024).

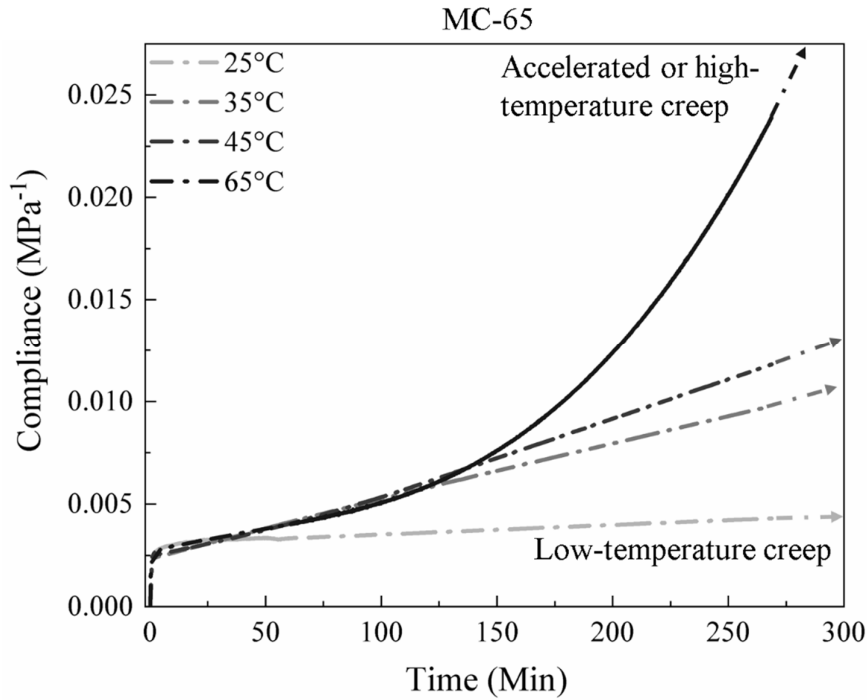


Figure 6.1 Creep compliances at various temperatures 25, 35, 45, and 65°C, showing the impact of accelerated creep (MC-65).

6.2 Model description

6.2.1 Structural model with creep analysis

A two-dimensional PEMFC numerical model is considered for the accelerated creep analysis of sealants. The dimensional details of the model are mentioned in Table 6.1. The 2D PEMFC model consists of 320714 number of elements. It consists of 320666 elements of type CPS4 and 48 elements of type CPS3. Figure 6.2 illustrates the GDL deformation along the length after the static and creep steps in 2D PEM fuel cell model considered for creep study. The sealants' accelerated creep analysis is conducted by incorporating the 2D PEMFC model in ABAQUS.

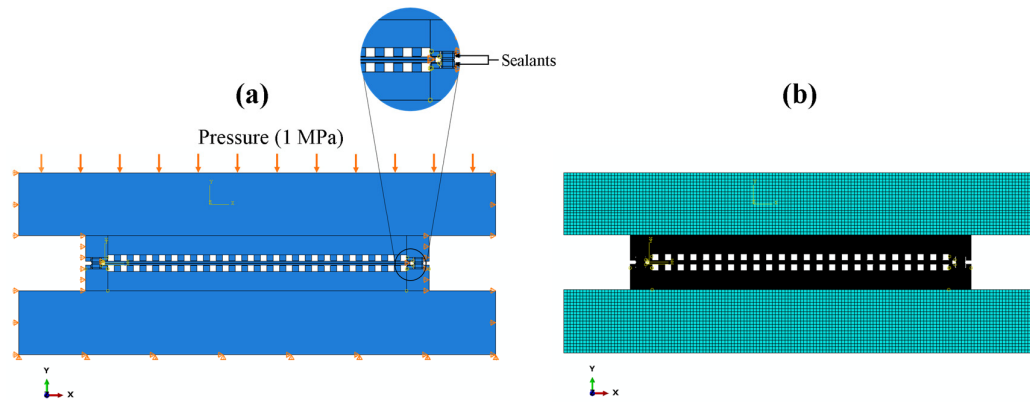


Figure 6.2 Structural model of PEMFC showing (a) load and boundary conditions, and (b) Meshed model considered for the creep analysis of PTFE sealant.

Table 6.1 Dimensions and material characteristics of 2D PEM fuel cell components

Components	Materials	Young's Modulus (MPa)	Source	Poisson's Ratio	Dimensions (mm)	Fillet Radius (mm)
Endplates	Aluminium	71000	(Shinde and Koorata 2021a)	0.33	75×10	-
Bipolar Plate	Graphite	10000	(Shinde and Koorata 2021a)	0.30	54×4	-
BPP Channels	Graphite	10000	(Shinde and Koorata 2021a)	0.30	1×1	0.1
Gas Diffusion Layer	Carbon Paper	-	(Koorata and	-	48×0.25	-

PEM	Nafion	177.4	Bhat 2021) (Koorat a and Bhat 2021)	0.25	48×0.05	-
Gaskets	PTFE	420	(Nunes et al. 2011)	0.46	1.52×0.85	0.2
Catalyst Layer	Pt/C	240	(Poorne sh and Cho 2011a)	0.25	48×0.015	

Table 6.2 Anisotropic material properties for GDL (Poornesh et al. 2012)

Material Constants	Value (MPa)
E₁	5600
E₂	9
E₃	2300
μ₁₂, μ₂₃, μ₁₃	0 (Assumed due to high GDL porosity)
G₁₂	50
G₂₃	50
G₁₃	1

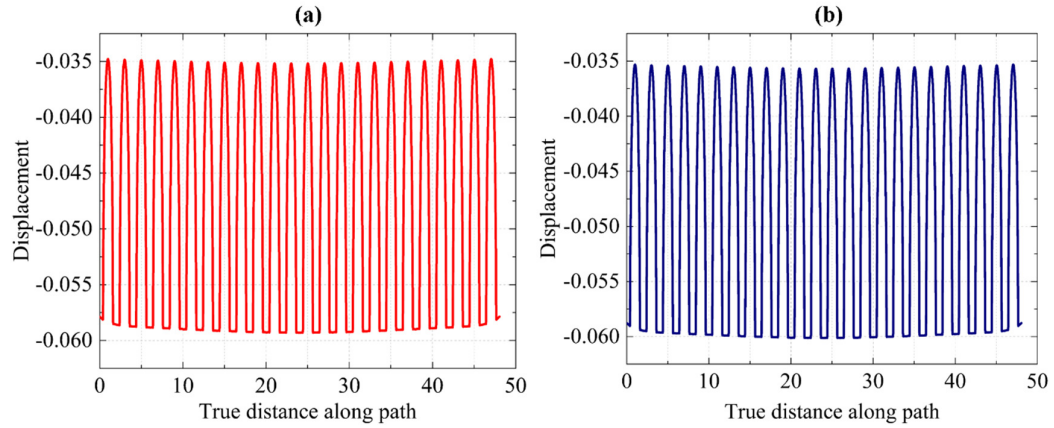


Figure 6.3 Shows GDL deformation along the length after the (a) static analysis (step-1), and (b) creep analysis (step-2) for the PTFE sealant.

6.2.2 Numerical model with flow, thermal and electrochemical analysis

The current study incorporates a 3D model of a single straight flow channel with an active area of 1cm^2 , as illustrated in Figure 6.3. Two different input parameters considered for the numerical study, (a) GDL porosity and permeability without sealant creep, and (b) with sealants' accelerated creep, are substituted into the model. In the first case, the input parameters are obtained from the refs. (Li et al. 2018b; Padavu et al. 2023) whereas in the second case, the parameters are obtained from the accelerated creep analysis on PTFE sealants in PEMFCs. Anode and cathode flow channels transmit hydrogen and oxygen gases, respectively. The details of PEM fuel cell model dimensions and working condition variables are summarised in Tables 6.3, 6.4 and 6.7. The PEM fuel cell working temperature and pressure are considered to be 353.15 K and 1atm, respectively. Apart from this, a 100% RH is employed for the reactant gases at both electrodes. The model taken into consideration for this study consists of a cell having length and width of 50 mm and 2 mm, respectively.

The present model also takes into consideration the transport of dissolved water and liquid water in the catalyst layer and membrane, as indicated in Eqn (6.22) and Eqn (6.23), respectively. The detailed variables utilized in the current model are illustrated in Table 6.1. The numerical simulation is performed utilizing the PEMFC module in ANSYS Fluent 2022 R1.

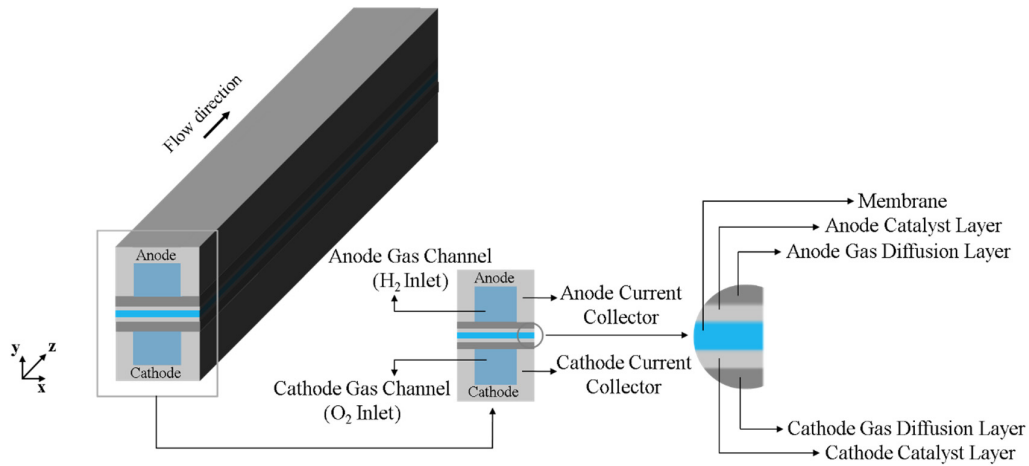


Figure 6.4 Single channel PEMFC model used for simulation

6.3 Model assumptions

The presumptions considered for the model as mentioned below:

- The gas movement is presumed as incompressible (due to small pressure gradients), laminar (low flow velocities) and steady-state behaviour.
- The gases are considered to follow the ideal gas law.
- The flow of gases is considered to be multiphase.
- The gravitational effect is neglected for the study.
- PEM fuel cell is assumed to operate under non-isothermal conditions due to heat generation during the electrochemical reaction.
- The membrane is considered to be impervious to reactants; therefore, the crossover of reactants is negligible.
- Water formed at the cathode catalyst is presumed to exist in dissolved or vapour form.
- GDL and CL at both electrodes and the membrane material characteristics are adopted as homogeneous and isotropic.

6.4 Mesh details

The 3D model utilized in the present study incorporates a flow channel, GDL, CL, and membrane. The numerical model with a straight flow field is implemented using a hexahedral mesh type. A single channel (1mm×1mm) (width×height) is considered for the numerical study. The number of grids considered for meshing in X, Y and Z-directions are 20, 70 and 500, respectively.

6.5 Methodology

6.5.1 Governing Equations

The current investigation includes the equations for the conservation of mass, momentum, energy, species, and water vapour, as mentioned below:

6.5.1.1 Continuity Equation

The continuity equation for present study is as stated by the refs. (Li et al. 2017; Padavu et al. 2021a)

$$\nabla \cdot (\rho \vec{U}) = S_m \quad (6.1)$$

The source term can be explained as:

$$\text{At Anode CL, } S_{m(H_2)} = \frac{-J_{an}}{2F} \cdot M_{H_2} \text{ (kgm}^{-3}\text{s}^{-1}\text{)} \quad (6.2)$$

$$\text{At Cathode CL, } S_{m(O_2)} = \frac{-J_{cat}}{4F} \cdot M_{O_2} \text{ (kgm}^{-3}\text{s}^{-1}\text{)} \quad (6.3)$$

$$\text{and, } S_{m(H_2O)} = \frac{J_{cat}}{2F} \cdot M_{H_2O} \text{ (kgm}^{-3}\text{s}^{-1}\text{)} \quad (6.4)$$

6.5.1.2 Momentum conservation

The momentum conservation equation for the present model can be written from the ref. (Padavu et al. 2021a)

$$\nabla \cdot (\rho \vec{U} \vec{U}) = -\nabla p + \nabla \cdot (\mu \nabla \vec{U}) + S_{mom} \quad (6.5)$$

$$S_{mom} = \frac{-\mu}{\kappa} \bar{U} \quad (\text{kgm}^{-2}\text{s}^{-2}) \quad (6.6)$$

6.5.1.3 Electronic charge conservation

The electronic charge conservation for the present model is as given by the ref. (Li et al. 2017; Padavu et al. 2021a)

$$\nabla \cdot (\sigma_{el.}^{eff} \nabla \phi_{el.}) + S_{el.} = 0 \quad (6.7)$$

Bruggeman correlation is utilized to evaluate the effective electronic conductivity and is shown as follows:

$$\sigma_{el.}^{eff} = \psi^{3/2} \sigma_{el.} \quad (6.8)$$

The source term for electronic charge conservation can be expressed as below,

$$\text{At the anode CL, } S_{el.} = -J_{an} (\text{Am}^{-3}) \quad (6.9)$$

$$\text{At the cathode CL, } S_{el.} = +J_{cat} (\text{Am}^{-3}) \quad (6.10)$$

6.5.1.4 Ionic charge conservation

The ionic charge conservation in the present model is followed by the refs. (Li et al. 2017; Padavu et al. 2021a)

$$\nabla \cdot (\sigma_{mem}^{eff} \nabla \phi_{mem}) + S_{mem} = 0 \quad (6.11)$$

The ionic conductivity is evaluated as expressed below,

$$\sigma_{mem} = (0.5139\lambda - 0.326) \times e^{\left[1268 \left(\frac{1}{303} - \frac{1}{T}\right)\right]} \quad (6.12)$$

$$\lambda_{mem} = \begin{cases} 0.043 + 17.18\omega_a - 39.85\omega_a^2 + 36.0\omega_a^3; & 0 \leq \omega_a \leq 1 \\ 14 + 4(\omega_a - 1); & 1 < \omega_a \leq 3 \end{cases} \quad (6.13)$$

$$\text{Where} \quad \omega_a = \frac{P_{wv}}{P_{sat}} \quad (6.14)$$

The source term used for the ionic charge is expressed as below,

$$\text{At the anode CL, } S_{mem} = +J_{an} \quad (\text{Am}^{-3}) \quad (6.15)$$

$$\text{At the cathode CL, } S_{mem} = -J_{cat} \quad (\text{Am}^{-3}) \quad (6.16)$$

6.5.1.5 Species conservation

The conservation of species in the present model is as given by the refs. (Li et al. 2017; Padavu et al. 2021a)

$$\nabla \cdot (\rho \vec{U} X_i) = \nabla \cdot (\rho D_i^{eff} \nabla X_i) + S_{sp.} \quad (6.17)$$

The coefficient of mass diffusion for the reactant gases in the flow channels can be expressed as follows:

$$D_i = D_0 \left(\frac{T}{T_0} \right)^{3/2} \left(\frac{P_0}{P} \right) \quad (6.18)$$

The coefficient of mass diffusion for the reactive gases in GDL and CL, taking into account the Bruggeman correlation, can be expressed as,

$$D_i^{eff} = \psi_i^{3/2} D_i \quad (6.19)$$

The source terms for species can be expressed as,

$$\text{At the anode CL, } S_{H_2} = \frac{-J_{an}}{2F} M_{H_2} \quad (\text{kgm}^{-3}\text{s}^{-1}), \quad (6.20)$$

$$\text{At Cathode CL, } S_{O_2} = \frac{-J_{cat}}{4F} M_{O_2} \quad (\text{kgm}^{-3}\text{s}^{-1}), \quad S_{H_2O} = \frac{J_{cat}}{2F} M_{H_2O} \quad (\text{kgm}^{-3}\text{s}^{-1}) \quad (6.21)$$

6.5.1.6 Dissolved phase model

Water flow in its dissolved phase within CL and membrane is followed by the refs (Wang and Wang 2005; Wu et al. 2009)

$$\nabla \cdot \left(-\sigma_{mem} \nabla \phi_{mem} \frac{n_d}{F} M_{H_2O} \right) = \nabla \cdot (M_{H_2O} D_w \nabla \lambda) + S_\lambda + S_{gd} + S_{ld} \quad (6.22)$$

6.5.1.7 Liquid phase model

The transition of water among the liquid phase and water vapor in the catalyst layer and membrane is then followed by the ref. (Scholz 2015)

$$\nabla \cdot \left(\frac{\rho_l \kappa \kappa_r}{\mu_l} \nabla (p_c + p) \right) + S_{gl} - S_{ld} = 0 \quad (6.23)$$

6.5.1.8 Electrochemistry Modelling

The electrochemical reactions are driven by the variation in the phase potentials between the solid and that of the membrane. The electrochemistry model used in the study is followed by the refs (Kulikovsky et al. 1999; Um et al. 2000)

$$\nabla \cdot (\sigma_{el.} \nabla \phi_{el.}) + J_{el.} = 0 \quad (6.24)$$

$$\nabla \cdot (\sigma_{mem.} \nabla \phi_{mem.}) + J_{mem.} = 0 \quad (6.25)$$

The source terms in Eqn (6.24) and Eqn (6.25), also known as exchange current density (Am^{-3}), have the following definitions,

$$J_{an} = \left(\nu_{an} \cdot j_{an}^{ref} \cdot e^{-E_{an}/RT(1-T/T_{an}^{ref})} \right) \left(\frac{[H_2]}{[H_2]_{ref}} \right)^{1/2} \left(e^{\beta_{an}^{an} \cdot F \cdot \eta_{an}/RT} - e^{-\beta_{an}^{an} \cdot F \cdot \eta_{an}/RT} \right) \quad (6.26)$$

$$J_{cat} = \left(\nu_{cat} \cdot j_{cat}^{ref} \cdot e^{-E_{cat}/RT(1-T/T_{cat}^{ref})} \right) \left(\frac{[O_2]}{[O_2]_{ref}} \right)^1 \left(-e^{\beta_{cat}^{cat} \cdot F \cdot \eta_{cat}/RT} + e^{-\beta_{cat}^{cat} \cdot F \cdot \eta_{cat}/RT} \right) \quad (6.27)$$

6.5.1.9 Half-cell potential

The surface overpotential that drives fuel cell kinetics and is expressed as,

$$\eta_{an} = \phi_{el.} - \phi_{mem} - V_{an}^0 \quad (6.28)$$

$$\eta_{cat} = \phi_{el.} - \phi_{mem} - V_{cat}^0 \quad (6.29)$$

The half-cell potentials, and are evaluated utilizing Nernst equations as follows (Scholz 2015),

$$V_{an}^0 = E_{an}^r - \frac{\Delta S_{an}}{2F} \cdot (T - T_0) - \frac{RT}{2F} \cdot \ln\left(\frac{P_{H_2}}{P_0}\right) \quad (6.30)$$

$$V_{cat}^0 = E_{cat}^r - \frac{\Delta S_{cat}}{2F} \cdot (T - T_0) - \frac{RT}{2F} \cdot \ln\left(\frac{P_{H_2O}}{P_{sat} \sqrt{P_{O_2} / P_0}}\right) \quad (6.31)$$

6.6 Boundary conditions

The gas channel walls are assumed to have a condition of no slip and zero flux. Apart from this, the back pressure at the anode and cathode outlet is neglected in this study.

$\phi_{el.} = 0$ is considered at the anode wall, and $\phi_{el.} = V_{cell}$ is considered at the cathode wall.

6.6.1 Mole fraction at inlet

The mole fraction at anode inlet is evaluated as expressed by the ref (Padavu et al. 2021a),

$$P_{sat.} = \left[10^{(-2.1794 + (0.02953) \times (T - 273) - (9.1837 \times 10^{-5}) \times (T - 273)^2 + (1.4454 \times 10^{-7}) \times (T - 273)^3)} \right] \times 101325 \quad (6.32)$$

$$y_{H_2O}^{an} = \frac{P_{sat.}}{P_{an}} \cdot RH_{an} \quad (6.33)$$

$$y_{H_2} = 1 - y_{H_2O}^{an} \quad (6.34)$$

Similarly, mole fraction at the inlet of cathode is evaluated as expressed by the ref. (Padavu et al. 2021a),

$$P_{sat.} = \left[10^{(-2.1794 + (0.02953) \times (T - 273) - (9.1837 \times 10^{-5}) \times (T - 273)^2 + (1.4454 \times 10^{-7}) \times (T - 273)^3)} \right] \times 101325 \quad (6.35)$$

$$y_{H_2O}^{cat} = \frac{P_{sat.}}{P_{cat}} \cdot RH_{cat} \quad (6.36)$$

$$y_{O_2} = 0.21 \times (1 - y_{H_2O}^{cat}) \quad (6.37)$$

6.6.2 Mass flow rate

Mass flow rate at the anode inlet is expressed, as by the ref (Li et al. 2017),

$$\dot{m}_{an,i} = \frac{\xi_{an} \cdot I_{ref} \cdot A_m \cdot M_{H_2}}{2F \cdot X_{H_2}} \quad (6.38)$$

Mass flow rate at cathode inlet is also expressed, as by the ref (Li et al. 2017),

$$\dot{m}_{cat,i} = \frac{\xi_{cat} \cdot I_{ref} \cdot A_m \cdot M_{O_2}}{4F \cdot X_{O_2}} \quad (6.39)$$

6.6.3 Modelling variables

The PEMFC model dimensions taken into account for the single straight-flow field design are mentioned in Table 6.3, which are comparable to the dimensions considered in ref (Shinde et al. 2023). Table 6.4 presents a list of the input variables that comprise the current numerical model for a single straight flow channel of the PEMFC. The primary equations and the source terms considered in this study are mentioned in Tables 6.5 and 6.6, respectively. The mole fractions of the reactants for maximum humidity and the multiphase mixture expressions are mentioned in Table 6.7, 6.8, and 6.9 respectively.

6.6.3.1 GDL porosity and permeability

The local porosity of GDL can be achieved, as given by the ref (Li and Sundén 2018)

$$\psi_f = 1 - (1 - \psi_0) \cdot \frac{t_0}{t} \quad (6.40)$$

Similarly, the local permeability of the GDL can be achieved, as given by the ref (Wang and Chen 2011)

$$\kappa_f = \frac{d_p^2}{150} \cdot \frac{\psi_f^3}{(1 - \psi_f)^2} \quad (6.41)$$

The parameters used in Eqn (6.1) to Eqn (6.41) are specified in the Nomenclature of this thesis.

Table 6.3 Geometrical dimensions and working environment.

Parameter	Value
Cell length, L_{cell}	50 mm
Cell width, W_{cell}	2 mm
GC width, L_{ch}	1 mm
GC height, H_{ch}	1 mm
GC length, L_{ch}	50 mm
CC rib width	1 mm
CC rib height	0.5 mm
GDL thickness	0.25 mm
CL thickness	0.015 mm
Membrane thickness	0.05 mm
Active area of the gas channel	100 mm ²
Anode/Cathode Pressure, $P_{\text{an}} / P_{\text{cat}}$	1/1 atm
Anode/Cathode Relative Humidity, $RH_{\text{an}} / RH_{\text{cat}}$	100%/100%
Operating temperature, $T_{\text{an}} / T_{\text{cat}}$	353.15K/353.15 K

Table 6.4 Kinetic, transport and physiochemical properties utilized in the PEM fuel cell model

Description	Value	Unit	Ref.
Stoichiometric ratio at anode, ξ_{an}	1.5	-	(Li et al. 2018b)
Stoichiometric ratio at cathode, ξ_{cat}	2.0	-	(Li et al. 2018b)
Reference current density, I_{ref}	10,000	A m ⁻²	(Padavu et al. 2023)
Specific active area, ν	2,00,000	m ⁻¹	(Carcadea et al. 2018)
Exchange current density at anode, j_{an}^{ref}	5x10 ⁸	A m ⁻²	(Li et al. 2017)
Exchange current density at cathode, j_{cat}^{ref}	2.5x10 ²	A m ⁻²	(Li et al. 2017)
Activation energy of anode, E_{an}	11640258	J kmol ⁻¹ K ⁻¹	Calculated using reference equation (Li et al. 2017)
Activation energy of cathode, E_{cat}	65684313	J kmol ⁻¹ K ⁻¹	Calculated using reference equation (Li et al. 2017)
Reference H ₂ molar concentration, $[H_2]_{ref}$	0.04088	kmol m ⁻³	(Li et al. 2017)
Reference O ₂ molar concentration, $[O_2]_{ref}$	0.04088	kmol m ⁻³	(Li et al. 2017)
Transfer exponent at anode, c_{an}	0.5	-	(Padavu et al. 2023)
Transfer exponent at cathode, c_{cat}	1.0	-	(Padavu et al. 2023)
Transfer coefficient at anode, β_{an}	1.0	-	(Padavu et al. 2023)

Transfer coefficient at cathode, β_{cat}	1.0	-	(Padavu et al. 2023)
Anode and cathode reference Temperature, $T_{an}^{ref} / T_{cat}^{ref}$	353.15/353.15	K	(Li et al. 2017)
Porosity of gas diffusion layer, ψ_{GDL}	(a) 0.6	-	(Li et al. 2018b)
	(b)0.5023(AGDL), 0.5788(CGDL)	-	[calculated]
Permeability of gas diffusion layer, κ_{GDL}	(a) 5.6×10^{-12}	m^2	(Li et al. 2018b)
	(b) 3.52×10^{-13} (AGDL), 7.41×10^{-13} (CGDL)	m^2	[calculated]
Porosity of catalyst layer, ψ_{CL}	0.2	-	(Li et al. 2017)
Permeability of catalyst layer, κ_{CL}	1×10^{-13}	m^2	(Li et al. 2018b)
Electron conductivity of CC, GDL and CL, $\sigma_{CC/GDL/CL}$	20,000/5000/2000	$S m^{-1}$	(Li et al. 2018b)
Faraday constant, F	96,485	$C mol^{-1}$	(Padavu et al. 2023)
Universal gas constant, R	8.314	$J mol^{-1} K^{-1}$	(Padavu et al. 2023)
Contact angle of GDL/CL, $\theta_{GDL/CL}$	$110^\circ/95^\circ$	-	(Li et al. 2018b)
Working pressure, P (Anode & Cathode)	1	Atm	(Li et al. 2018b)
Working temperature, T	353.15	K	(Li et al. 2018b)

Working cell voltage, V	1.0 to 0.4	V	(Padavu et al. 2023)
Mass flow rate, anode inlet, $\dot{m}_{an,i}$	1.366721×10^{-7}	kg s ⁻¹	[calculated]
Mass flow rate, cathode inlet, $\dot{m}_{cat,i}$	1.096027×10^{-6}	kg s ⁻¹	[calculated]
Water mole fraction at cathode inlet, $y_{H_2O}^{cat}$	0.4640	-	(Padavu et al. 2023)
H ₂ mole fraction at anode inlet, $y_{H_2}^{an}$	0.5360	-	(Padavu et al. 2023)
O ₂ mole fraction at cathode inlet, $y_{O_2}^{cat}$	0.1126	-	(Padavu et al. 2023)
Entropy of reaction at anode, ΔS_{an}	104	J kmol ⁻¹ K ⁻¹	(Li et al. 2018b)
Entropy of reaction at cathode, ΔS_{cat}	-326360	J kmol ⁻¹ K ⁻¹	(Li et al. 2018b)
Membrane equivalent weight, M_{eq}	1100	kg kmol ⁻¹	(Li et al. 2018b)
Thermal conductivity of CC/GDL/CL, k_s	100/1.7/0.3	W m ⁻¹ K ⁻¹	(Li et al. 2018b)
Thermal conductivity of Membrane, k_{mem}	0.25	W m ⁻¹ K ⁻¹	(Li et al. 2018b)
Condensation rate, δ_c	100	s ⁻¹	(Jiao and Li 2011)
Evaporation rate, δ_e	100	s ⁻¹	(Jiao and Li 2011)
Water removal coefficient, Θ	5×10^{-5}	Sm ⁻¹	(Arif et al. 2020)

AGDL: Anode gas diffusion layer, CGDL: Cathode gas diffusion layer

Table 6.5 The governing equations used for the study

Entity	Equations
Mass	$\nabla \cdot (\rho \vec{U}) = S_m$
Momentum	$\nabla \cdot (\rho \vec{U} \vec{U}) = -\nabla p + \nabla \cdot (\mu \nabla \vec{U}) + S_{mom}$
Energy	$\nabla \cdot (\rho c_p \vec{U} T) = \nabla \cdot (k_{eff} \Delta T) + S_T$
Charge	$\nabla \cdot (\sigma_{el.}^{eff} \cdot \nabla \phi_{el.}) + S_{el.} = 0$
	$\nabla \cdot (\sigma_{mem}^{eff} \cdot \nabla \phi_{mem}) + S_{mem} = 0$
Species	$\nabla \cdot (\rho \vec{U} X_i) = \nabla \cdot (\rho D_i^{eff} \cdot \nabla X_i) + S_{sp.}$

Table 6.6 Source terms considered for the PEMFC model (Chippar and Ju 2013; Jiao and Li 2011; Yin et al. 2014)

Source term	Unit	Zone
$S_m = S_{H_2}$	$\text{kg m}^{-3} \text{s}^{-1}$	Anode catalyst
$S_m = S_{O_2}$	$\text{kg m}^{-3} \text{s}^{-1}$	Cathode catalyst
$S_m = S_{H_2O}$	$\text{kg m}^{-3} \text{s}^{-1}$	Cathode catalyst
$S_{mom} = -\frac{\mu}{K} \vec{U}$	$\text{kg m}^{-2} \text{s}^{-2}$	Anode/Cathode gas diffusion & catalyst layer
$S_T = J_{an} \eta_{an} - \frac{T \cdot \Delta S_{an}}{2F} \cdot J_{an} + \sigma_{mem}^{eff} \nabla \phi_{mem}^2 + \sigma_{el.}^{eff} \nabla \phi_{el.}^2$	W m^{-3}	Anode catalyst
$S_T = J_{cat} \eta_{cat} - \frac{T \cdot \Delta S_{cat}}{4F} \cdot J_{cat} + \sigma_{mem}^{eff} \nabla \phi_{mem}^2 + \sigma_{el.}^{eff} \nabla \phi_{el.}^2$	W m^{-3}	Cathode catalyst
$S_T = \sigma_{mem}^{eff} \nabla \phi_{mem}^2$	W m^{-3}	Membrane
$S_T = \sigma_{el.}^{eff} \nabla \phi_{el.}^2$	W m^{-3}	Anode & cathode gas diffusion layer
$S_T = \sigma_{el.}^{eff} \nabla \phi_{el.}^2$	W m^{-3}	Anode & cathode current collectors
$S_{el.} = -J_{an}$	A m^{-3}	Anode catalyst
$S_{el.} = +J_{cat}$	A m^{-3}	Cathode catalyst
$S_{mem} = +J_{an}$	A m^{-3}	Anode catalyst
$S_{mem} = -J_{cat}$	A m^{-3}	Cathode catalyst

$S_{H_2} = -\frac{J_{an}}{2F} \cdot M_{H_2}$	kg m ⁻³ s ⁻¹	Anode catalyst
$S_{O_2} = -\frac{J_{cat}}{2F} \cdot M_{O_2}$	kg m ⁻³ s ⁻¹	Cathode catalyst
$S_{H_2O} = -\frac{J_{cat}}{2F} \cdot M_{H_2O}$	kg m ⁻³ s ⁻¹	Cathode catalyst
$S_l = S_{phase}$	kg m ⁻³ s ⁻¹	Anode/Cathode gas diffusion & catalyst layer
$S_{phase} = \begin{cases} \delta_c \cdot \frac{\psi(1-s)}{RT} \cdot M_{H_2O} \cdot (p_{wv} - p_{sat}); & p_{wv} \geq p_{sat} \\ \delta_e \cdot \frac{\psi s}{RT} \cdot M_{H_2O} \cdot (p_{wv} - p_{sat}); & p_{wv} < p_{sat} \end{cases}$	kg m ⁻³ s ⁻¹	
$S_d = S_{vd}$	mol m ⁻³ s ⁻¹	Anode catalyst
$S_d = S_{vd} + S_\lambda$	mol m ⁻³ s ⁻¹	Cathode catalyst
$S_\lambda = M_{H_2O} \cdot \frac{J_{cat}}{2F}$		Cathode catalyst

Table 6.7 Mole fraction of reactants taken into account for maximum humidity

Parameter	Humidity	Value	Reference
Inlet anode hydrogen mole fraction, y_{H_2}	100%	0.5360	[calculated]
Inlet anode oxygen mole fraction, y_{O_2}	100%	0.1126	[calculated]
Inlet anode water mole fraction, $y_{H_2O}^{an}$	100%	0.4640	[calculated]
Inlet cathode water mole fraction, $y_{H_2O}^{cat}$	100%	0.4640	[calculated]

Table 6.8 Mathematical definitions of the variables used in Eqn (6.22) (Carcadea et al. 2018; Scholz 2015)

Description	Expression	Units
Osmotic drag coefficient	$n_d = 2.5 \frac{\lambda}{22}$	-
Water diffusion coefficient	$D_w = \frac{\rho_i}{M_{eq}} \times 4.1 \times 10^{-10} \left(\frac{\lambda}{25} \right)^{0.15} \left[1 + \tanh \left(\frac{\lambda - 2.5}{1.4} \right) \right]$	m^2s^{-1}
Source term for dissolved water content	$S_\lambda = M_{H_2O} \cdot \frac{J_{cat}}{2F}$	$kgm^{-3}s^{-1}$
Mass conversion rate for gas and dissolved phase	$S_{gd} = (1-s) \delta_{gd} \cdot M_{H_2O} \cdot \frac{\rho_i}{M_{eq}} \cdot (\lambda_{eq} - \lambda)$	$kgm^{-3}s^{-1}$
Mass conversion rate for liquid and dissolved phase	$S_{ld} = s \cdot \delta_{ld} \cdot M_{H_2O} \cdot \frac{\rho_i}{M_{eq}} \cdot (\lambda_{eq} - \lambda)$	$kgm^{-3}s^{-1}$
Equilibrium water content	$\lambda_{eq} = 0.3 + 6\omega_a (1 - \tanh(\omega_a - 0.5)) + 0.69(\lambda_{a=1} - 3.52)\omega_a^{0.5} \cdot \left(1 + \tanh \left(\frac{\omega_a - 0.89}{0.23} \right) \right) + s \cdot (\lambda_{s=1} - \lambda_{a=1})$	mol H ₂ O (mol SO ₃ H) ⁻ 1
Water activity	$\omega_a = \frac{P_{wv}}{P_{sat}}$	-

Table 6.9 Mathematical definitions of the variables used in Eqn (6.23) (Scholz 2015; Wang and Wang 2005; Weber and Newman 2004)

Description	Expression
Relative permeability, (GDL)	$\kappa_r = s^b$
Relative permeability (Membrane)	$\kappa_r = \left(\frac{\frac{M_{H_2O}}{\rho_l} \cdot \lambda_{s=1} + \frac{M_{eq}}{\rho_l} \cdot \lambda}{\frac{M_{H_2O}}{\rho_l} \cdot \lambda + \frac{M_{eq}}{\rho_l} \cdot \lambda_{s=1}} \right)^2$
Mass change rate among gas and liquid phases	$S_{gl} = \begin{cases} \delta_e \cdot \psi \cdot s \cdot D_{gl} \frac{M_{H_2O}}{RT} \cdot p \ln \left(\frac{p - p_{sat}}{p - p_{wv}} \right), & p_{wv} \leq p_{sat} \\ \delta_c \cdot \psi \cdot (1-s) \cdot D_{gl} \frac{M_{H_2O}}{RT} \cdot p \ln \left(\frac{p - p_{sat}}{p - p_{wv}} \right), & p_{wv} > p_{sat} \end{cases}$
D_{gl} (Anode & Cathode)	$D_{gl} = \begin{cases} 0.365 \times 10^{-4} \left(\frac{T}{343} \right)^{2.334} \left(\frac{10^5}{p} \right) \\ 1.79 \times 10^{-4} \left(\frac{T}{343} \right)^{2.334} \left(\frac{10^5}{p} \right) \end{cases}$
Capillary Pressure	$p_c = \begin{cases} \sigma \cos \theta \left(\frac{\psi}{\kappa} \right)^{1/2} \left(1.417(1-s) - 2.12(1-s)^2 + 1.263(1-s)^3 \right), & \theta \leq 90^\circ \\ \sigma \cos \theta \left(\frac{\psi}{\kappa} \right)^{1/2} \left(1.417s - 2.12s^2 + 1.263s^3 \right), & \theta > 90^\circ \end{cases}$

6.7 Results and Discussion

A straight single-channel PEMFC model is incorporated for the numerical investigation, as shown in Figure 6.3. The straight flow field design, with an active area of 1cm^2 , is considered for the maximum humidity (100%) conditions at the inlet as mentioned in the numerical model. The design variables and the working conditions are mentioned in Table 6.3, 6.4, and 6.7, respectively. The performance curve and the transport properties for the present model are further discussed in the following section.

6.7.1 Performance curves

The PEMFC performance is quantified utilizing the polarization curves, as illustrated in Figure 4. Above the cell voltage of 0.75V, the average current densities in both cases are identical. In case 1, the results are obtained by considering the input parameters from the refs (Li et al. 2018b; Padavu et al. 2023), whereas in case 2, the results are facilitated by taking into account the GDL porosity and permeability obtained from the sealants' accelerated creep. The results in case 1 are observed to give better performance compared to case 2, especially when the cell voltage is below 0.5V. The average current density for case 1 is $0.591987 \text{ Acm}^{-2}$, while for case 2 it is $0.486737 \text{ Acm}^{-2}$, at the voltage of 0.6V. Similarly, the average current density for case 1 is $1.309655 \text{ Acm}^{-2}$, while for case 2, it is $1.041806 \text{ Acm}^{-2}$, at the voltage of 0.4V. The variation in current density for case 1 and case 2 extends from 17.78 to 20.45% when the cell voltage is reduced from 0.6 to 0.4V.

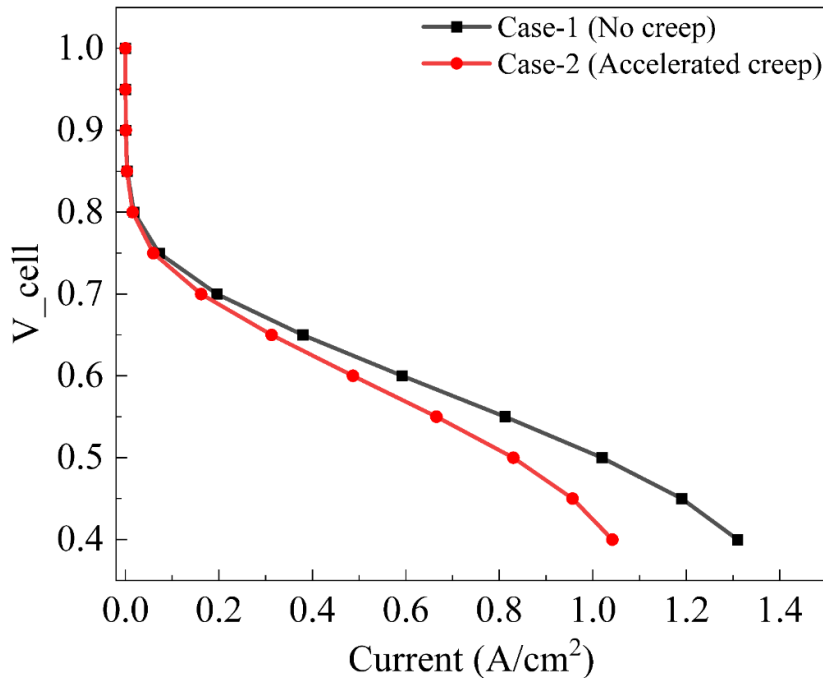


Figure 6.5 Single channel performance comparison of the PEM fuel cell for case-1 (no creep) with that of case-2 (sealants' accelerated creep).

6.7.2 Transport properties

Figure 6.6-6.8 shows the contour plots for H₂, O₂, and H₂O concentration variation in different sections of the fuel cell model. Figure 6.6(i) shows the H₂ concentration variation at the mid-plane of anode CL, at the voltage of 0.4V. The results show that in case 2, the diffusion of H₂ at the inlet and outlet is greater compared to case 1, indicating the higher consumption of H₂ in case 2. Figure 6.7(i) and 6.8(i) illustrate the O₂ concentration variation at the mid-plane of the cathode CL and cathode GDL, respectively. The findings in case 1 indicate a progressive decline in the O₂ concentration from the inlet to the outlet due to oxygen consumption and water generation, indicating enhanced oxygen reduction reaction (ORR). On the other hand, in case 2, the oxygen consumption is even lower, indicating a reduction in the ORR reaction. Figure 6.6(ii), 6.7(ii), and 6.8(ii) illustrate the H₂O concentration variation in the anode CL, cathode CL, and cathode GDL, respectively. The results indicate that the higher relative humidity (100%) of air results in higher H₂O concentration in the cathode CL and GDL outlet regions. Also, at the cathode CL and GDL outlet, there is a steady increment in H₂O concentration as oxygen is consumed and water is produced and accumulated. The water accumulation is higher at the cathode GDL outlet in case 2, compared to case 1, which lowered the cell performance. Furthermore, it is reported from these results that in case 2, the H₂O concentration at the outlet in anode CL is lowered by 70.45% compared to case 1.

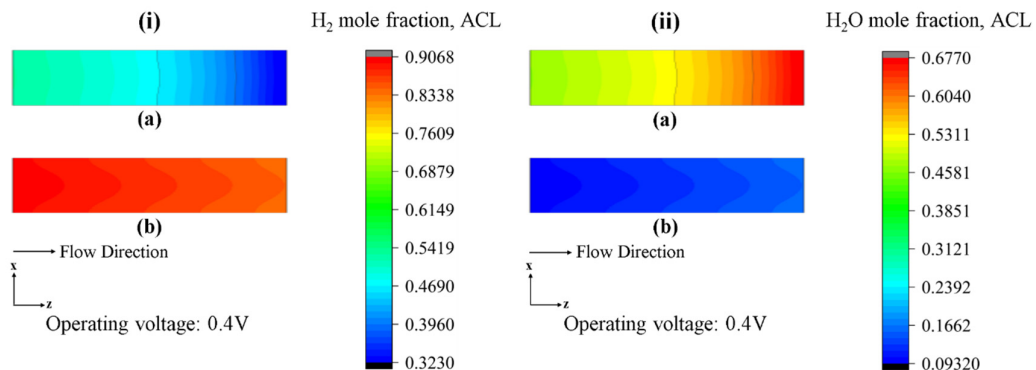


Figure 6.6 (i) H₂ mole fraction variation and (ii) H₂O mole fraction variation in anode CL, respectively, at 0.4V for (a) case 1, and (b) case 2.

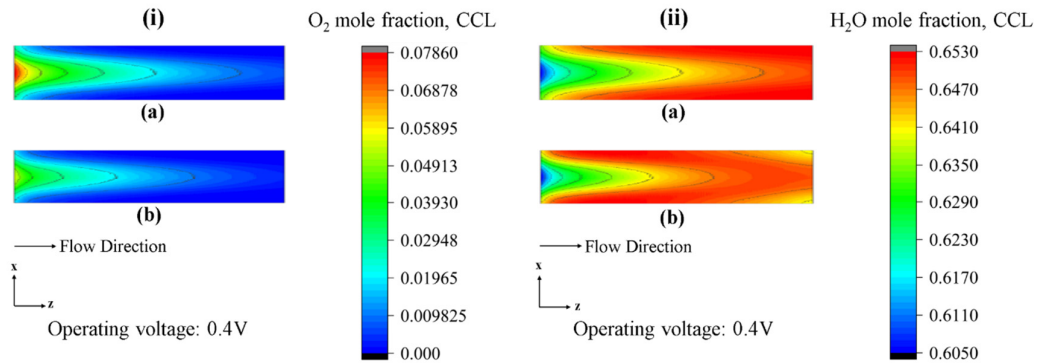


Figure 6.7 (i) O₂ mole fraction variation and (ii) H₂O mole fraction variation in cathode CL, respectively, at 0.4V for (a) case 1, and (b) case 2.

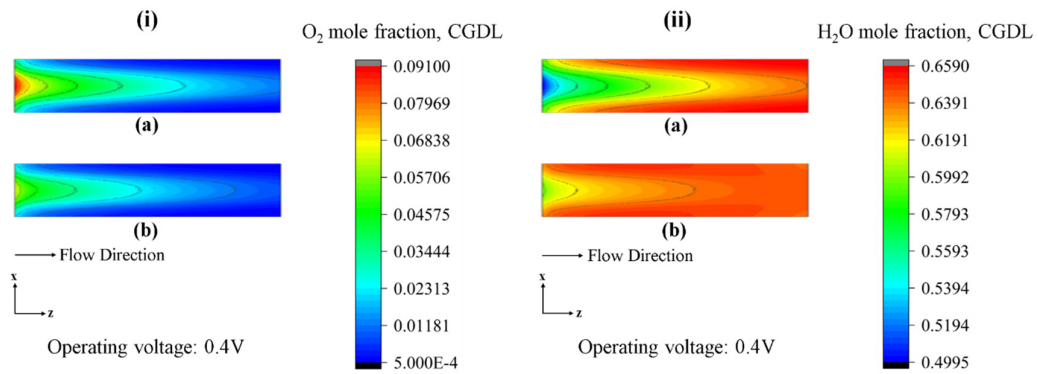


Figure 6.8 (i) O₂ mole fraction variation and (ii) H₂O mole fraction variation in cathode GDL, respectively, at 0.4V for (a) case 1, and (b) case 2.

Figure 6.9-6.12 shows the contour plots showing temperature, liquid saturation, water content, and current density variation in different sections of the fuel cell model. The temperature variation in cathode GDL and membrane at the cell voltage of 0.4V are illustrated in Figure 6.9(i) and 6.11(i), respectively. The findings suggest that the temperature under the rib region is lower than that under the flow channel region due to the higher thermal conductivity of the rib. Furthermore, there is a negligible drop in temperature at the cathode GDL and membrane. Figure 6.9(ii) indicates that in case 2, there is an increase in liquid saturation by 70.2% at the cathode GDL, compared to case 1, which is potentially caused due to the increase in pores size in GDL. This increase in pores size ultimately lowered the cell performance, which is in fair agreement with

the results in ref. (Ji and Wei 2009). Figure 6.10(i) and (ii) show the water content in the anode and cathode catalyst layer at the cell voltage of 0.4V. These findings indicate that in case 2, the water content is lowered by 36% at the anode catalyst layer outlet, while it is dropped by 13.65% at the cathode catalyst layer outlet, compared to case 1.

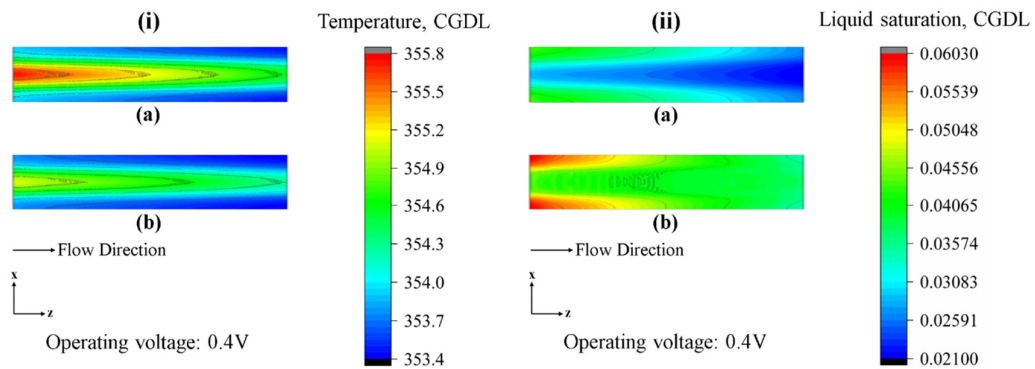


Figure 6.9 (i) Temperature distribution and (ii) Liquid saturation in cathode GDL, respectively, at 0.4V for (a) case 1, and (b) case 2.

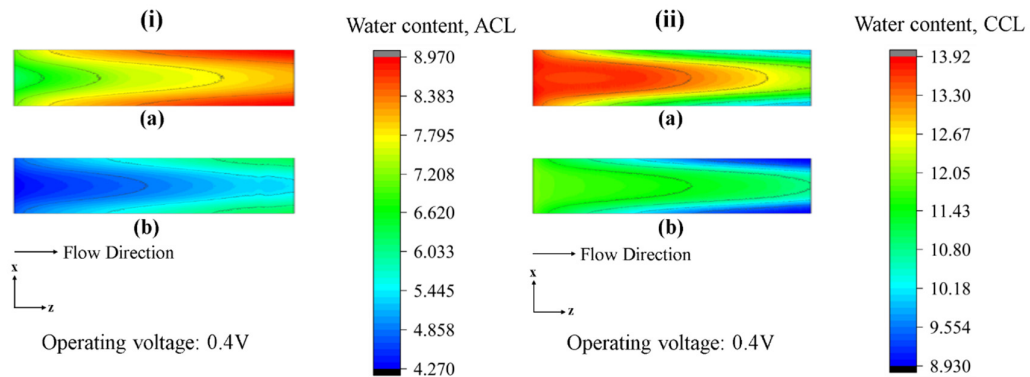


Figure 6.10 Water content at (i) anode CL and (ii) cathode CL, respectively, at 0.4V for (a) case 1, and (b) case 2.

The water content at the mid-section of the membrane at the voltage of 0.4V is depicted in Figure 6.11(ii). The result shows that in case 2, the water content is increased by 33.65% at the membrane outlet, compared to case 1. The result suggests that the ionic conductivity of the membrane is increased due to the increase in water content in case 2, compared to case 1.

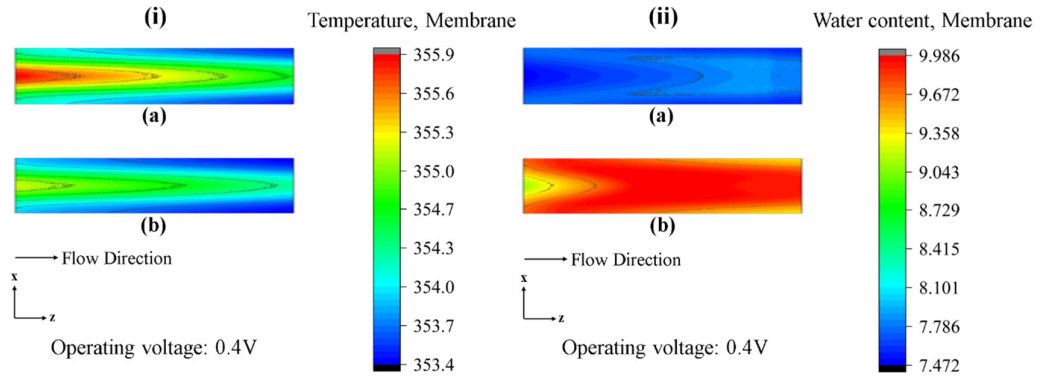


Figure 6.11 (i) Temperature and (ii) water content variation in the membrane at 0.4V for (a) case 1, and (b) case 2.

The water content and the current density (Acm^{-2}) variation at the cathode CL-membrane, at the voltage of 0.4V are illustrated in Figure 6.12(i) and (ii), respectively. The results convey that in case 2, the water content at the cathode CL-membrane outlet is lowered by 21.4%, suggesting that the ionic conductivity of the membrane is declined, and therefore the cell performance is lowered. Further, the current density at the cathode CL-membrane inlet is lowered by 23.1% compared to case 1. The current density gradually declined along the flow path in both cases possibly due to higher water accumulation in cathode GDL and a decline in the ionic conductivity of the membrane.

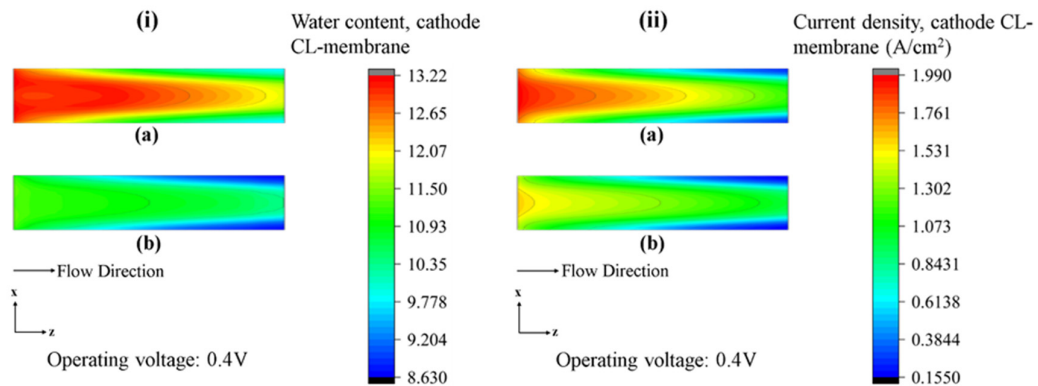


Figure 6.12 (i) Water content and (ii) Current density (Acm^{-2}) variation at the cathode CL-membrane interface at 0.4V for (a) case 1, and (b) case 2.

6.8 Conclusions

The current investigation leads to the following conclusions:

1. The sealants' accelerated creep causes GDL deformation that reduces the thickness and, consequently the GDL porosity and permeability values are altered.
2. The transport characteristics are altered with the change in GDL porosity and permeability; therefore, the PEMFC performance is influenced.
3. It is reported from these results that in case 2, the H₂O concentration at the outlet of anode CL is lowered by 70.45% in comparison with case 1. Furthermore, in case 2, there is an increase in liquid saturation by 70.2% at the cathode GDL, compared to case 1.
4. The findings indicate that in case 2, the water content is lowered by 36% and 13.65% at the anode and cathode CL outlet, respectively, compared to case 1.
5. The results convey that in case 2, the water content at the cathode CL-membrane outlet is lowered by 21.4%, while the current density at the cathode CL-membrane intake is lowered by 23.1%, compared to case 1.
6. The current density reported for case 1 (without creep) and case 2 (sealants' accelerated creep) are 1.309655 and 1.041806 Acm⁻², respectively, at a cell voltage of 0.4V. In addition, the PEMFC performance in case 2 is lowered by 20.45%, compared to 17.78% in case 1, at a cell voltage of 0.4V, indicating the effect of sealants' accelerated creep in the PEMFC working conditions.

6.9 Closure

In the present chapter the influence of PTFE sealants' accelerated creep on the PEMFC performance is explored. In the following chapter, the influence of hygrothermal conditions of PEMFC on the dynamic mechanical properties of various sealants are studied.

CHAPTER 7

IMPACT OF HYGROTHERMAL LOADING ON THE DYNAMIC MECHANICAL CHARACTERISTICS OF SEALANTS

7.1 Introduction

Elastomers are extensively utilized across various industries, such as aerospace, biomedical, and automotive sectors. These elastomers experience various mechanical loads, such as tension, compression, and cyclic loads in these operational conditions (Cui et al. 2012; Radhakrishnan and Haridoss 2010). Nowadays, elastomers are increasingly used as sealants, highlighting their resilience to the environmental conditions of PEMFC (Lin et al. 2011a; Tan et al. 2008b, 2009a). It is evident that the strain rate and environmental conditions during testing significantly affect the dynamic responses of polymeric materials. The assessment of sealants' properties, when subjected to hygrothermal conditions, is critical to ensure the overall performance and longevity of the PEMFC. The functional characteristics of polymeric sealants in PEMFCs are influenced by two key environmental factors; relative humidity (RH) and temperature. Various research works have emphasized the impact of humidity and temperature on the viscoelastic characteristics of polymers.

The current study extensively investigates sealant/gasket materials FKM, EPDM, and PTFE for their dynamic characteristics, which includes storage modulus (E'), and Loss modulus (E''), when subjected to a low axial strain of 0.25%, along with temperature and relative humidity, applicable to PEMFC loading conditions. The motive of this investigation is to demonstrate the cumulative impact of relative humidity (RH) and temperature conditions on the dynamic characteristics of the sealants and, thereby, to determine which material degrades quickly in PEMFC operational conditions. The findings of this study provide invaluable information to assess the impact of PEMFC environmental conditions on the dynamic mechanical characteristics of sealants and, consequently, on the longevity and performance of PEMFCs.

7.2 Methodology

7.2.1. Experimental procedure

Rectangular samples of EPDM, PTFE, and FKM are tested, which have thicknesses of 0.70, 0.53, and 0.43 mm, respectively. These rectangular samples are tested in a Rheometer (DHR 20, TA Instruments), with an RH accessory. In the case of the temperature sweep tests, the samples are subjected to 30 minutes of equilibration at each RH value before beginning the temperature ramp at the rate of 1°C/min. Similarly, in the case of RH sweep tests, the samples are subjected to 15 minutes of equilibration at each temperature level before beginning the RH ramp at a rate of 2% RH/min. The relative humidity sweep tests are performed in the range of 5-90% RH at constant temperatures of room temperature (RT), 45, 60, and 80°C, while the temperature sweep tests are performed in the range of RT to 90°C at the constant relative humidity levels of 0, 50, 70, and 90%. An investigation is conducted to compare the dynamic characteristics of three gasket/sealant materials, namely FKM, EPDM, and PTFE, in PEMFC working conditions.

7.2.2 Dynamic test with RH accessory

Dynamic viscoelastic properties of PTFE, EPDM and FKM samples are explored at various temperatures and RH conditions measured utilizing a Rheometer (DHR 20, TA Instruments) with RH accessory. The operating temperature range for this equipment is 5–120°C. The humidity inside the enclosure is regulated by a mixture of N₂ and water vapor obtained from the RH accessory chamber. The ramp rate for humidity is 2% RH/min, linearly increasing or decreasing with time. The measurable range of relative humidity is from 5 to 95%. The humidity correctness is $\pm 3\%$ for relative humidity (RH) values between 5 and 90% and $\pm 5\%$ for RH values greater than 90%. The tension fixture clamp is chosen for conducting temperature and relative humidity sweep tests with a constant axial strain of 0.25% and loading frequency of 1Hz.

7.2.2.1 RH sweep test

After 15 min of equilibration, RH sweep tests are conducted isothermally at four constant temperatures (30, 45, 60 and 80°C) at a humidity ramp rate of 2% RH/min.

The humidity range is taken from 5 to 90% RH, which is the operating range for the Rheometer (DHR 20, TA Instruments).

7.2.2.2. Temperature sweep test

After 30 min of equilibration, temperature sweep tests are conducted at 1°C/min considering four constant RH of 0, 50, 70 and 90% RH. The temperature sweep test is conducted from room temperature (RT) up to 90°C on Rheometer (DHR 20, TA Instruments).

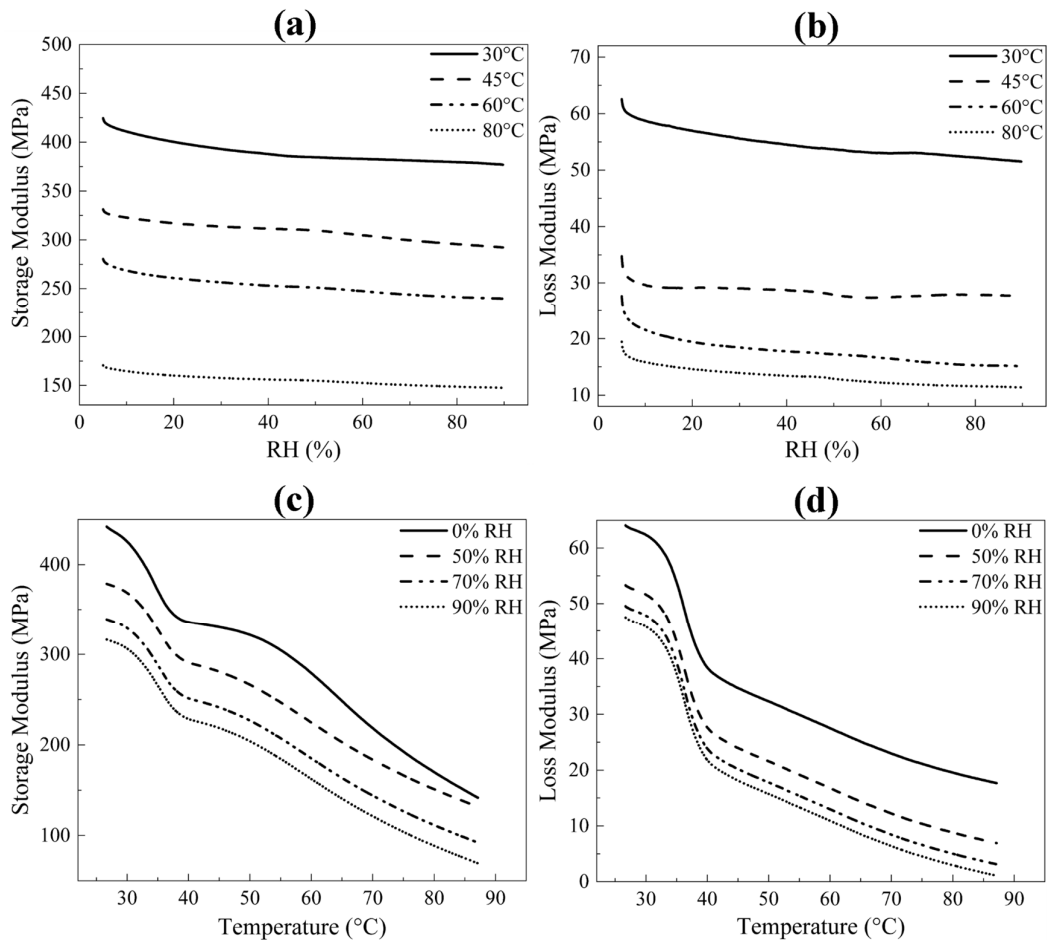


Figure 7.1 (a) E' and (b) E'' for RH sweep test and (c) E' and (d) E'' for temperature sweep test for PTFE samples.

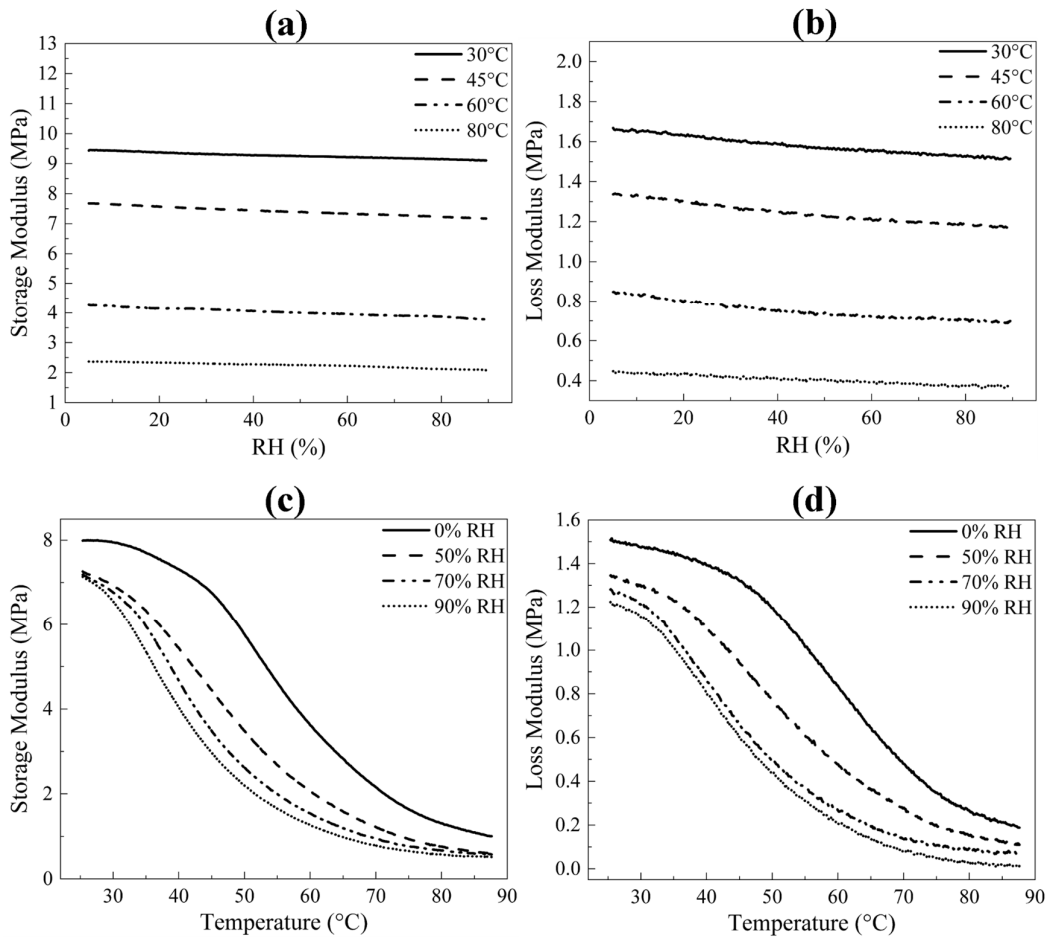


Figure 7.2 (a) E' and (b) E'' for RH sweep test and (c) E' and (d) E'' for temperature sweep test for EPDM samples.

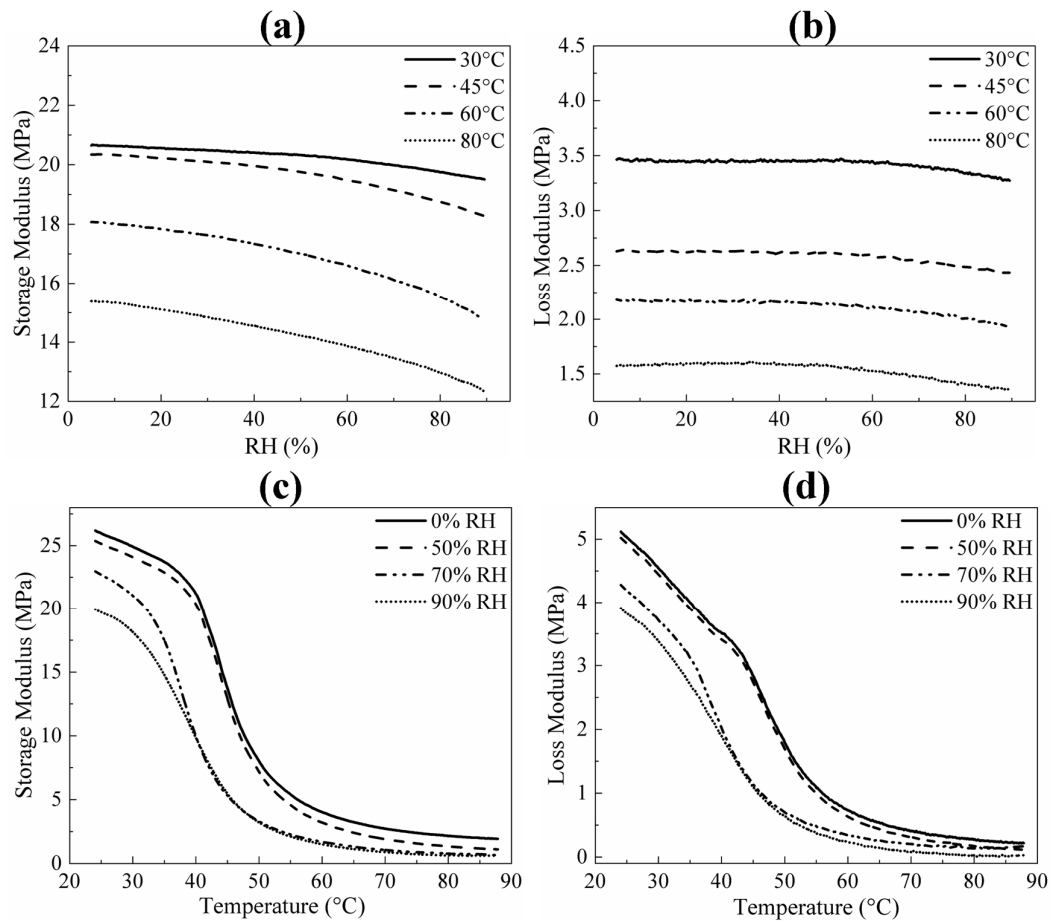


Figure 7.3 (a) E' and (b) E'' for RH sweep test and (c) E' and (d) E'' for temperature sweep test for FKM (VITON) samples.

7.3 Results and Discussion

7.3.1 Combined effect of RH and temperature on dynamic viscoelastic properties of sealants

The impact of RH and temperature on E' , and E'' of PTFE, EPDM and VITON samples are evaluated using the RH and temperature sweep tests. Figure 7.1 (a-b) and Figure 7.1 (c-d) shows the dynamic characteristics of PTFE samples during the RH and temperature sweep tests, respectively. Figure 7.2 (a-b) and Figure 7.2 (c-d) demonstrates the dynamic characteristics of EPDM samples during the RH and temperature sweep tests, respectively. Similarly, Figure 7.3 (a-b) and Figure 7.3 (c-d)

demonstrates the dynamic characteristics of FKM (VITON) samples during the RH and temperature sweep tests, respectively.

It is evident from the findings in Figure 7.1(a-b), 7.2(a-b), and 7.3(a-b) that E' declined by 65.2%, 77.98%, and 40%, whereas E'' declined by 81.83%, 77.69% and 60.92% for PTFE, EPDM and VITON, respectively, when the temperature is raised from 30 to 80°C, during the RH sweep test. Moreover, it is observed from the findings in Figure 7.1(c-d), 7.2(c-d), and 7.3(c-d) that E' is lowered by 84.24%, 93.4%, and 97.61%, whereas E'' is lowered by 98.12%, 94.95%, and 99.47% for PTFE, EPDM, and VITON, respectively, when RH is increased from 0 to 90%, for the temperature sweep test. These findings suggest that the dynamic mechanical characteristics of PTFE, EPDM and VITON sealants deteriorate in the PEMFC operational conditions.

A detailed analysis of the results in Figure 7.1(c-d) reveals that there is a slope change in the E' and E'' curves at nearly 40°C, which is reflected as a maxima peak at 37.5°C in the $\text{Tan } \delta$ plot for PTFE as demonstrated in the results in the refs (Blumm et al. 2010; Wingard 2018). Moreover, the findings from Figure 7.2(c-d) demonstrate that there is a slope change in the E' and E'' curves at nearly 55°C, which is reflected as a maxima peak at 60°C in the $\text{Tan } \delta$ plot for EPDM samples as demonstrated in the results in the ref (Davenas et al. 2003). Finally, the findings indicate that E' and E'' decline gradually with temperature, whereas these properties decline sharply with an increase in RH for all three sealant materials and are in fair agreement with the results in ref (Lin et al. 2011d).

7.4 Conclusion

The present study on the dynamic viscoelastic characteristics of sealants in PEMFC leads to the following conclusions,

1. The findings indicate that E' declined by 65.2%, 77.98%, and 40%, whereas E'' declined by 81.83%, 77.69%, and 60.92% for PTFE, EPDM, and VITON, respectively, when the temperature is raised from 30 to 80°C during the RH sweep test.

2. It is observed from the findings that E' is lowered by 84.24%, 93.4%, and 97.61%, whereas E'' is lowered by 98.12%, 94.95%, and 99.47% for PTFE, EPDM, and VITON, respectively, when RH is increased from 0 to 90%, for the temperature sweep test.
3. The findings disclosed that a slope change occurred at nearly 40°C in the E' and E'' curves for PTFE samples and at nearly 55°C a slope change occurred in the E' and E'' curves for EPDM samples.
4. The findings reveal that E' , and E'' for PTFE, EPDM, and VITON samples decline gradually with temperature, whereas these properties decline sharply with an increase in RH, indicating the dominance of RH over temperature on the dynamic properties.
5. The findings from the RH and temperature sweep tests indicate that the degradation is least for VITON sealant and highest for EPDM sealant in the case of the RH sweep test. Furthermore, the findings indicate that the degradation is least for PTFE sealant and highest for VITON sealant in the case of the temperature sweep test.

7.5 Limitations of the study

The limitations of the study are:

- The present study has some limitations on the applicability of the analytical model to the experimental results of PTFE sealants at higher temperatures (above 45°C), particularly at the stress of 4 MPa.
- The creep characteristics of other commercial sealants (silicone, EPDM, and FKM rubber) are not considered in the present study.

7.6 Closure

The present chapter addresses the combined influence of RH and temperature conditions of PEMFC on the dynamic viscoelastic characteristics of various sealant materials (EPDM, FKM, and PTFE). The following chapter discusses the conclusions drawn from this thesis and the scope for future work.

CHAPTER 8

CONCLUSIONS AND FUTURE WORK

8.1 Conclusion

The PEM fuel cell's performance is key to improving its longevity. Sealants are the vital components whose physical and chemical characteristics highly influence the PEMFC performance and longevity.

The present thesis begins with studying the physical and chemical characteristics of commercial sealant materials such as Silicone rubber, EPDM rubber, FKM rubber, and PTFE under the PEMFC operating conditions. The physical and chemical characteristics of the sealants discussed suggest that the overall performance and longevity of PEMFCs are improved. Therefore, the sealants' material selection and design are crucial for improving the overall performance of LT-PEMFC and HT-PEMFC. In the process of reviewing the physical and chemical properties of the sealants along with their designs in PEMFCs, it is identified that the development of standard testing techniques for sealants is essential for further improving the longevity of the LT-PEMFC and HT-PEMFC.

Consequently, an extensive experimental investigation is conducted to examine the creep characteristics of PTFE sealant at different temperatures including 25 (RT), 35, 45, 55, and 65°C, at stresses of 2, 3, and 4 MPa. The creep behaviour within the range of 2–4 MPa displays sufficient comparability, since the creep strains demonstrate nearly identical increases with temperature. This is illustrated from the creep strain curves at stresses of 2, 3, and 4 MPa, where the slope of these curves (strain rate) increases with temperature. Moreover, their slopes are again increasing with an increase in stress level.

Furthermore, an analytical study is conducted on PTFE sealant by developing the master curves at a specified temperature of 25°C, at three stress levels of 2, 3, and 4 MPa utilizing the TTS method and WLF equation. The creep compliance master curve for PTFE samples offers a prediction for 4.5 hours. Except for the creep plots predicted at 4 MPa at higher temperatures, the forecasts provided by the model are fairly

consistent with the experimental data for the stress levels of 2 and 3 MPa at almost all temperatures. The deviations in the curves are potentially caused due to the occurrence of viscoplastic strains in PTFE samples at higher temperatures, especially at higher stresses.

Next, a two-dimensional structural model of PEMFC is considered for investigating the accelerated creep in PTFE sealant due to the assembly loading conditions. The sealants' accelerated creep analysis is conducted by considering the Prony series parameters for PTFE sealant. The sealants' accelerated creep causes GDL deformation, reduces thickness, and alters GDL porosity and permeability values. It is reported from the sealants' accelerated creep analysis that the anode GDL porosity dropped from the initial value of 0.6 to 0.5023, whereas it dropped from 0.6 to 0.5788 at the cathode GDL.

Further, a numerical investigation is conducted by considering a three-dimensional, steady state, incompressible, and non-isothermal model of a single straight flow channel with an active area of 1cm^2 . The reported current densities for case 1 (without creep) and case 2 (sealants' accelerated creep) are 0.591987 Acm^{-2} and 0.486737 Acm^{-2} , respectively, at a voltage of 0.6V. Similarly, the average current density for case 1 is 1.309655 Acm^{-2} , while for case 2, it is 1.041806 Acm^{-2} , at a cell voltage of 0.4V. Additionally, the PEMFC performance in case 2 is lowered by 20.45%, compared to 17.78% in case 1, at a cell voltage of 0.4V, indicating the effect of sealants' accelerated creep in the PEMFC working conditions.

Finally, an experimental investigation is conducted to examine the collective impact RH and temperature on the dynamic viscoelastic characteristics of EPDM rubber, FKM (VITON) rubber, and PTFE sealants in PEMFCs. The samples are exposed to four RH conditions of 0, 50, 70, and 90% during the temperature sweep from room temperature (RT) up to 90°C. Further, during the RH sweep tests in the range of 5-90% RH, the samples are subjected to four temperatures 30, 45, 60, and 80°C. The findings from the RH and temperature sweep tests indicate that the degradation is least for VITON sealant and highest for EPDM sealant in the case of the RH sweep test. Furthermore, the degradation is least for PTFE sealant and highest for VITON sealant in the case of the temperature sweep test.

8.2 Scope for future work

The future scope of the present work to further extend this work shall include:

- Experimentally and numerically investigating the creep characteristics of other commercial sealant materials (e.g. EPDM, FKM, and their variants) in PEMFC working conditions.
- Carrying out the numerical investigation on the impact of PTFE sealants' accelerated creep on cell performance by incorporating a multichannel 3D PEMFC model.
- Experimental investigation of the creep characteristics of commercial sealants in PEMFC under the assembly loading conditions at the cell-level.
- Experimentally and numerically investigating the creep characteristics of commercial sealant materials under compressive or combined loading conditions.

REFERENCES

- Alawsi, G., Aldajah, S., and Rahmaan, S. A. (2009). "Impact of humidity on the durability of E-glass/polymer composites." *Mater. Des.*, 30(7), 2506–2512.
- Albert P. Grasso, Vernon; Myron Krasij, Avon; Michael J. Rajpolt, M. (2000). "Use of Thermoplastic Films to Create Seals and Bond PEM Cell Components." United States Patent.
- Allen, D. H., Holmberg, J. A., Ericson, M., Lans, L., Svensson, N., and Holmberg, S. (2001). "Modeling the viscoelastic response of GMT structural components." *Compos. Sci. Technol.*, 61(4), 503–515.
- Améduri, B., Boutevin, B., and Kostov, G. (2001). "Fluoroelastomers: Synthesis, properties and applications." *Prog. Polym. Sci.*, 26(1), 105–187.
- Araya, S. S., Zhou, F., Liso, V., Sahlin, S. L., Vang, J. R., Thomas, S., Gao, X., Jeppesen, C., and Kær, S. K. (2016). "A comprehensive review of PBI-based high temperature PEM fuel cells." *Int. J. Hydrogen Energy*, 41(46), 21310–21344.
- Arif, M., Cheung, S. C. P., and Andrews, J. (2020). "A systematic approach for matching simulated and experimental polarization curves for a PEM fuel cell." *Int. J. Hydrogen Energy*, 45(3), 2206–2223.
- Arthurs, C., and Kusoglu, A. (2021). "Compressive Creep of Polymer Electrolyte Membranes: A Case Study for Electrolyzers." *ACS Appl. Energy Mater.*, 4(4), 3249–3254.
- Baik, K. D., Kong, I. M., Hong, B. K., Kim, S. H., and Kim, M. S. (2013). "Local measurements of hydrogen crossover rate in polymer electrolyte membrane fuel cells." *Appl. Energy*, 101, 560–566.
- Basuli, U., Jose, J., Lee, R. H., Yoo, Y. H., Jeong, K. U., Ahn, J. H., and Nah, C. (2012). "Properties and degradation of the gasket component of a proton exchange membrane fuel cell—A review." *J. Nanosci. Nanotechnol.*, 12(10), 7641–7657.
- Betten, J., and Tsang, N. (2003). *Creep Mechanics. Appl. Mech. Rev.*

Bharadwaj, M., Claramunt, S., and Srinivasan, S. (2017). “Modeling Creep Relaxation of Polytetrafluorethylene Gaskets for Finite Element Analysis.” *Int. J. Mater. Mech. Manuf.*, 5(2), 123–126.

Bhosale, A. C., Mahajan, M. A., and Ghosh, P. C. (2019). “Optimization of contact resistance with better gasketing for a unitized regenerative fuel cell.” *Int. J. Hydrogen Energy*, 44(37), 20953–20962.

Blumm, J., Lindemann, A., Meyer, M., and Strasser, C. (2010). “Characterization of PTFE using advanced thermal analysis techniques.” *Int. J. Thermophys.*, 31(10), 1919–1927.

Bouziane, K., Khetabi, E. M., Lachat, R., Zamel, N., Meyer, Y., and Candusso, D. (2020). “Impact of cyclic mechanical compression on the electrical contact resistance between the gas diffusion layer and the bipolar plate of a polymer electrolyte membrane fuel cell.” *Renew. Energy*, 153, 349–361.

Burak Erman, J. E. M. (2011). *The Science and Technology of Rubber*. Elsevier Science Ltd.

Carcadea, E., Varlam, M., Ingham, D. B., Ismail, M. S., Patularu, L., Marinoiu, A., and Schitea, D. (2018). “The effects of cathode flow channel size and operating conditions on PEM fuel performance: A CFD modelling study and experimental demonstration.” *Int. J. Energy Res.*, 42(8), 2789–2804.

Ceballos, J. O., Ordoñez, L. C., and Sierra, J. M. (2022). “Numerical simulation of a PEM fuel cell: Effect of tortuosity parameters on the construction of polarization curves.” *Int. J. Hydrogen Energy*, 47(70), 30291–30302.

Chang, H., Wan, Z., Chen, X., Wan, J., Luo, L., Zhang, H., Shu, S., and Tu, Z. (2016). “Temperature and humidity effect on aging of silicone rubbers as sealing materials for proton exchange membrane fuel cell applications.” *Appl. Therm. Eng.*, 104, 472–478.

Charlene Jones, Mike Shorts, M. P. (2007). *1 st Edition. Fluid Seal. Assoc.*, FLUID SEALING ASSOCIATION, EUROPEAN SEALING ASSOCIATION.

Chen, X., Liang, F., Lu, W., Jin, Z., Zhao, Y., and Fu, M. (2018). “High permittivity

nanocomposites embedded with Ag/TiO₂ core-shell nanoparticles modified by phosphonic acid.” *Polymers (Basel)*., 10(6).

Chippar, P., and Ju, H. (2013). “Numerical modeling and investigation of gas crossover effects in high temperature proton exchange membrane (PEM) fuel cells.” *Int. J. Hydrogen Energy*, 38(18), 7704–7714.

Cui, T., Chao, Y. J., and Zee, J. W. Van. (2012). “Stress relaxation behavior of EPDM seals in polymer electrolyte membrane fuel cell environment.” *Int. J. Hydrogen Energy*, 37(18), 13478–13483.

Cui, T., Lin, C. W., Chien, C. H., Chao, Y. J., and Zee, J. W. Van. (2011). “Service life estimation of liquid silicone rubber seals in polymer electrolyte membrane fuel cell environment.” *J. Power Sources*, 196(3), 1216–1221.

Dasappa, P. (2008). “Constitutive Modelling of Creep in a Long Fiber Random Glass Mat Thermoplastic Composite.” University of Waterloo.

Dasappa, P., Lee-Sullivan, P., and Xiao, X. (2009a). “Temperature effects on creep behavior of continuous fiber GMT composites.” *Compos. Part A Appl. Sci. Manuf.*, 40(8), 1071–1081.

Dasappa, P., Lee-Sullivan, P., Xiao, X., and Foss H, P. (2009b). “Tensile Creep of a Long-Fiber Glass Mat Thermoplastic Composite. I. Short-Term Tests Prasad.” *Polym. Compos.*

Dasappa, P., Lee-Sullivan, P., Xiao, X., and Foss H, P. (2009c). “Tensile Creep of a Long-Fibre Glass Mat Thermoplastic (GMT) Composite. II. Viscoelastic-Viscoplastic Constitutive Modeling Prasad.” *Polym. Compos.*

Davenas, J., Stevenson, I., Celette, N., Vigier, G., and David, L. (2003). “Influence of the molecular modifications on the properties of EPDM elastomers under irradiation.” *Nucl. Instruments Methods Phys. Res. Sect. B Beam Interact. with Mater. Atoms*, 208(1–4), 461–465.

“Design guide.” (2007). *Fire Prev. Fire Eng. Journals*, (MAR.).

Feng, J., Zhang, Q., Tu, Z., Tu, W., Wan, Z., Pan, M., and Zhang, H. (2014).

“Degradation of silicone rubbers with different hardness in various aqueous solutions.” *Polym. Degrad. Stab.*, 109, 122–128.

Ferry, J. D. (1980). “Viscoelastic properties of polymers.” *Viscoelastic Prop. Polym.*

Gamby, D., and Blugeon, L. (1987). “On the characterization by Schapery’s model of non-linear Viscoelastic materials.” *Polym. Test.*, 7(2), 137–147.

Gillen, K. T., Bernstein, R., Clough, R. L., and Celina, M. (2006a). “Lifetime predictions for semi-crystalline cable insulation materials: I. Mechanical properties and oxygen consumption measurements on EPR materials.” *Polym. Degrad. Stab.*, 91(9), 2146–2156.

Gillen, K. T., Celina, M., Bernstein, R., and Shedd, M. (2006b). “Lifetime predictions of EPR materials using the Wear-out approach.” *Polym. Degrad. Stab.*, 91(12), 3197–3207.

Grelle, T., Wolff, D., and Jaunich, M. (2015). “Temperature-dependent leak tightness of elastomer seals after partial and rapid release of compression.” *Polym. Test.*, 48, 44–49.

Habibnia, M., Shakeri, M., and Nourouzi, S. (2016). “Determination of the effective parameters on the fuel cell efficiency, based on sealing behavior of the system.” *Int. J. Hydrogen Energy*, 41(40), 18147–18156.

Haider, R., Wen, Y., Ma, Z.-F., Wilkinson, D. P., Zhang, L., Yuan, X., Song, S., and Zhang, J. (2021). “High temperature proton exchange membrane fuel cells: progress in advanced materials and key technologies.” *1138 | Chem. Soc. Rev.*, 50, 1138.

Han, W., Du, H., Li, S., Kang, H., and Fang, Q. (2020). “Mechanical properties and creep behavior of fluoroelastomer under hydrochloric acid environments.” *Polym. Bull.*, 77(11), 5967–5983.

Hardiman, M., Vaughan, T. J., and McCarthy, C. T. (2017). “A review of key developments and pertinent issues in nanoindentation testing of fibre reinforced plastic microstructures.” *Compos. Struct.*, 180, 782–798.

Henriques, I. R., Borges, L. A., Costa, M. F., Soares, B. G., and Castello, D. A. (2018).

“Comparisons of complex modulus provided by different DMA.” *Polym. Test.*, 72(August), 394–406.

Herrmann, K., Hasche, K., Pohlenz, F., and Seemann, R. (2001). “Characterisation of the geometry of indenters used for the micro- And nanoindentation method.” *Meas. J. Int. Meas. Confed.*, 29(3), 201–207.

Hiel, C., Cardon, A. H., and Brinson, H. F. (1984). “The Nonlinear Viscoelastic Response.”

Hirano, Y., Inohara, T., Toyoda, M., Murase, H., and Kosakada, M. (2001). “Accelerated weatherability of shed materials for composite insulators.” *IEEE Trans. Dielectr. Electr. Insul.*, 8(1), 97–103.

Hu, H., Zhang, X., He, Y., Guo, Z. S., Zhang, J., and Song, Y. (2013). “Combined effect of relative humidity and temperature on dynamic viscoelastic properties and glass transition of poly(vinyl alcohol).” *J. Appl. Polym. Sci.*, 130(5), 3161–3167.

Huang, Y. X., Cheng, C. H., Wang, X. D., and Jang, J. Y. (2010). “Effects of porosity gradient in gas diffusion layers on performance of proton exchange membrane fuel cells.” *Energy*, 35(12), 4786–4794.

Husar, A., Serra, M., and Kunsch, C. (2007). “Description of gasket failure in a 7 cell PEMFC stack.” *J. Power Sources*, 169(1), 85–91.

Irmscher, P., Qui, D., Janßen, H., Lehnert, W., and Stolten, D. (2019). “Impact of gas diffusion layer mechanics on PEM fuel cell performance.” *Int. J. Hydrogen Energy*, 44(41), 23406–23415.

J.W., W. C. T. T. J. C. Y. J. L. W.-K. S. C. S. Van. (2006). “Fuelcell2006-97124 Degradation of Gasket Materials in a Simulated Fuel Cell.”

Jansen, K. M. B., Zhang, M. F., Ernst, L. J., Vu, D. K., and Weiss, L. (2020). “Effect of temperature and humidity on moisture diffusion in an epoxy moulding compound material.” *Microelectron. Reliab.*, 107(November 2019), 0–5.

Jeya, R. P. K., and . A.-H. B. (2021). “Creep and thermal ratcheting characterization of polytetrafluoroethylene-based gasket materials.” *Adv. Mater. Proc.*, 2(10), 609–614.

- Ji, M., and Wei, Z. (2009). "A review of water management in polymer electrolyte membrane fuel cells." *Energies*, 2(4), 1057–1106.
- Jiao, K., and Li, X. (2011). "Water transport in polymer electrolyte membrane fuel cells." *Prog. Energy Combust. Sci.*, 37(3), 221–291.
- Kashi, S., Varley, R., Souza, M. De, Al-Assafi, S., Pietro, A. Di, Lavigne, C. de, and Fox, B. (2018). "Mechanical, Thermal, and Morphological Behavior of Silicone Rubber during Accelerated Aging." *Polym. - Plast. Technol. Eng.*, 57(16), 1687–1696.
- Konidari, M. V., Papadokostaki, K. G., and Sanopoulou, M. (2011). "Moisture-induced effects on the tensile mechanical properties and glass-transition temperature of poly(vinyl alcohol) films." *J. Appl. Polym. Sci.*, 120(6), 3381–3386.
- Koorata, P. K., and Bhat, S. D. (2020). "Compressive cyclic response of PEM fuel cell gas diffusion media." *Int. J. Hydrogen Energy*, 46(7), 5570–5579.
- Koorata, P. K., and Bhat, S. D. (2021). "Compressive cyclic response of PEM fuel cell gas diffusion media." *Int. J. Hydrogen Energy*, 46(7), 5570–5579.
- Koorata, P. K., and Bhat, S. D. (2022). "Thermomechanical stability and inelastic energy dissipation as durability criteria for fuel cell gas diffusion media with pre-assembly effects." *Int. J. Hydrogen Energy*, 47(2), 1217–1228.
- Kulikovsky, A. A., Divisek, J., and Kornyshev, A. A. (1999). "Modeling the Cathode Compartment of Polymer Electrolyte Fuel Cells: Dead and Active Reaction Zones." *J. Electrochem. Soc.*, 146(11), 3981–3991.
- Kumagai, S., and Yoshimura, N. (1999). "Influence of single and multiple environmental stresses on tracking and erosion of RTV silicone rubber." *IEEE Trans. Dielectr. Electr. Insul.*, 6(2), 211–225.
- Kumar, V., and Koorata, P. K. (2024). "Low stress creep response of PTFE sealants applied to PEM fuel cells." *J. Appl. Polym. Sci.*, 141(17), e55292.
- Kumar, V., Koorata, P. K., Shinde, U., Padavu, P., and George, S. C. (2022a). "Review on physical and chemical properties of low and high-temperature polymer electrolyte membrane fuel cell (PEFC) sealants." *Polym. Degrad. Stab.*, 205.

- Kumar, V., Koorata, P. K., Shinde, U., Padavu, P., and George, S. C. (2022b). "Review on physical and chemical properties of low and high-temperature polymer electrolyte membrane fuel cell (PEFC) sealants." *Polym. Degrad. Stab.*, 205, 110151.
- Kurt, G., and Kasgoz, A. (2021). "Effects of molecular weight and molecular weight distribution on creep properties of polypropylene homopolymer." *J. Appl. Polym. Sci.*, 138(30).
- Lee, B. S., and Lee, D. C. (1999). "Surface degradation properties of ultraviolet treated epoxy/glass fiber." *IEEE Trans. Dielectr. Electr. Insul.*, 6(6), 907–912.
- Lee, S. J., Hsu, C. De, and Huang, C. H. (2005). "Analyses of the fuel cell stack assembly pressure." *J. Power Sources*, 145(2), 353–361.
- Li, G., Tan, J., and Gong, J. (2012). "Chemical aging of the silicone rubber in a simulated and three accelerated proton exchange membrane fuel cell environments." *J. Power Sources*, 217, 175–183.
- Li, H. L., Yin, Z. W., Jiang, D., Jin, L. Y., Cao, Q., and Qu, Y. F. (2018a). "A Study of the Static/Kinetic Friction Behavior of PTFE-Based Fabric Composites." *Tribol. Trans.*, 61(1), 122–132.
- Li, S., and Sundén, B. (2018). "Effects of gas diffusion layer deformation on the transport phenomena and performance of PEM fuel cells with interdigitated flow fields." *Int. J. Hydrogen Energy*, 43(33), 16279–16292.
- Li, S., Yuan, J., Xie, G., and Sunden, B. (2017). "Numerical investigation of transport phenomena in high temperature proton exchange membrane fuel cells with different flow field designs." *Numer. Heat Transf. Part A Appl.*, 72(11), 807–820.
- Li, S., Yuan, J., Xie, G., and Sundén, B. (2018b). "Effects of agglomerate model parameters on transport characterization and performance of PEM fuel cells." *Int. J. Hydrogen Energy*, 43(17), 8451–8463.
- Li, X., and Bhushan, B. (2002). "A review of nanoindentation continuous stiffness measurement technique and its applications." *Mater. Charact.*, 48(1), 11–36.
- Liang, P., Qiu, D., Peng, L., Yi, P., Lai, X., and Ni, J. (2017). "Structure failure of the

sealing in the assembly process for proton exchange membrane fuel cells.” *Int. J. Hydrogen Energy*, 42(15), 10217–10227.

Lin, C. W., Chien, C. H., Tan, J., Chao, Y. J., and Zee, J. W. Van. (2011a). “Dynamic mechanical characteristics of five elastomeric gasket materials aged in a simulated and an accelerated PEM fuel cell environment.” *Int. J. Hydrogen Energy*, 36(11), 6756–6767.

Lin, C. W., Chien, C. H., Tan, J., Chao, Y. J., and Zee, J. W. Van. (2011b). “Chemical degradation of five elastomeric seal materials in a simulated and an accelerated PEM fuel cell environment.” *J. Power Sources*, 196(4), 1955–1966.

Lin, C. W., Chien, C. H., Tan, J., Chao, Y. J., and Zee, J. W. Van. (2011c). “Chemical degradation of five elastomeric seal materials in a simulated and an accelerated PEM fuel cell environment.” *J. Power Sources*, 196(4), 1955–1966.

Lin, C. W., Chien, C. H., Tan, J., Chao, Y. J., and Zee, J. W. Van. (2011d). “Dynamic mechanical characteristics of five elastomeric gasket materials aged in a simulated and an accelerated PEM fuel cell environment.” *Int. J. Hydrogen Energy*, 36(11), 6756–6767.

Liu, Y., Shi, Y., Zhang, D., Li, J., and Huang, G. (2013). “Preparation and thermal degradation behavior of room temperature vulcanized silicone rubber-g-polyhedral oligomeric silsesquioxanes.” *Polymer (Guildf)*, 54(22), 6140–6149.

Lochner, T., Kluge, R. M., Fichtner, J., El-Sayed, H. A., Garlyyev, B., and Bandarenka, A. S. (2020). “Temperature Effects in Polymer Electrolyte Membrane Fuel Cells.” *ChemElectroChem*, 7(17), 3545–3568.

Mahdavi, R., Goodarzi, V., Ali Khonakdar, H., Hassan Jafari, S., Reza Saeb, M., and Shojaei, S. (2018). “Experimental analysis and prediction of viscoelastic creep properties of PP/EVA/LDH nanocomposites using master curves based on time-temperature superposition.” *J. Appl. Polym. Sci.*, 135(38), 1–12.

Majsztrik, P. W., Bocarsly, A. B., and Benziger, J. B. (2008). “Viscoelastic response of nafion. effects of temperature and hydration on tensile creep.” *Macromolecules*, 41(24), 9849–9862.

- Mark, J. E., Eisenberg, A., Graessley, W. W., Mandelkern, L., and Koenig, J. L. (1984). "PHYSICAL PROPERTIES OF POLYMERS." *Phys Prop Polym*.
- Menard, K. P. (1999). *Dynamic Mechanical Analysis, A Practical Introduction*. CRC Press.
- Michael M. Walsh, F. (2000). "Fuel cell assembly fluid flow plate having conductive fibers and rigidizing material therein." *United States Pat*.
- Mikkola, M., Advanced, T. K. K., and Systems, E. (2007). *Studies on Limiting Factors of Polymer Electrolyte Membrane Fuel Cell Cathode. Technology*.
- Mitra, S., Ghanbari-Siahkali, A., Kingshott, P., Almdal, K., Rehmeier, H. K., and Christensen, A. G. (2004a). "Chemical degradation of fluoroelastomer in an alkaline environment." *Polym. Degrad. Stab.*, 83(2), 195–206.
- Mitra, S., Ghanbari-Siahkali, A., Kingshott, P., Hvilsted, S., and Almdal, K. (2004b). "Chemical degradation of an uncrosslinked pure fluororubber in an alkaline environment." *J. Polym. Sci. Part A Polym. Chem.*, 42(24), 6216–6229.
- Mitra, S., Ghanbari-Siahkali, A., Kingshott, P., Hvilsted, S., and Almdal, K. (2006a). "An investigation on changes in chemical properties of pure ethylene-propylene-diene rubber in aqueous acidic environments." *Mater. Chem. Phys.*, 98(2–3), 248–255.
- Mitra, S., Ghanbari-Siahkali, A., Kingshott, P., Rehmeier, H. K., Abildgaard, H., and Almdal, K. (2006b). "Chemical degradation of crosslinked ethylene-propylene-diene rubber in an acidic environment. Part I. Effect on accelerated sulphur crosslinks." *Polym. Degrad. Stab.*, 91(1), 69–80.
- Mitra, S., Ghanbari-Siahkali, A., Kingshott, P., Rehmeier, H. K., Abildgaard, H., and Almdal, K. (2006c). "Chemical degradation of crosslinked ethylene-propylene-diene rubber in an acidic environment. Part II. Effect of peroxide crosslinking in the presence of a coagent." *Polym. Degrad. Stab.*, 91(1), 81–93.
- Mitra, S., Ghanbari-Siahkali, A., Kingshott, P., Rehmeier, H. K., Abildgaard, H., and Almdal, K. (2006d). "Chemical degradation of crosslinked ethylene-propylene-diene rubber in an acidic environment. Part I. Effect on accelerated sulphur crosslinks."

Polym. Degrad. Stab., 91(1), 69–80.

Mitra, S., Ghanbari-Siahkali, A., Kingshott, P., Rehmeier, H. K., Abildgaard, H., and Almdal, K. (2006e). “Chemical degradation of crosslinked ethylene-propylene-diene rubber in an acidic environment. Part I. Effect on accelerated sulphur crosslinks.” *Polym. Degrad. Stab.*, 91(1), 69–80.

Mitra, S., Ghanbari-Siahkali, A., Kingshott, P., Rehmeier, H. K., Abildgaard, H., and Almdal, K. (2006f). “Chemical degradation of crosslinked ethylene-propylene-diene rubber in an acidic environment. Part II. Effect of peroxide crosslinking in the presence of a coagent.” *Polym. Degrad. Stab.*, 91(1), 81–93.

Moreno, V. M., and Gorur, R. S. (1999). “Ac and dc performance of polymeric housing materials for HV outdoor insulators.” *IEEE Trans. Dielectr. Electr. Insul.*, 6(3), 342–350.

Nah, C., Kim, S. G., Shibulal, G. S., Yoo, Y. H., Mensah, B., Jeong, B. H., Hong, B. K., and Ahn, J. H. (2015). “Effects of curing systems on the mechanical and chemical ageing resistance properties of gasket compounds based on ethylene-propylene-diene-termonomer rubber in a simulated fuel cell environment.” *Int. J. Hydrogen Energy*, 40(33), 10627–10635.

Nomula, S. S. R., Rathore, D. K., Ray, B. C., and Prusty, R. K. (2019). “Creep performance of CNT reinforced glass fiber/epoxy composites: Roles of temperature and stress.” *J. Appl. Polym. Sci.*, 136(25), 1–15.

Nunes, L. C. S., Dias, F. W. R., and Costa Mattos, H. S. Da. (2011). “Mechanical behavior of polytetrafluoroethylene in tensile loading under different strain rates.” *Polym. Test.*, 30(7), 791–796.

Ollier-Duréault, V., and Gosse, B. (1998). “Photo-oxidation and electrical aging of anhydride-cured epoxy resins.” *IEEE Trans. Dielectr. Electr. Insul.*, 5(6), 935–943.

Ollier, R. P., Casado, U., Torres Nicolini, A., Alvarez, V. A., Pérez, C. J., and Ludueña, L. N. (2021). “Improved creep performance of melt-extruded polycaprolactone/organo-bentonite nanocomposites.” *J. Appl. Polym. Sci.*, 138(38), 1–11.

Padavu, P., Koorata, P. K., and Bhat, S. D. (2021a). “Numerical investigation on the improved reactant mass transport with depth-dependent flow fields in polymer electrolyte fuel cell under inhomogeneous gas diffusion layer compression.” *Int. J. Heat Mass Transf.*, 180.

Padavu, P., Koorata, P. K., and Bhat, S. D. (2021b). “Numerical investigation on the improved reactant mass transport with depth-dependent flow fields in polymer electrolyte fuel cell under inhomogeneous gas diffusion layer compression.” *Int. J. Heat Mass Transf.*, 180, 121796.

Padavu, P., Koorata, P. K., and Kattimani, S. (2023). “Model based evaluation of water management and membrane hydration in polymer electrolyte fuel cell with reactant flow-field gradients.” *Int. J. Heat Mass Transf.*, 214, 124460.

Park, J. S., Park, J. W., and Ruckenstein, E. (2001). “On the viscoelastic properties of poly(vinyl alcohol) and chemically crosslinked poly(vinyl alcohol).” *J. Appl. Polym. Sci.*, 82(7), 1816–1823.

Parsons, J. (2009). *Low Cost, Durable Seals For PEM Fuel Cells*.

Pehlivan-Davis, S. (2015). “Polymer Electrolyte Membrane (PEM) Fuel Cell Seals Durability.”

Peretz, D., and Weitsman, Y. (1983). “The Nonlinear Thermoviscoelastic Characterizations of FM-73 Adhesives.” *J. Rheol. (N. Y. N. Y.)*, 27(2), 97–114.

Performance, D. (2009). “Perfluoroelastomer and Fluoroelastomer Seals for Photovoltaic Cell Manufacturing Processes.” (May).

Poornesh, K. K., and Cho, C. (2011a). “Poroelastic PEM fuel cell catalyst layer and its implication in predicting the effect of mechanical load on flow and transport properties.” *Int. J. Hydrogen Energy*, 36(5), 3623–3634.

Poornesh, K. K., and Cho, C. (2011b). “Poroelastic PEM fuel cell catalyst layer and its implication in predicting the effect of mechanical load on flow and transport properties.” *Int. J. Hydrogen Energy*, 36(5), 3623–3634.

Poornesh, K. K., and Cho, C. (2015). “Stability of Polymer Electrolyte Membranes In

Fuel Cells: Initial Attempts To Bridge Physical And Chemical Degradation Modes.” *Fuel Cells*, 15(1), 196–203.

Poornesh, K. K., Lee, S. K., Cho, C., and Choi, K. W. (2010). “Effect of bipolar plate materials on the stress distribution and interfacial contact resistance in PEM fuel cell.” *Int. J. Precis. Eng. Manuf.*, 11(4), 583–588.

Poornesh, K. K., Sohn, Y. J., Park, G. G., and Yang, T. H. (2012). “Gas-diffusion layer’s structural anisotropy induced localized instability of nafion membrane in polymer electrolyte fuel cell.” *Int. J. Hydrogen Energy*, 37(20), 15339–15349.

Poornesh, K. K., Wendling, L., Xiao, Y., and Cho, C. (2014). “Effect of hygrothermal ageing on the tensile and fracture response of a fuel cell membrane.” *Smart Mater. Struct.*, 23(7), 075017.

Poornesh, K. K., Xiao, Y., and Cho, C. (2013). “Thermo-Mechanical Response of Fuel Cell Electrodes: Constitutive Model and Application in Studying the Structural Response of Polymer Electrolyte Fuel Cell.” *Fuel Cells*, 13(2), 217–226.

Porte, E., Eristoff, S., Agrawala, A., and Kramer-Bottiglio, R. (2023). “Characterization of Temperature and Humidity Dependence in Soft Elastomer Behavior.” *Soft Robot.*, 00(00), 1–13.

Pozio, A., Giorgi, L., Francesco, M. De, Silva, R. F., Presti, R. Lo, and Danzi, A. (2002). “Membrane electrode gasket assembly (MEGA) technology for polymer electrolyte fuel cells.” *J. Power Sources*, 112(2), 491–496.

Qiu, D., Liang, P., Peng, L., Yi, P., Lai, X., and Ni, J. (2020). “Material behavior of rubber sealing for proton exchange membrane fuel cells.” *Int. J. Hydrogen Energy*, 45(8), 5465–5473.

Radhakrishnan, V., and Haridoss, P. (2010). “Effect of cyclic compression on structure and properties of a Gas Diffusion Layer used in PEM fuel cells.” *Int. J. Hydrogen Energy*, 35(20), 11107–11118.

Restrepo-Zapata, N. C., Ortiz, J. P. H., and Osswald, T. A. (2013). “Methodology for generation of time-temperature-transformation (TTT) diagram: Solid and cellular

epdm.” *Annu. Tech. Conf. - ANTEC, Conf. Proc.*, 1(January 2016), 743–748.

Rosli, R. E., Sulong, A. B., Daud, W. R. W., Zulkifley, M. A., Husaini, T., Rosli, M. I., Majlan, E. H., and Haque, M. A. (2017). “A review of high-temperature proton exchange membrane fuel cell (HT-PEMFC) system.” *Int. J. Hydrogen Energy*, 42(14), 9293–9314.

Scholz, H. (2015). “Modeling and investigation of flooding phenomena in low-temperature PEM fuel cells.” *AutoUni-Schriftenreihe, Logos-Verl.*, Berlin.

Schulze, M., Knöri, T., Schneider, A., and Gülzow, E. (2004). “Degradation of sealings for PEFC test cells during fuel cell operation.” *J. Power Sources*, 127(1–2), 222–229.

Shaw, M. T., and MacKnight, W. J. (2005). *Introduction to Polymer Viscoelasticity*. Wiley.

Shen, L., Xia, L., Han, T., Wu, H., and Guo, S. (2016a). “Improvement of hardness and compression set properties of EPDM seals with alternating multilayered structure for PEM fuel cells.” *Int. J. Hydrogen Energy*, 41(48), 23164–23172.

Shen, L., Xia, L., Han, T., Wu, H., and Guo, S. (2016b). “Improvement of hardness and compression set properties of EPDM seals with alternating multilayered structure for PEM fuel cells.” *Int. J. Hydrogen Energy*, 41(48), 23164–23172.

Shi, S., Chen, G., Wang, Z., and Chen, X. (2013). “Mechanical properties of Nafion 212 proton exchange membrane subjected to hygrothermal aging.” *J. Power Sources*, 238, 318–323.

Shinde, U., and Koorata, P. K. (2021a). “Numerical investigation on the sensitivity of endplate design and gas diffusion material models in quantifying localized interface and bulk electrical resistance.” *Int. J. Hydrogen Energy*, 46(33), 17358–17373.

Shinde, U., and Koorata, P. K. (2021b). “Numerical investigation on the sensitivity of endplate design and gas diffusion material models in quantifying localized interface and bulk electrical resistance.” *Int. J. Hydrogen Energy*, 46(33), 17358–17373.

Shinde, U., and Koorata, P. K. (2022). “A phase-dependent constitutive model to predict cyclic electrical conductivity in fuel cell gas diffusion media.” *J. Power*

Sources, 527, 231179.

Shinde, U., Koorata, P. K., and Padavu, P. (2023). “Electrical/flow heterogeneity of gas diffusion layer and inlet humidity induced performance variation in polymer electrolyte fuel cells.” *Int. J. Hydrogen Energy*, 48(34), 12877–12892.

Shojaei, L., Goodarzi, V., Otadi, M., Khonakdar, H. A., Jafari, S. H., Asghari, G. hossein, and Reuter, U. (2018). “Temperature and frequency-dependent creep and recovery studies on PVDF-HFP/organo-modified layered double hydroxides nanocomposites.” *J. Appl. Polym. Sci.*, 135(23), 1–15.

Stan, F., and Fetecau, C. (2013). “Study of stress relaxation in polytetrafluoroethylene composites by cylindrical macroindentation.” *Compos. Part B Eng.*, 47, 298–307.

Stanley P. Bonk, Myron Krasij, C. A. R. (2002). “Fuel cell stack assembly with edge seal.” *United States Pat.*

Streitwieser, A., and Heathcock, C. H. (1976). *Introduction to organic chemistry*. New York: Macmillan.

Swaminathan, G., and Shivakumar, K. (2009). “A Re-examination of DMA testing of polymer matrix composites.” *J. Reinf. Plast. Compos.*, 28(8), 979–994.

Tábi, T., Wacha, A. F., and Hajba, S. (2019). “Effect of D-lactide content of annealed poly(lactic acid) on its thermal, mechanical, heat deflection temperature, and creep properties.” *J. Appl. Polym. Sci.*, 136(8), 1–10.

Tan, J., Chao, Y. J., Li, X., and Zee, J. W. Van. (2007a). “Degradation of silicone rubber under compression in a simulated PEM fuel cell environment.” *J. Power Sources*, 172(2), 782–789.

Tan, J., Chao, Y. J., Li, X., and Zee, J. W. Van. (2009a). “Microindentation Test for Assessing the Mechanical Properties of Silicone Rubber Exposed to a Simulated Polymer Electrolyte Membrane Fuel Cell Environment.” *J. Fuel Cell Sci. Technol.*, 6(4), 1–9.

Tan, J., Chao, Y. J., Wang, H., Gong, J., and Zee, J. W. Van. (2009b). “Chemical and mechanical stability of EPDM in a PEM fuel cell environment.” *Polym. Degrad. Stab.*,

94(11), 2072–2078.

Tan, J., Chao, Y. J., Wang, H., Gong, J., and Zee, J. W. Van. (2009c). “Chemical and mechanical stability of EPDM in a PEM fuel cell environment.” *Polym. Degrad. Stab.*, 94(11), 2072–2078.

Tan, J., Chao, Y. J., Yang, M., Lee, W. K., and Zee, J. W. Van. (2011). “Chemical and mechanical stability of a Silicone gasket material exposed to PEM fuel cell environment.” *Int. J. Hydrogen Energy*, Pergamon, 1846–1852.

Tan, J., Chao, Y. J., Yang, M., Williams, C. T., and Zee, J. W. Van. (2008a). “Degradation Characteristics of Elastomeric Gasket Materials in a Simulated PEM Fuel Cell Environment.” *J. Mater. Eng. Perform.*, 17(6), 785–792.

Tan, J., Chao, Y. J., Yang, M., Williams, C. T., and Zee, J. W. Van. (2008b). “Degradation characteristics of elastomeric gasket materials in a simulated PEM fuel cell environment.” *J. Mater. Eng. Perform.*, 17(6), 785–792.

Tan, J., Chao, Y. J., Yang, M., Williams, C. T., and Zee, J. W. Van. (2008c). “Degradation characteristics of elastomeric gasket materials in a simulated PEM fuel cell environment.” *J. Mater. Eng. Perform.*, 17(6), 785–792.

Tan, J., Chao, Y. J., Yang, M., Williams, C. T., and Zee, J. W. Van. (2008d). “Degradation characteristics of elastomeric gasket materials in a simulated PEM fuel cell environment.” *J. Mater. Eng. Perform.*, 17(6), 785–792.

Tan, J., Chao, Y. J., Zee, J. W. Van, and Lee, W. K. (2007b). “Degradation of elastomeric gasket materials in PEM fuel cells.” *Mater. Sci. Eng. A*, 669–675.

Tan, J., Chao, Y. J., Zee, J. W. Van, and Lee, W. K. (2007c). “Degradation of elastomeric gasket materials in PEM fuel cells.” *Mater. Sci. Eng. A*, 445–446, 669–675.

Tan, J., Chao, Y. J., Zee, J. W. Van, Li, X., Wang, X., and Yang, M. (2008e). “Assessment of mechanical properties of fluoroelastomer and EPDM in a simulated PEM fuel cell environment by microindentation test.” *Mater. Sci. Eng. A*, 496(1–2), 464–470.

Tan, J., Chao, Y. J., Zee, J. W. Van, Li, X., Wang, X., and Yang, M. (2008f).

“Assessment of mechanical properties of fluoroelastomer and EPDM in a simulated PEM fuel cell environment by microindentation test.” *Mater. Sci. Eng. A*, 496(1–2), 464–470.

Tawalbeh, M., Alarab, S., Al-Othman, A., and Javed, R. M. N. (2022). “The Operating Parameters, Structural Composition, and Fuel Sustainability Aspects of PEM Fuel Cells: A Mini Review.” *Fuels*, 3(3), 449–474.

Tomer, N. S., Delor-Jestin, F., Singh, R. P., and Lacoste, J. (2007). “Cross-linking assessment after accelerated ageing of ethylene propylene diene monomer rubber.” *Polym. Degrad. Stab.*, 92(3), 457–463.

Um, S., Wang, C.-Y., and Chen, K. S. (2000). “Computational Fluid Dynamics Modeling of Proton Exchange Membrane Fuel Cells.” *J. Electrochem. Soc.*, 147(12), 4485.

Um, S., and Wang, C. Y. (2004). “Three-dimensional analysis of transport and electrochemical reactions in polymer electrolyte fuel cells.” *J. Power Sources*, 125(1), 40–51.

Wang, Q., Zheng, F., and Wang, T. (2016). “Tribological properties of polymers PI, PTFE and PEEK at cryogenic temperature in vacuum.” *Cryogenics (Guildf.)*, 75, 19–25.

Wang, Y., and Chen, K. S. (2011). “Effect of Spatially-Varying GDL Properties and Land Compression on Water Distribution in PEM Fuel Cells.” *J. Electrochem. Soc.*, 158(11), B1292.

Wang, Y., and Wang, C. Y. (2005). “Transient analysis of polymer electrolyte fuel cells.” *Electrochim. Acta*, 50(6), 1307–1315.

Weber, A. Z., and Newman, J. (2004). “Transport in Polymer-Electrolyte Membranes.” *J. Electrochem. Soc.*, 151(2), A311.

Wingard, D. (2018). *Use of DSC and DMA Techniques to Help Investigate a Material Anomaly for PTFE Used in Processing a Piston Cup for the Urine Processor Assembly (UPA) on International Space Station (ISS)*.

- Wu, F., Chen, B., Yan, Y., Chen, Y., and Pan, M. (2018a). “Degradation of silicone rubbers as sealing materials for proton exchange membrane fuel cells under temperature cycling.” *Polymers (Basel)*, 10(5).
- Wu, F., Chen, B., Yan, Y., Chen, Y., and Pan, M. (2018b). “Degradation of Silicone Rubbers as Sealing Materials for Proton Exchange Membrane Fuel Cells under Temperature Cycling.” *Polym. 2018, Vol. 10, Page 522*, 10(5), 522.
- Wu, H., Li, X., and Berg, P. (2009). “On the modeling of water transport in polymer electrolyte membrane fuel cells.” *Electrochim. Acta*, 54(27), 6913–6927.
- Wu, J., Yuan, X. Z., Martin, J. J., Wang, H., Zhang, J., Shen, J., Wu, S., and Merida, W. (2008). “A review of PEM fuel cell durability: Degradation mechanisms and mitigation strategies.” *J. Power Sources*, 184(1), 104–119.
- Xia, L., Wang, M., Wu, H., and Guo, S. (2016). “Effects of cure system and filler on chemical aging behavior of fluoroelastomer in simulated proton exchange membrane fuel cell environment.” *Int. J. Hydrogen Energy*, 41(4), 2887–2895.
- Xia, R., Zhou, H., Zhang, Z., Wu, R., and Wu, W. P. (2018). “Effects of loading conditions on the nanoindentation creep behavior of nafion 117 membranes.” *Polym. Eng. Sci.*, 58(11), 2071–2077.
- Xiao, X. R., Hiel, C. C., and Cardon, A. H. (1994). “Characterization and modeling of nonlinear viscoelastic response of PEEK resin and PEEK composites.” *Compos. Eng.*, 4(7), 681–702.
- Xu, Q., Pang, M., Zhu, L., Zhang, Y., and Feng, S. (2010). “Mechanical properties of silicone rubber composed of diverse vinyl content silicone gums blending.” *Mater. Des.*, 31(9), 4083–4087.
- Yang, P., Wang, Y., Yang, Y., Yuan, L., and Jin, Z. (2021). “Effects of Gas Diffusion Layer Porosity Distribution on Proton Exchange Membrane Fuel Cell.” *Energy Technol.*, 9(7), 1–10.
- Ye, D., and Zhan, Z. (2013). “A review on the sealing structures of membrane electrode assembly of proton exchange membrane fuel cells.” *J. Power Sources*, 231, 285–292.

Ye, J., Yao, T., Deng, Z., Zhang, K., Dai, S., and Liu, X. (2021). “A modified creep model of polylactic acid (PLA-max) materials with different printing angles processed by fused filament fabrication.” *J. Appl. Polym. Sci.*, 138(17), 1–15.

Yin, Y., Wang, J., Yang, X., Du, Q., Fang, J., and Jiao, K. (2014). “Modeling of high temperature proton exchange membrane fuel cells with novel sulfonated polybenzimidazole membranes.” *Int. J. Hydrogen Energy*, 39(25), 13671–13680.

Yoshimura, N., Kumagai, S., and Nishimura, S. (1999). “Electrical and environmental aging of silicone rubber used in outdoor insulation.” *IEEE Trans. Dielectr. Electr. Insul.*, 6(5), 632–650.

Youn, B. H., and Huh, C. S. (2005). “Surface degradation of HTV silicone rubber and EPDM used for outdoor insulators under accelerated ultraviolet weathering condition.” *IEEE Trans. Dielectr. Electr. Insul.*, 1015–1024.

Yuan, X., Li, H., Zhang, S., Martin, J., and Wang, H. (2011). “A review of polymer electrolyte membrane fuel cell durability test protocols.” *J. Power Sources*.

Zhang, H., and Cloud, A. (2006). “The permeability characteristics of silicone rubber.” *Int. SAMPE Tech. Conf.*

Zhang, J., Xie, Z., Zhang, J., Tang, Y., Song, C., Navessin, T., Shi, Z., Song, D., Wang, H., Wilkinson, D. P., Liu, Z. S., and Holdcroft, S. (2006). “High temperature PEM fuel cells.” *J. Power Sources*, 160(2 SPEC. ISS.), 872–891.

Zhang, Z., Tian, C., Yuan, Z., Li, J., Wu, W. P., and Xia, R. (2019). “Temperature and loading sensitivity investigation of nanoindentation short-term creep behavior in Nafion®.” *Mater. Res. Express*, 6(5).

Zhao, J., Guo, H., Xing, Y., Ping, S., Lin, W., Yang, Y., Wang, Z., and Ma, T. (2023). “A review on the sealing structure and materials of fuel-cell stacks.” *Clean Energy*, 7(1), 59–69.

Zhao, T., and Allen Bernstorff, R. (1998). “Ageing tests of polymeric housing materials for non-ceramic insulators.” *IEEE Electr. Insul. Mag.*, 14(2), 26–33.

Zhou, P., and Wu, C. W. (2007). “Numerical study on the compression effect of gas

diffusion layer on PEMFC performance.” *J. Power Sources*, 170(1), 93–100.

Zhou, Y., Jiao, K., Du, Q., Yin, Y., and Li, X. (2013). “Gas diffusion layer deformation and its effect on the transport characteristics and performance of proton exchange membrane fuel cell.” *Int. J. Hydrogen Energy*, 38(29), 12891–12903.

LIST OF PUBLICATIONS

International Journals

1. **Kumar, V.**, Koorata, P. K., Shinde, U., Padavu, P., & George, S. C. (2022). Review on physical and chemical properties of low and high-temperature polymer electrolyte membrane fuel cell (PEFC) sealants. *Polymer Degradation and Stability*, 205, (2022), 110151 (IF: 6.3)
2. **Kumar, V.**, Koorata, P. K.. (2024). Low stress creep response of PTFE sealants applied to PEM fuel cells, *J. Appl. Polym. Sci.*, 141(17), e55292 (2024) (IF: 3.0)
3. **Kumar, V.**, Koorata, P. K., Evaluating the PEM fuel cell performance under accelerated creep of sealants (Submitted to *International Journal of Hydrogen Energy*).
4. **Kumar, V.**, Koorata, P. K., Experimental study on dynamic characteristics of Ethylene propylene diene monomer (EPDM), Fluoroelastomer (FKM) and Polytetrafluoroethylene (PTFE) sealants subjected to hygrothermal conditions, applicable to PEM fuel cell (Submitted to *Materials Letters*).

BIODATA

Name: Vikas Kumar
Date of Birth: 18/07/1987
Mobile: +91 7541946205
Email: vikaskumarbhgalpur@gmail.com
Address: Sai Janki Enclave, N C C Road, Mundichak, Bhagalpur,
Bihar-812001, India

Qualification:

Degree	University/Institute	Subject	Year	Percentage/Grade
Ph.D	National Institute of Technology Karnataka, Surathkal	PEM Fuel Cells, Manufacturing Engineering	2018 to present	7.5 CGPA (Course work)
M. Tech	National Institute of Technology, Jamshedpur	Industrial Manufacturing Engineering	2014- 2016	8.45 CGPA
B.E.	HCET Jabalpur, Madhya Pradesh	Mechanical Engineering	2007- 2011	65.78%

VIKAS KUMAR